FRAGMENTATION OF MAGNETICALLY-SUPPORTED, WEAKLY-IONIZED MOLECULAR CLOUDS

BY

DUNCAN CHRISTIE

DISSERTATION

Submitted in partial fulfillment of the requirements
for the degree of Doctor of Philosophy in Physics
in the Graduate College of the
University of Illinois at Urbana-Champaign, 2011

Urbana, Illinois

Doctoral Committee:

Professor John Stack, Chair
Professor Telemachos Ch. Mouschovias
Associate Professor Leslie W. Looney
Adjunct Associate Professor Benjamin Wandelt

Abstract

We follow the evolution and fragmentation of isolated, magnetically-supported, weakly-ionized, self-gravitating molecular clouds in three dimensions. Although the model clouds are supported by the magnetic field, high-density, magnetically-supercritical fragments form due to the drift between the ions and the neutrals, *ambipolar diffusion*. To follow the evolution of the model clouds, we extended the publicly-available Zeus-MP code to include the effects of nonideal magnetohydrodynamics and have modified several algorithms to improve accuracy and convergence. We present the results of a parameter study which varies the ionization fraction, mass-to-flux ratio, and velocity perturbation in the model clouds.

Acknowledgements

I would like to thank...

... Telemachos Ch. Mouschovias, for his patience and understanding, his knowledge, and his unwavering support.

... Matthew Kunz, for being both a sounding board and a friend.

... Michael Campbell and the administrators of the Turing Cluster, without whom I would not be able to complete my thesis project.

... Leslie Looney, for providing valuable comments on this manuscript.

... the Department of Physics, for providing financial support in the form of teaching and research assistantships, as well as a travel grant to attend the Cosmic Agitator conference.

... Jacqueline Cook, for being a friend and confidant.

... Dominic Biava, for commiserating during the bad times and celebrating during the good times.

Table of Contents

Chapter 1

Introduction

Stars are the most visible aspect of astrophysics. Almost everyone in the world can look up and see them. They can end their lives in spectacular fashion, and, in the case of SN 1054, be observed with the naked eye. Their formation, however, occurs in the dark depths of molecular clouds, behind an opaque curtain of molecular gas. Under the force of their own self-gravity, these clouds contract and fragment, forming cores, the cold precursors to stars.

The details of how these clouds fragment depends on the chemistry, magnetic field, and turbulent energy of the cloud. In §1.1, the observed properties of molecular clouds are summarized. §1.2 provides an overview of the relevant theoretical aspects of the fragmentation problem with a review of previous numerical studies provided in §1.3. Lastly, the requirements for a model molecular cloud are listed in §1.4.

1.1 Observed Properties of Molecular Clouds

Molecular clouds are large associations of molecular hydrogen, helium, and other trace elements, have sizes ranging from 1 to 5 pc, masses ranging from a few tens to $10^4\ M_\odot$, mean densities on the order of a few $10^3\ \mathrm{cm}^{-3}$, and temperatures ≈ 10 K (Myers 1985). Due to their cold temperatures, they are difficult to distinguish from the background. The most common method of observing molecular clouds is to observe emission from tracer molecules, such as CO, NH_3, HCO^+, N_2H^+, CS, and others. More recently, observations have been made of continuum dust emission at $450\ \mu m$ and $850\ \mu m$, allowing for cores

to be identified based on their protostellar content (e.g. Andre et al. 2000).

1.1.1 Distibution of Matter in Molecular Clouds

Molecular clouds exhibit significant structure. On the parsec scale they appear filamentary, with the filaments fragmenting into high-density cores on smaller scales (e.g. André et al. 2010). Observations of the gas within molecular clouds has shown that the column densities are distributed lognormally with a power-law tail on the high end (Goodman et al. 2009; Kainulainen et al. 2009; Wong et al. 2008; Lombardi et al. 2006). The power-law tail is generally associated with gravitational collapse of the cores and is only seen in clouds with active star formation. The lognormal distribution of column densites has been proposed as a signature of supersonic turbulence within clouds. However, this is not the only explanation (see §5.2.1; also Tassis et al. 2010).

The high-density cores are sites of star formation. The sizes of these vary from 0.05 pc to 1 pc with a mean size ≈ 0.15 pc, although this value can vary greatly from cloud to cloud (Benson and Myers 1989). In general, the spacing between cores is comparable to the Jeans length

$$\lambda_J = \left(\frac{\pi C^2}{G\rho}\right)^{1/2}, \tag{1.1}$$

where C is the sound speed, G is the gravitational constant, and ρ is the average density; however, there are examples where the mean spacing is significantly greater than the Jeans length (e.g. the Pipe nebula).

Determination of the shapes of dense cores is limited by projection effects. Dense cores do not appear circular on the sky, and so statistical methods are required. The earliest attempts at determining the shapes of dense cores yielded contradictory results. Ryden (1996) and Myers et al. (1991) both found a preference for prolate cores with Ryden (1996) claiming that oblate cores are eliminated with 99% confidence. These

analyses were limited in that they did not consider the possibility of cores having triaxial shapes. Analysis by Jones et al. (2001), which allowed for triaxial cores, found that cores are likely triaxial and close to oblate in shape. This result is supported by a Bayesian analysis of the shapes of cores in Orion (Tassis 2007).

There is a wide distribution of core masses, even within a single cloud. The differential mass function takes a piecewise powerlaw form

$$\frac{dN}{dM} \propto M^{-\alpha}\,, \tag{1.2}$$

where, for cores with masses $M > 1.0\ M_{\odot}$, the expontent α ranges from 2 to 2.5, with a typical value of 2.35 (e.g. Motte et al. 1998; Testi and Sargent 1998; Johnstone and Bally 2006; Nutter and Ward-Thompson 2007). For masses $M < 1.0\ M_{\odot}$, the power law is shallower, with $\alpha \approx 1.5$. The exact slopes and the positions of the breaks vary from cloud to cloud. Additionally, there is a turnover in the mass function at small masses; however, it is difficult to observe it since incompleteness in the observation of low-mass cores results in a similar downturn in the observed mass function. In their observations of Orion, Nutter and Ward-Thompson (2007) were able to observe the turnover at $1.3\ M_{\odot}$, four times greater than their incompleteness threshold, indicating that the turnover is likely a real effect.

1.1.2 Magnetic Fields

Although it is exceedingly difficult to determine the strength of the magnetic field, there is strong observational evidence for magnetic fields within molecular clouds, as there is for the general interstellar medium. Most observations of the magnetic field strength in clouds are done by measuring the Zeeman effect, often on a spectral line of OH. In the case where the Zeeman splitting $\Delta\nu_{\mathrm{Zeeman}}$ is much smaller than the width of the specral line $\Delta\nu$ (i.e. $\Delta\nu_{\mathrm{Zeeman}} \ll \Delta\nu$), it is only possible to determine the line-of-sight

component of the magnetic field. In this case, the total magnetic field strength can only be inferred though statistical means.

The cold neutral medium (CNM) in the galaxy has a root-mean-squared (rms) magnetic field of $6.0\ \mu\mathrm{G}$ (Heiles and Troland 2005). Molecular clouds have stronger fields, typically in the range of $10\mu\mathrm{G}$ to $200\mu\mathrm{G}$ (Crutcher 1999; Crutcher and Kazes 1983; Kazes and Crutcher 1986; Goodman et al. 1989). As the density increases beyond $10^4\ \mathrm{cm}^{-3}$ or $10^5\ \mathrm{cm}^{-3}$, the magnetic field begins to scale with the density as

$$B \propto \rho^{\kappa}\ , \tag{1.3}$$

where $\kappa \approx 0.47$, (Crutcher 1999), in excellent agreement with the theoretical prediction by Fiedler and Mouschovias (1993).

By creating polarization maps of molecular clouds, astronomers have been able to map out the morphology of the magnetic field within molecular clouds. In the case of the Pipe nebula (Fig. 1.2), optical polarization measurements indicate that the projected magnetic field is roughly perpendicular to the filamentary structure – the stem of the pipe (Alves et al. 2008). A Bayesian analysis by Tassis et al. (2009) found that molecular clouds are most likely oblate with little triaxiality and that the magnetic field is aligned approximately along the shortest axis. However, because of the small sample size, it was not possible to reject other possibilities.

On the scales of cores, observations show ordered field lines with an hour-glass morphology (e.g. Girart et al. 2006). This morphology is expected when the small-scale structure formation is regulated by the magnetic field instead of supersonic turbulence. This geometry of the magnetic field lines is seen both in nature and in simulations of magnetically supported molecular cloud cores (see Fig. 1.1).

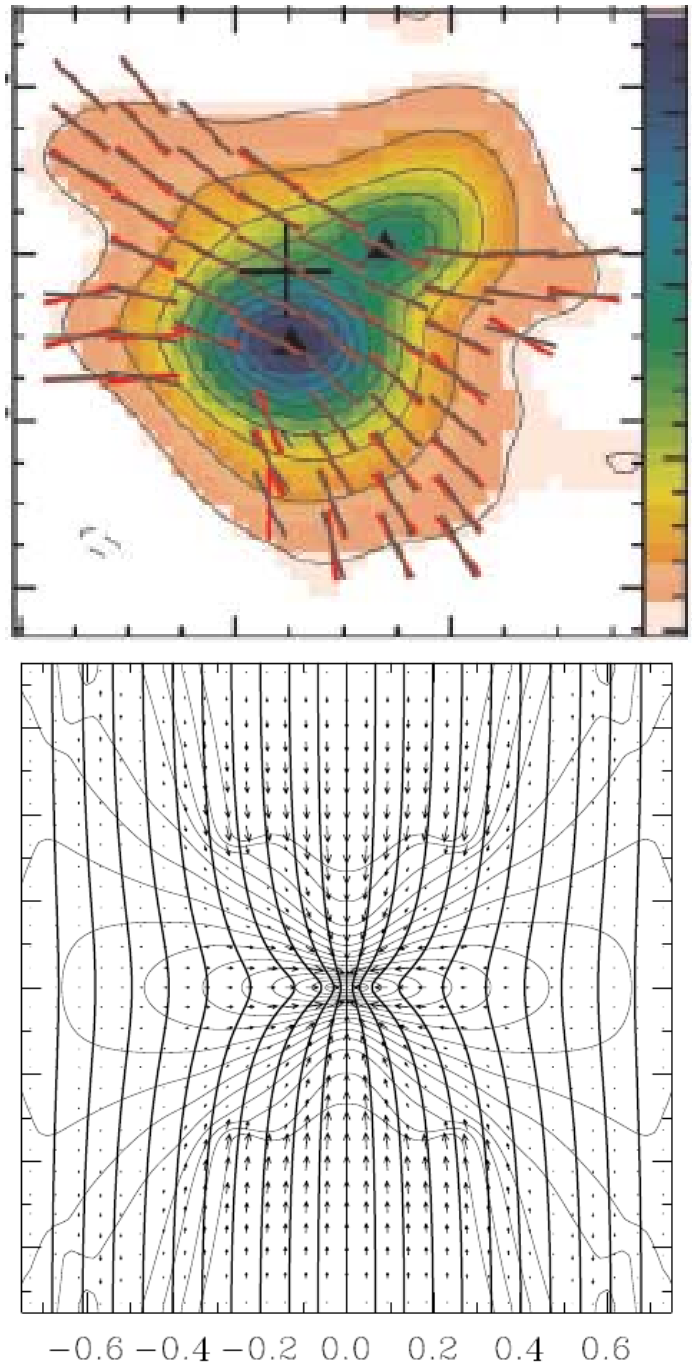

Figure 1.1: *Top:* The protostellar source NGC 1333 IRAS 4A. The red lines correspond to the inferred magnetic field vectors from dust polarimetry, and the contours correspond to the dust emmission (Source: Girart et al. 2006). *Bottom:* The model core from Kunz and Mouschovias (2010). The contours represent the density with the magnetic field lines (solid, dark lines) overlayed. Both observation and theory reveal an hourglass morphology in the magnetic field lines.

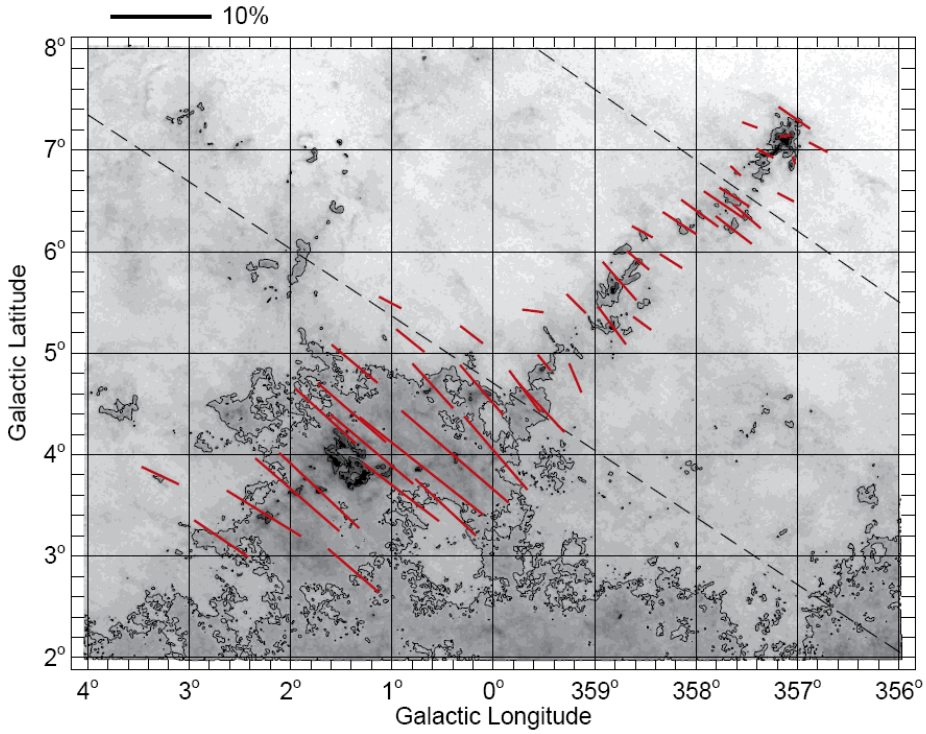

Figure 1.2: Pipe Nebula. The figure shows dust extinction with the magnetic field vectors overplotted. All the magnetic field vectors are roughly parallel and are perpendicular to the filamentary structure (the neck of the pipe). Source: Alves et al. (2008).

1.1.3 Turbulence

The observed supersonic linewidths in molecular clouds have been attributed to turbulent internal motions (Zuckerman and Palmer 1974; Zuckerman and Evans 1974). It has also been shown that the velocity dispersion correlates positively with the size of the object observed (Larson 1981), leading to the suggestion that Kolmogorov-like turbulence is responsible for the observed linewidths. Reanalysis of data by Heyer et al. (2009) found dependence on the surface density Σ_0 of the cloud as well, not found in Larson's scaling relation, implying a more complex explanation for the origin of the linewidths.

Although large nonthermal linewidths are observed within clouds, observations of individual cores indicate that the nonthermal motions within the cores are subsonic (Benson and Myers 1989; Myers and Fuller 1992; Kirk et al. 2007), indicating that these motions are unlikely to contribute to the support of the cores against their self-gravity.

1.2 Theoretical Considerations

1.2.1 Stability and Magnetic Fields

Stability analysis of a gravitating gaseous system (Jeans 1902) found that perturbations longer than the Jeans wavelength λ_J were unstable. This corresponds to an unstable mass

$$M_J = \frac{4}{3}\pi\rho\left(\frac{\lambda_J}{2}\right)^3 \tag{1.4a}$$

$$= 9.0\left(\frac{T}{10\,\mathrm{K}}\right)^{3/2}\left(\frac{n}{10^3\,\mathrm{cm}^{-3}}\right)^{-1/2}\mathrm{M}_\odot\ , \tag{1.4b}$$

where the gas has been assumed to be isothermal and composed of hydrogen and helium in interstellar proportions. This Jeans analysis assumes an infinite, uniform initial state on which the linear analysis is performed. This is hardly a reasonable initial condition.

Bonnor (1956) and Ebert (1957) performed a stability analysis of an isothermal, nonrotating, nonmagnetic, gravitating spherical cloud in equilibrium and found that such a cloud would collapse if its mass exceeded a critical value given by

$$M_{\rm BE} = 1.18 \frac{C^4}{\left(G^3 P_{\rm ext}\right)^{1/2}} \tag{1.5a}$$

$$= 5.72 \left(\frac{T}{10\ {\rm K}}\right)^{3/2} \left(\frac{n}{10^3\ {\rm cm}^{-3}}\right)^{-1/2}\ {\rm M}_\odot\ , \tag{1.5b}$$

where $P_{\rm ext}$ is the external pressure, G is the gravitational constant, and C is the isothermal sound speed.

Based on the observed temperatures and masses of molecular clouds (10 K), they are incapable of being supported by their thermal pressure. Magnetic fields of magnitude comparable to that observed within molecular clouds, are capable of supporting the clouds against collapse. A cloud of mass M threaded by a magnetic flux Φ_B is stable against collapse provided that the mass-to-flux ratio M/Φ_B satisfies (Mouschovias and Spitzer 1976)

$$\frac{M}{\Phi_B} < \left(\frac{M}{\Phi_B}\right)_{\rm crit} \approx \frac{1}{\sqrt{63G}}\ . \tag{1.6}$$

Observations of magnetic fields in clouds indicate that they are either subcritical (i.e., capable of being supported by the magnetic field) or slightly supercritical (i.e., incapable of being supported by the magnetic field) (Crutcher 1999; Shu et al. 1999)[1]. Even if molecular clouds are magnetically subcritical as a whole, fragments within them can separate out and collapse due to the imperfect coupling between the neutral and charged matter. Under the action of their self-gravity, neutral particles can contract relative to the magnetic field lines (and the plasma), thereby forming supercritical fragments (or cores). The relative motion of the neutrals and the plasma is referred to as ambipolar diffusion.

[1]Crutcher (1999) contains an error in accounting for projection effects when calculating the flux. This error was corrected in Shu et al. (1999).

Mestel and Spitzer (1956) calculated the drift velocity $v_{\rm D}$ between the neutrals and the ions and found that

$$v_{\rm D} = \frac{|\,(\boldsymbol{\nabla} \times \boldsymbol{B}) \times \boldsymbol{B}|}{4\pi\rho_{\rm n} n_{\rm i} \sigma_{\rm in} v_{\rm n,T}}\ , \tag{1.7}$$

where $\rho_{\rm n}$, $n_{\rm i}$, and $\sigma_{\rm in}$ are the neutral mass density, the ion number density, and the ion-neutral collision cross section, respectively, and $v_{\rm n,T}$ is the thermal velocity. They realized that in clouds the ionization would decrease since the dust shields gas from the external ultraviolet light. This decrease in ionization results in a higher drift velocity and they thought the magnetic flux would escape the cloud, which would then collapse as a whole and undergo heirarchical fragmentation, as suggested by Hoyle (1953), and form stars.

The modern understanding (Mouschovias 1979) is that ambipolar diffusion redistributes mass within the central flux tubes of a cloud. Since the evelope of the cloud has a relatively high ionization, and, as a result, has a very long ambipolar diffusion timescales, it is difficult for the magnetic field lines to move through the envelope. As a result, ambipolar diffusion is only effective deep within the clouds.

Nakano and Tademaru (1972) mistakenly believed that the process of ambipolar diffusion was only important when the ambipolar diffusion timescale is comparable to the free-fall time. This is only so if star formation takes place on a free-fall time. Since molecular clouds are supported by magnetic fields, not their thermal pressure, the free-fall time is not the relevant timescale for star formation. Additionally, it has been claimed that ambipolar diffusion operates on timescales too long to be important in the fragmentation process, even if the star formation timescale is longer than the freefall timescale (Hartmann 2001). The ambipolar-diffusion timescale for a gravitating object is

$$\tau_{\rm AD} = 1.8 \times 10^6 \left(\frac{x_{\rm i}}{10^{-7}}\right)\ \ {\rm yr}\ , \tag{1.8}$$

where $x_{\rm i}$ is the degree of ionization (Mouschovias 1979). The actual timescale for star

formation can be a fraction or a multiple of this timescale depending on how close the cloud is to its critical state. Thus, ambipolar diffusion cannot be dismissed based on timescale arguments; moreover, since clouds are likely magnetically subcritical, ambipolar diffusion is both unavoidable and essential – unavoidable because of the small degree of ionization in the interiors of molecular clouds ($< 10^{-7}$), and essential because it is the only mechanism that can increase the mass-to-flux ratio at typical molecular cloud densities ($10^3 - 10^4$ cm^{-3}).

Morton (1991) performed a stability analyis of finite-thickness, magnetic thin disks[2] in order to determine their fragmentation properties. In this analysis, the wavelength of maximal growth rate was found to depend on the mass-to-flux ratio. For large mass-to-flux ratios, fragmentation occurs on the thermal lengthscale, as expected when the magnetic field is negligible. For very small mass-to-flux ratios, fragmentation again occurs on the thermal lengthscale; however, the timescale is increased since the neutrals must first diffuse through the magnetic field lines before becoming unstable and collape. For values of the mass-to-flux ratio near the critical value, the fragmentation scale increases and can be many times greater than the thermal wavelength. The degree to which the fragmentation scale increases depends on the collisional timescale between the neutrals and the ions, $\tau_{\rm ni}$ (see Fig. 1.3).

Kunz and Mouschovias (2009a) used this result to develop an analytical explanation for the initial mass function of fragments (or cores). By observing that in simulations of magnetically subcritical clouds (e.g. Fiedler and Mouschovias 1993; Desch and Mouschovias 2001) the magnetic field strength does not increase appreciably until the core becomes supercritical, they used the fact that the initial column density ($\sigma_{\rm n,0}$) could be related to the column density when the core becomes critical ($\sigma_{\rm n,cr}$) by

[2]In a thin disk model, the model cloud is assumed to be a sheet of thickness $2Z$. If the direction perpendicular to the sheet is z, there would be no variation in physical quantities along the z direction within the disk. Additionally, it is assumed that all physical quantities vary on scales larger than the half-thickness Z of the disk.

$$\sigma_{\rm n,cr} \approx \frac{\sigma_{\rm n,0}}{\mu_0} \ . \tag{1.9}$$

Using this result, the mass of a core relative to the thermal mass of the initial state is

$$\frac{m_{\rm c}}{m_{\rm T,0}} \approx \min\left(\mu_0, 1\right) \left(\frac{\lambda_{\rm fr}}{\lambda_{\rm T,0}}\right)^2 \ . \tag{1.10}$$

By assuming a distribution of mass-to-flux ratios, Kunz and Mouschovias (2009a) calculated a mass function (see Fig. 1.4) which agreed well with the observed distribution of core masses. The result is insensitive to the specific distribution of mass-to-flux ratios, provided that the range of values $\mu = 0.6$-1.0 is included.

1.2.2 Turbulence and MHD Waves

Without energy injection (driving), supersonic turbulence within molecular clouds dissipates quicky, often on the scale of the turbulent crossing time (Mestel 1965; Goldreich and Kwan 1974). Simulations of turbulence have found that, without energy injection (driving), this is in fact the case (Stone et al. 1998). If the cloud were supported primarily by turbulent pressure, it would quickly begin to collapse. This motivated the idea that molecular clouds are short-lived (Hartmann et al. 2001). However, this view is contradicted by the observed number of starless molecular clouds relative to those with embedded (proto)stars (Tassis and Mouschovias 2004; Mouschovias et al. 2006)[3] as well as by the star formation timescale [4] derived from the separation between the dust lanes and the first appearance of OB stars downstream from a galactic shock in spiral galaxies

[3]The relative abundance of starless molecular clouds $N_{\rm NS}$ to total number of molecular clouds $N_{\rm MC}$ should be proportional to the ratio of the cloud lifetime $\tau_{\rm MC}$ the star formation rate $\tau_{\rm SF}$:

$$\frac{N_{\rm NS}}{N_{\rm MC}} = \frac{\tau_{\rm SF}}{\tau_{\rm MC}} \ . \tag{1.11}$$

If only 10% of clouds in the solar neighborhood lack stars (Hartmann et al. 2001), then the lifetime of a molecular cloud is significantly longer than the star formation timescale, contradicting the claim that molecular clouds are short lived, transient objects, since typically $\tau_{\rm SF} > 1$ Myr.

[4]Mathewson et al. (1972) originally found a timescale of $6\,{\rm Myr}$; however, this number was revised to $12.5\,{\rm Myr}$ by Mouschovias et al. (2006) based on the updated distance to M51.

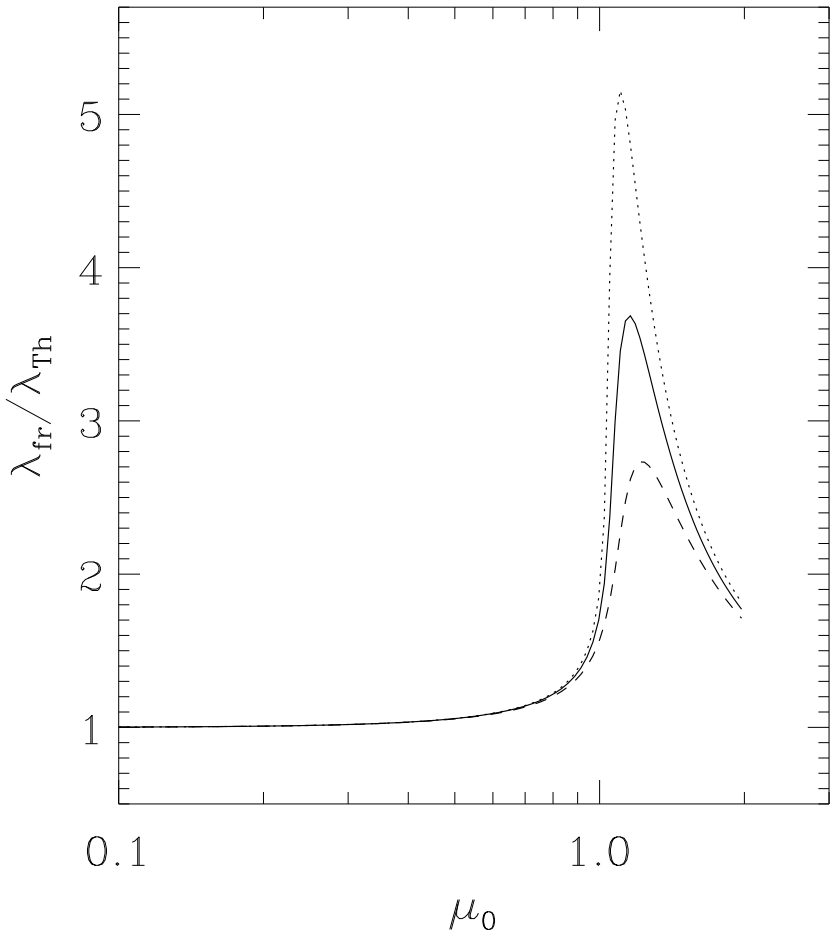

Figure 1.3: The fragmentation wavelength (normalized to the thermal wavelength) as a function of a cloud's mass-to-flux ratio for $\tau_{\rm ni} = 0.230$ (solid line), 0.162 (dashed line), and 0.325 (dotted line). The fragmentation wavelength is the wavelength with the largest growth rate (i.e., it increases in amplitude the fastest) as determined from a linear stability analysis.

(Mathewson et al. 1972).

The constant or periodic injection of energy and momentum can sustain turbulence over timescales longer than in the undriven case, and there are many simulations of core formation in the presence of driven turbulence (e.g., Padoan et al. 2001). Analysis of observational data (Brunt 2003) as well as comparison with simulations of driven turbulence (Ossenkopf and Mac Low 2002; Brunt et al. 2009) have found that driving of the turbulence most likely takes place at the largest scales. Although comparisons of the cores formed in simulations with driving at the largest scales and those with decaying turbulence have found differences, the differences are not significant enough to differentiate between the two possibilities on the basis of core properties alone(Offner et al. 2008b,a).

Arons and Max (1975) and Mouschovias (1975) proposed that the nonthermal motions could be explained by long-lived hydromagnetic waves in the cloud. Mouschovias (1987) showed that, if a cloud is magnetically supported and the waves within the cloud have an amplitude δB comparable to that of the cloud's mean field B, then the nonthermal velocity dispersion should be

$$(\Delta v)_{\rm NT} \approx 1.4 \left(\frac{B}{30\ \mu{\rm G}}\right)^{1/2} \left(\frac{R}{1\ {\rm pc}}\right)^{1/2}\ {\rm km\ s^{-1}}, \tag{1.12}$$

where R is the size of the observed object. Analysis of available observations found excellent agreement with equation (1.12) (Mouschovias and Psaltis 1995; Mouschovias et al. 2006).

Figure 1.5 (a) shows a plot of the linewidth versus size for those objects which have had their magnetic field measured. In Figure 1.5 (b), the same data have been plotted with the colors indicating the magnetic field strength, showing a clear dependence on the magnetic field strength. In Figure 1.6, the quantity $(\Delta v)_{\rm NT}/R^{1/2}$ has been plotted against the magnetic field strength B for the same objects. The solid line shows the relation predicted from Equation 1.12, and the dash line shows the fit to the data. The slight deviation between the theoretical prediction and the best fit to the data suggests that

the motions within the clouds are slightly subAlfvénic.

Although the nonthermal motions can be explained by magnetic waves, ambipolar diffusion will result in a cutoff wavelength $\lambda_{\rm A}$ where Alfvén waves of shorter wavelength ($\lambda < \lambda_{\rm A}$) cannot propagate in the neutrals. The Alfvén wavelength $\lambda_{\rm A}$ is given by

$$\lambda_{\rm A} \equiv \pi v_{\rm A} \tau_{\rm ni} \tag{1.13a}$$

$$= 0.29 \left(\frac{B}{30\,\mu{\rm G}}\right) \left(\frac{10^3\,{\rm cm}^{-3}}{n_{\rm n}}\right) \left(\frac{3\times10^{-3}\,{\rm cm}^{-3}}{K_{\rm CR}}\right)\,{\rm pc}, \tag{1.13b}$$

where $v_{\rm A} \equiv B/\sqrt{4\pi\rho_{\rm n}}$ is the Alvén speed, and $\tau_{\rm ni}$ is the collision time of a neutral particle in a sea of ions. $K_{\rm CR}$ is the cosmic-ray ionization constant (see §2.2). This lengthscale sets the dissipation scale for hydromagnetic waves within a molecular cloud; this cutoff can be see in observations of molecular clouds (Hezareh et al. 2010).

1.3 Previous Numerical Studies

Due to the nonlinear nature of the problem, numerical simulations are required in order to follow the evolution of a model cloud (on large lengthscales) and a collapsing core (on small lengthscales). Numerical simulations can be divided into two categories: those which follow the formation and evolution of an individual core and those which instead follow the early fragmentation of a cloud into several cores.

Calculations that follow the evolution of an individual core are primarily carried out in two dimensions using axisymmetry to reduce the dimensionality of the problem, with some simulations reducing the dimensionality further by considering finite-thickness thin disks. These simplifications are necessary because to follow the evolution of a collapsing core one must account for additional physics not present in the initial fragmentation stages.(Ciolek and Mouschovias 1993; Morton et al. 1994; Ciolek and Mouschovias 1994, 1995; Basu and Mouschovias 1994)

The first simulations of core formation in magnetically supported clouds included only neutrals, ions, and electrons (Fiedler and Mouschovias 1992). Through a slow progression, additional physics has been added: neutral and negatively-charged grains (Ciolek and Mouschovias 1993; Morton et al. 1994; Ciolek and Mouschovias 1994), ultraviolet ionizating radiation (Ciolek and Mouschovias 1995), rotation (Basu and Mouschovias 1994; Mellon and Li 2008, 2009; Dapp and Basu 2010), positively-charged grains (Desch and Mouschovias 2001), and radiative transfer (Kunz and Mouschovias 2009b, 2010).

Simulations of the early stages of star formation do not require the same assortment of physical processes included in the aformentioned simulations. For the most part, the physics is limited to either hydrodynamics or magnetohydrodynamics with gravity and, in some cases, nonideal MHD.

Since magnetically-supported molecular clouds are expected to be flattened objects, the dimensionality of the fragmentation problem can be reduced to two dimensions by assuming an infinitesimally thin sheet (Indebetouw and Zweibel 2000), or a finite-thickness thin sheet (e.g., Ciolek and Basu 2006). These simulations have been able to show that, as predicted by the linear analysis (see Fig. 1.3), the mean separation between cores increases as the mass-to-flux ratio approaches the critical value (Ciolek and Basu 2006; Basu et al. 2009b); however, this behavior is dominated by highly nonlinear velocity perturbations (Basu et al. 2009a). Kudoh and Basu (2008) performed three-dimensional simulations of sheets of gas initially in equilibrium, the three-dimensional analogue of the two-dimensional thin-disk models. These simulations yielded qualitatively similar results to the two-dimensional results, although, due to the small box size, they were not able to compare core statistics.

More extensive three dimensional simulations have been done by Nakamura and Li (2008). They performed a simulation of a magnetically subcritical ($\mu_0 = 0.91$) molecular cloud with a supersonic velocity perturbation. In their simulation, cores are presumed to turn into stars once they reach a critical density ($n \approx 10^5\,\mathrm{cm}^{-3}$), although they do

not acually model the accretion process. Instead, they employ CLUMPFIND to identify the core boundary. A predetermined fraction of the gas (and its associated momentum) inside the core are removed from the computational domain and turned into a Lagrangian particle. Although these particles do not acrete gas, they do inject energy back into the gas though jets and winds. This feedback replenishes energy lost to dissipation. They find the gas flattens to form a sheet which fragments into smaller, supercritical cores. The larger the initial velocity perturbation, the faster the first "stars" form; however, they do not observe significant differences in the overall efficiency of "star" formation. Additionally, the eventual reinjection of energy by jets results in a reduction in "star" formation at later stages.

Recently, studies of nonideal MHD turbulence have been completed using the ZEUS-MPAD code (Li et al. 2008; McKee et al. 2010). These simulations are limited in that they do not include any ion chemistry (the ions are instead subject to a continuity equation) and they do not include gravity. They assume that the effect of ambipolar diffusion driven by the magnetic field will be qualitatively similar to gravity-driven ambipolar diffusion, and attempt to analyze the resulting cores.

1.4 Requirements for a Model Cloud

Given the observations of molecular clouds, we study their fragmentation in three dimensions and perform a parameter study under the following requirements:

- *The model clouds must be magnetically subcritical.* Observations of molecular clouds indicate that they are likely magnetically subcritical. Despite this fact, the majority of simulations of molecular clouds assume that the clouds are supercritical. Since magnetically subritical clouds are stable against collapse in the limit of ideal MHD, ambipolar diffusion is necessary to initiate their evolution and fragmentation.

- *The model clouds must be isolated.* Periodic boundary conditions are commonly used in simulations of molecular clouds due to the computational ease associated with calculating the gravitational potential using fast Fourier transform (FFT) methods. However, periodic boxes artificially prevent the global collapse of a cloud.[5] By using isolated boundary conditions on the gravitational potential we allow for the possibility of global gravitational collapse of the model clouds.

- *The velocity perturbation should be, at most, transAlfvénic.* The observed velocity dispersion within star-forming regions are subAlfvénic. Although these observations are of regions where prestellar objects have already formed, there is evidence that the turbulent properties of clouds without active star formation are similar to those with active star formation (Heyer et al. 2006).

[5]Turbulence offers only temporary support against collapse because it dies out quickly.

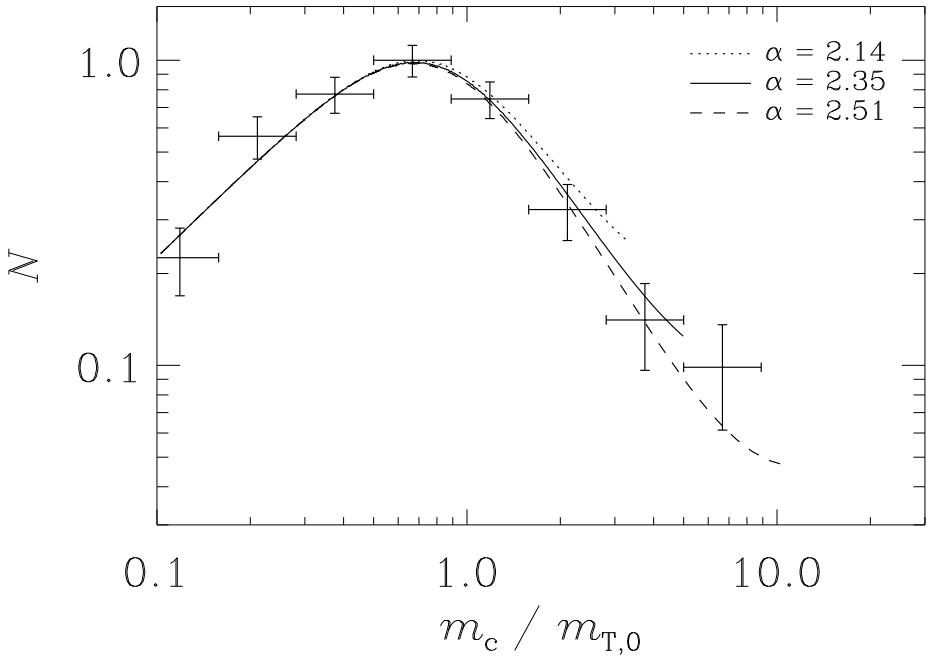

Figure 1.4: The Kunz-Mouschovias core mass function for $\tau_{\rm ni} = 0.230$ (solid line), 0.162 (dashed line), and 0.325 (dotted line). The data from Orion (Nutter and Ward-Thompson 2007) are overplotted. For a complete discussion, see Kunz and Mouschovias (2009a).

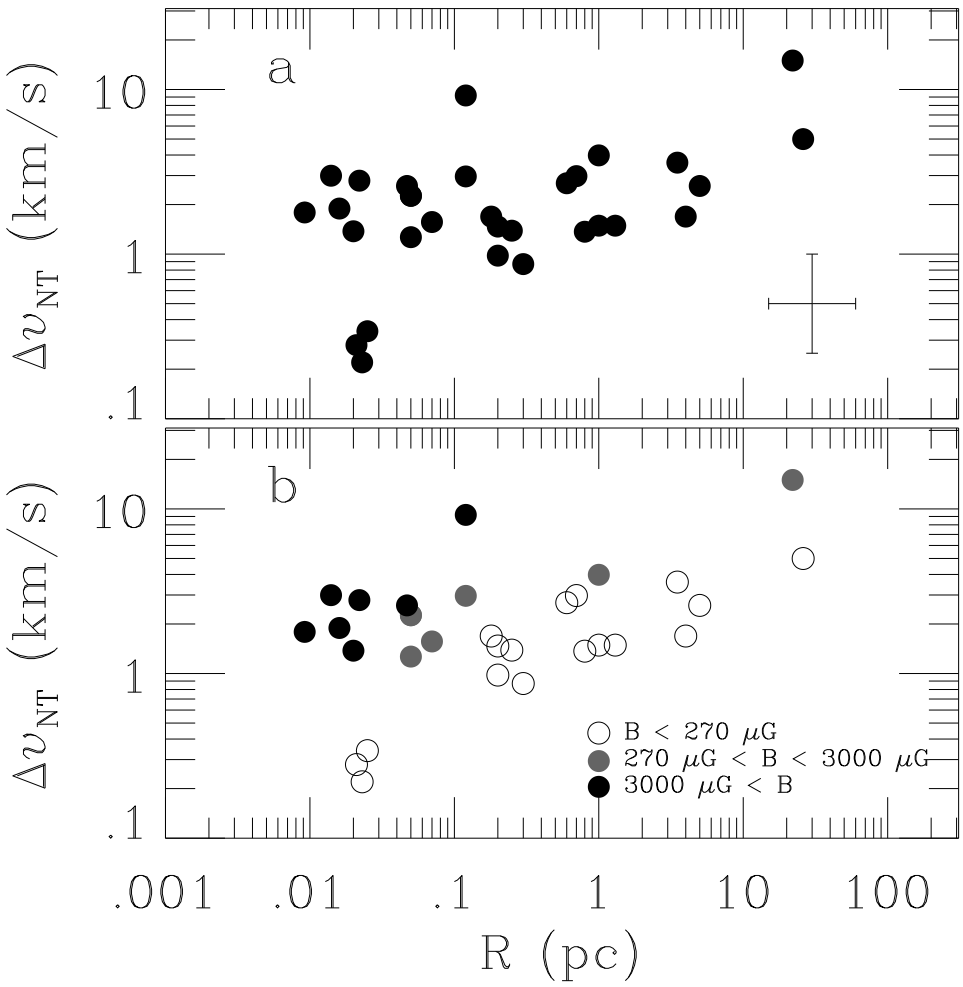

Figure 1.5: Linewidth versus size for objects which also have a measured magnetic field. The bottom frames show the same data; however, in the bottom plot the points are color-coded based on their magnetic field strength.

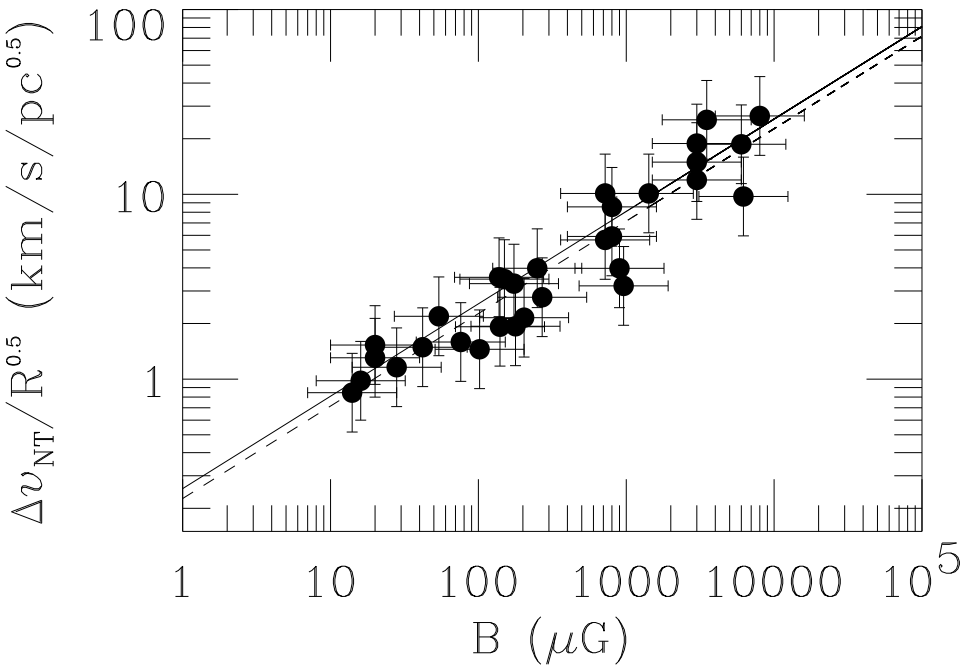

Figure 1.6: $\Delta v_{\rm NT}/R^{1/2}$ versus the observed magnetic field B. The solid line is the predicted relation from equation 1.12. The dashed line is the least-squares fit to the data.

Chapter 2

Formulation of the Problem

In this chapter we outline the physics of two-fluid magnetohydrodynamics (§2.1) and the chemical model used to determine the ionization fraction (§2.2). Molecular clouds are weakly-ionized gaseous systems consisting of neutral hydrogen and helium, as well as heavier atoms and molecules in much smaller abundances. Ions within a cloud couple to the magnetic field and, through their collisional interactions with the neutrals, transmit the Lorentz force to the neutrals. The relevant equations are summarized (§2.3).

2.1 Two-Fluid Magnetohydrodynamics

Molecular clouds can be described as a weakly-ionized plasma evolving under the laws of magnetohydrodynamics. The neutral gas satisfies a continuity equation

$$\frac{\partial \rho_{\rm n}}{\partial t} + \boldsymbol{\nabla} \cdot (\rho_{\rm n} \boldsymbol{v}_{\mathbf{n}}) = 0, \tag{2.1}$$

where $\boldsymbol{v}_{\mathbf{n}}$ is the velocity and $\rho_{\rm n}$ is the density of neutrals. The neutrals only experience their own pressure P, gravity $\boldsymbol{g}$, and the frictional drag forces with ions ($\boldsymbol{F}_{\mathbf{ni}}$) and electrons ($\boldsymbol{F}_{\mathbf{ne}}$). It is through this frictional coupling that the neutrals experience the magnetic force:

$$\frac{\partial (\rho_{\rm n} \boldsymbol{v}_{\mathbf{n}})}{\partial t} + \boldsymbol{\nabla} \cdot (\rho_{\rm n} \boldsymbol{v}_{\mathbf{n}} \boldsymbol{v}_{\mathbf{n}}) = -\boldsymbol{\nabla} P + \rho_{\rm n} \boldsymbol{\nabla} \Psi + \boldsymbol{F}_{\mathbf{ni}} + \boldsymbol{F}_{\mathbf{ne}} \, . \tag{2.2}$$

The gravitational potential Ψ is the solution to the Poisson equation,

$$\nabla^2 \Psi = 4\pi G \rho_{\rm n} \ . \tag{2.3}$$

Due to the negligible contribution of the ions and electrons to the total density, their contribution in equation 2.3 has been ignored.

Unlike the neutrals, the ions do not satisfy a similar continuity equation. The number of ions depends primarily on the equilibrium chemistry (see §2.2), and so no continuity equation is required for them. Additionally, the ions and electrons are assumed to be at their terminal velocity

$$0 = e n_{\rm i} \left(\boldsymbol{E} + \frac{\boldsymbol{v_{\rm i}}}{c} \times \boldsymbol{B} \right) + \boldsymbol{F_{\rm in}} \ , \tag{2.4a}$$

$$0 = -e n_{\rm e} \left(\boldsymbol{E} + \frac{\boldsymbol{v_{\rm e}}}{c} \times \boldsymbol{B} \right) + \boldsymbol{F_{\rm en}} \ , \tag{2.4b}$$

where e is the charge of an electron and $n_{\rm i}$ and $n_{\rm e}$ are the number densities of the ions and electrons, respectively. The frictional force (per unit volume) on a species s due to collisions with the neutrals is given by

$$\boldsymbol{F_{sn}} = \frac{\rho_{\rm s}}{\tau_{sn}} \left(\boldsymbol{v_{\rm n}} - \boldsymbol{v_s} \right) \ , \tag{2.5}$$

where the momentum exchange timescale is given by

$$\tau_{sn} = a_{\rm He-s} \frac{m_{\rm H_2} + m_s}{\rho_{\rm n} \langle \sigma_{\rm coll} w \rangle_{s\rm H_2}} \ . \tag{2.6}$$

The factor $a_{\rm He-s}$ is a correction factor for the presence of helium in addition to the hydrogen in the neutral gas, and is given by (see Mouschovias (1996))

$$a_{\rm He-s} = \begin{cases} 1.23 & s = {\rm i} \\ 1.21 & s = {\rm e} \end{cases} \ . \tag{2.7}$$

The collisional rate $\langle \sigma_{\rm coll} w \rangle_{\rm sH_2}$ is 1.69×10^{-9} cm^3 s^{-1} for $\rm HCO^+$ with a similar value for

Na^+ and Mg^+ (McDaniel and Mason 1973) and $1.3 \times 10^{-9}\ \mathrm{cm}^3\,\mathrm{s}^{-1}$ for electrons (Mott and Massey 1987).

By introducing the electric field in the frame of the neutrals,

$$\boldsymbol{E_n} \equiv \boldsymbol{E} + \boldsymbol{v_n} \times \boldsymbol{B}/c\,, \tag{2.8}$$

equations 2.4 can be rewritten as

$$0 = en_\mathrm{i}\left(\boldsymbol{E_n} + \frac{\boldsymbol{v_i} - \boldsymbol{v_n}}{c} \times \boldsymbol{B}\right) + \frac{\rho_\mathrm{i}}{\tau_\mathrm{in}}\left(\boldsymbol{v_n} - \boldsymbol{v_i}\right) \tag{2.9a}$$

$$0 = -en_\mathrm{e}\left(\boldsymbol{E_n} + \frac{\boldsymbol{v_e} - \boldsymbol{v_n}}{c} \times \boldsymbol{B}\right) + \frac{\rho_\mathrm{e}}{\tau_\mathrm{en}}\left(\boldsymbol{v_n} - \boldsymbol{v_e}\right)\ . \tag{2.9b}$$

The force law can now be expressed in terms of the velocities of the ions and electrons relative to the neutrals. We introduce $\boldsymbol{w_i} \equiv \boldsymbol{v_i} - \boldsymbol{v_n}$ and $\boldsymbol{w_e} \equiv \boldsymbol{v_e} - \boldsymbol{v_n}$. The electric field $\boldsymbol{E_n}$ can be obtained by using Equation 2.9 and the current density

$$\boldsymbol{j} = n_\mathrm{i} e \boldsymbol{w_i} - n_\mathrm{e} e \boldsymbol{w_e}\,. \tag{2.10}$$

Written in terms of the current parallel ($\boldsymbol{j}_\parallel$) and perpendicular ($\boldsymbol{j}_\perp$) to the magnetic field, the electric field $\boldsymbol{E_n}$ becomes

$$\boldsymbol{E_n} = \eta_\parallel \boldsymbol{j}_\parallel + \eta_\perp \boldsymbol{j}_\perp + \eta_\mathrm{H} \boldsymbol{j}_\perp \times \hat{\boldsymbol{e}}_\mathbf{B}\ , \tag{2.11}$$

where $\hat{\boldsymbol{e}}_\mathbf{B}$ is a unit vector in the direction of the magnetic field $\boldsymbol{B}$. The resistivities $\eta_\parallel$, $\eta_\perp$, and the Hall resistivity η_H are given by

$$\eta_\parallel = \frac{1}{\sigma_\parallel}\,, \tag{2.12a}$$

$$\eta_\perp = \frac{\sigma_\perp}{\sigma_\perp + \sigma_\mathrm{H}}\,, \tag{2.12b}$$

$$\eta_{\rm H} = \frac{\sigma_{\rm H}}{\sigma_\perp + \sigma_{\rm H}} \,, \tag{2.12c}$$

where

$$\sigma_\parallel = \sum_s \sigma_s \,, \tag{2.13a}$$

$$\sigma_\perp = \sum_s \frac{\sigma_s}{1 + \left(\omega_s \tau_s\right)^2} \,, \tag{2.13b}$$

$$\sigma_{\rm H} = \sum_s \frac{\sigma_s \omega_{\rm s} \tau_{n{\rm s}}}{1 + \left(\omega_s \tau_s\right)^2} \,, \tag{2.13c}$$

where $\sigma_s = n_s e^2 \tau_{\rm sn}/m_s$ is the conductivity of species s, and the cyclotron frequency of species s is given by $\omega_s = eB/m_s c$.

Faraday's Law,

$$\frac{\partial \boldsymbol{B}}{\partial t} = -c\boldsymbol{\nabla} \times \boldsymbol{E} \,, \tag{2.14}$$

can now be written in its final form using equations 2.8 and 2.11,

$$\frac{\partial \boldsymbol{B}}{\partial t} - \boldsymbol{\nabla} \times \left(\boldsymbol{v}_{\mathbf{n}} \times \boldsymbol{B}\right) = -c\boldsymbol{\nabla} \times \left(\eta_\parallel \boldsymbol{j}_\parallel + \eta_\perp \boldsymbol{j}_\perp + \eta_{\rm H} \boldsymbol{j}_\perp \times \hat{\boldsymbol{e}}_{\mathbf{B}}\right) \,. \tag{2.15}$$

Finally, the system is closed using Ampere's Law

$$\boldsymbol{j} = \frac{c}{4\pi} \boldsymbol{\nabla} \times \boldsymbol{B} \,. \tag{2.16}$$

The force on the neutrals due to collisions with the ions and electrons, $\boldsymbol{F}_{\mathbf{ni}} + \boldsymbol{F}_{\mathbf{ne}}$, can now be eliminated from equation 2.2, to find that

$$\frac{\partial (\rho_{\rm n} \boldsymbol{v}_{\mathbf{n}})}{\partial t} + \boldsymbol{\nabla} \cdot (\rho_{\rm n} \boldsymbol{v}_{\mathbf{n}} \boldsymbol{v}_{\mathbf{n}}) = -\boldsymbol{\nabla} P + \rho_{\rm n} \boldsymbol{\nabla} \Psi + \frac{1}{4\pi} \left(\boldsymbol{\nabla} \times \boldsymbol{B}\right) \times \boldsymbol{B} \,. \tag{2.17}$$

2.2 The Chemical Model

Within the density range of interest, the dominant source of ionization is high-energy (> 100 MeV) cosmic rays penetrating deep into the cloud. Significant attenuation of these particles occurs only at column densities $\gtrsim 96\,\mathrm{g/cm^3}$, much higher than the column densities relevant to fragmentation of molecular clouds. Although cosmic-ray ionization results in molecular ions (see Table 2.1), these are neutralized through charge transfer on timescales much shorter than the dynamical timescale. Since the timescale on which these reactions occur is much shorter than the evolutionary timescale of the system, we can safely assume that the chemical abundances are in equilibrium.

The equilibrium values can be calculated by equating the rate of ion formation to the rate of dissociative and radiative recombination:

$$\zeta_{\rm CR} n_{\rm n} = x_e \left(\alpha_{\rm dr} x_{\rm m+} + \alpha_{\rm rr} x_{\rm a+}\right) n_{\rm n}^2 \tag{2.18a}$$

$$\zeta_{\rm CR} n_{\rm n} = x_{m+} \left(\alpha_{\rm dr} x_{\rm e} + \beta x_{\rm a_0}\right) n_{\rm n}^2 \,, \tag{2.18b}$$

where $\zeta_{\rm CR}$ is the cosmic-ray ionization rate, $\alpha_{\rm dr}$ is the dissociative recombination rate, $\alpha_{\rm rr}$ is the radiative recombination rate, and β is the charge transfer rate (see Table 2.1). $x_{\rm e}$ ($\equiv n_{\rm e}/n_{\rm n}$), x_{a+} ($\equiv n_{\rm a+}/n_{\rm n}$), and $x_{\rm m+}$ ($\equiv n_{\rm m+}/n_{\rm n}$) are the abundances of the electrons, atomic ions, and molecular ions, respectively, relative to the neutrals.

Over the range of densities of interest here ($10^3 - 10^6\ \mathrm{cm^{-3}}$), the number of ions can be approximated by a power law (Fiedler and Mouschovias 1992)

$$n_{\rm i} = K_{\rm CR} \left(\frac{n_{\rm n}}{10^5\,\mathrm{cm^{-3}}}\right)^{1/2} \,, \tag{2.19}$$

where $K_{\rm CR} \approx \left(10^5 \zeta/\alpha_{\rm dr}\right)^{1/2}$.

For intermediate densities, high-energy cosmic rays will account for most of the ion-

ization; however, at densities below $10^4\,\mathrm{cm}^{-3}$ it is possible for UV to penetrate into the cloud and directly ionize atomic species such as sulfur, iron, silicon, carbon, and magnesium greatly increasing the ionization in the low-density envelope. Although it has been found that UV radiation does not affect the evolution of central quantities, the increased coupling between the magnetic field and the neutral matter in the envelope renders the ambipolar-diffusion timescale too long to be of relevance in the evolution of molecular cloud envelopes (Ciolek and Mouschovias 1995). Direct calculation of the UV ionization in three dimensions is computationally expensive. Instead, we follow Fiedler and Mouschovias (1992) and introduce a second term in the ionization-equilibrium equation,

$$n_{\mathrm{i}} = K_{\mathrm{CR}} \left(\frac{n_{\mathrm{n}}}{10^5\,\mathrm{cm}^{-3}} \right)^{1/2} + K_{\mathrm{UV}} \left(\frac{10^3\,\mathrm{cm}^{-3}}{n_{\mathrm{n}}} \right)^2 , \tag{2.20}$$

which mimics the effect of UV ionization in the cloud envelopes. The typical value for K_{UV} is $4.68 \times 10^{-4}\,\mathrm{cm}^{-3}$ (Fiedler and Mouschovias 1992). In addition to this, we apply a cap on the ionization of 10^{-4}. Figure 2.1 shows the ionization $x_{\mathrm{i}} \equiv n_{\mathrm{i}}/n_{\mathrm{n}}$ over the range of densities investigated in the problem.

2.3 Summary of the MHD Equations

For reference, the equations that govern the model clouds are summarized here. The quantities ρ_{n}, $\boldsymbol{v}_{\mathbf{n}}$, $\boldsymbol{B}$, and $\boldsymbol{j}$ are the neutral density, neutral velocity, magnetic field, and current density, respectively.

$$\frac{\partial \rho_{\mathrm{n}}}{\partial t} + \boldsymbol{\nabla} \cdot (\rho_{\mathrm{n}} \boldsymbol{v}_{\mathbf{n}}) = 0, \tag{2.21a}$$

$$\frac{\partial (\rho_{\mathrm{n}} \boldsymbol{v}_{\mathbf{n}})}{\partial t} + \boldsymbol{\nabla} \cdot (\rho_{\mathrm{n}} \boldsymbol{v}_{\mathbf{n}} \boldsymbol{v}_{\mathbf{n}}) = -\boldsymbol{\nabla} P + \rho_{\mathrm{n}} \boldsymbol{\nabla} \Psi + \frac{1}{4\pi} (\boldsymbol{\nabla} \times \boldsymbol{B}) \times \boldsymbol{B} \, . \tag{2.21b}$$

$$\frac{\partial \boldsymbol{B}}{\partial t} - \boldsymbol{\nabla} \times (\boldsymbol{v}_{\mathbf{n}} \times \boldsymbol{B}) = -c \boldsymbol{\nabla} \times \left(\eta_{\parallel} \boldsymbol{j}_{\parallel} + \eta_{\perp} \boldsymbol{j}_{\perp} + \eta_{\mathrm{H}} \boldsymbol{j}_{\perp} \times \hat{\boldsymbol{e}}_{\mathbf{B}} \right) \, . \tag{2.21c}$$

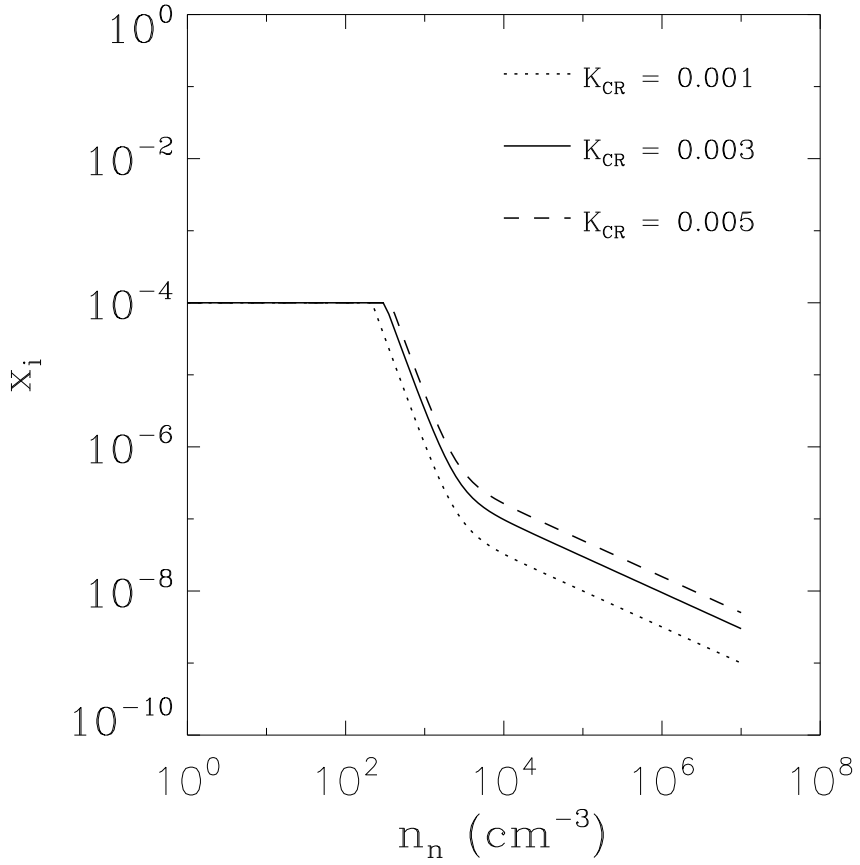

Figure 2.1: Ionization versus volume density for the three values of $K_{\rm CR}$ used in the parameter study.

$$\nabla^2 \Psi = 4\pi G \rho_{\rm n} \, . \tag{2.21d}$$

$$n_{\rm i} = K_{\rm CR} \left(\frac{n_{\rm n}}{10^5 \, {\rm cm}^{-3}} \right)^{1/2} + K_{\rm UV} \left(\frac{10^3 \, {\rm cm}^{-3}}{n_{\rm n}} \right)^2 \, , \tag{2.21e}$$

$$\boldsymbol{j} = \frac{c}{4\pi} \boldsymbol{\nabla} \times \boldsymbol{B} \tag{2.21f}$$

$$\eta_{\parallel} = \frac{1}{\sigma_{\parallel}} \, , \tag{2.21g}$$

$$\eta_{\perp} = \frac{\sigma_{\perp}}{\sigma_{\perp} + \sigma_{\rm H}} \, , \tag{2.21h}$$

$$\eta_{\rm H} = \frac{\sigma_{\rm H}}{\sigma_{\perp} + \sigma_{\rm H}} \, , \tag{2.21i}$$

$$\sigma_{\parallel} = \sum_s \sigma_s \, , \tag{2.21j}$$

$$\sigma_{\perp} = \sum_s \frac{\sigma_s}{1 + \left(\omega_s \tau_s \right)^2} \, , \tag{2.21k}$$

$$\sigma_{\rm H} = \sum_s \frac{\sigma_s \omega_{\rm s} \tau_{n{\rm s}}}{1 + \left(\omega_s \tau_s \right)^2} \, , \tag{2.21l}$$

Table 2.1: Chemical Reaction Network Used To Determine Ionization Fraction

	Reaction			Rate Constant	Value
Cosmic Ray Ionization	$CR + H_2$	$\rightarrow$	$H_2^+ + e_-$		
	$H_2^+ + H_2$	$\rightarrow$	$H_3^+ + H$		
	$H_3^+ + CO$	$\rightarrow$	$HCO^+ + H_2$	ζ	$5 \times 10^{-17}\,s^{-1}$
Charge Transfer	$HCO^+ + Na$	$\rightarrow$	$HCO + Na^+$	β	$2.5 \times 10^{-9}\,s^{-1}$
Dissociative Recombination	$HCO^+ + e^-$	$\rightarrow$	$H + CO$	α_{dr}	$2.0 \times 10^{-7}\left(\frac{T}{300\,K}\,s^{-1}\right)$
Radiative Recombination	$Na^+ + e^-$	$\rightarrow$	$Na + \gamma$	α_{rr}	$2.8 \times 10^{-12}\left(\frac{T}{300\,K}\right)\,s^{-1}$

Chapter 3

The Model Cloud

3.1 Initial Conditions

We consider model clouds with a density distribution $\rho_{\rm n}(r)$ given by

$$\rho_n(r) = \begin{cases} \rho_{n,0} & r < R_0 \\ \rho_{n,0} \exp\left(-(r-R_0)^2/a^2\right) & r \geq R_0 \ , \end{cases} \tag{3.1}$$

where r is the cylindrical polar radius. The constants R_0 and a are chosen such that there are at least several Jeans masses within the central region and the density at the boundary is sufficiently small. The region $r > R_0$ acts as a low density buffer separating the cloud from the effects of the boundary of the computational domain. The initial magnetic field is $\boldsymbol{B} = B_0 \hat{\boldsymbol{e}}_z$. For a typical model cloud, the density is $\rho_{\rm n} = 300\,{\rm cm}^{-3}$, the temperature $T = 10\,K$, and the magnetic field $B_0 = 16\,\mu{\rm G}$.

The true initial condition for the simulation should be a cloud in equilibrium, supported by both turbulent, thermal, and magnetic forces. To find this equilibrium, we assume an equation of state that includes the contribution of turbulent velocity,

$$P = \left(C^2 + v_{\rm turb}^2\right) \rho \, . \tag{3.2}$$

For a typical run, the value of $v_{\rm turb}$ is $2.0\,C$, twice the isothermal sound speed. We then allow the model cloud to relax to an equilibrium state under flux-freezing. The equilibrium found through this process becomes the initial state for the simulation. At the beginning of the simulation, the velocity field is reinitialed, the equation of state is

$P = C^2 \rho_{\rm n}$, and the model cloud is allowed to evolve under nonideal MHD.

The velocity perturbation is divided into two parts,

$$\boldsymbol{v}(\boldsymbol{x}) = \boldsymbol{v}_{\rm turb}(\boldsymbol{x}) + \boldsymbol{v}_{\rm sol}(\boldsymbol{x})\,. \tag{3.3}$$

The first term, $\boldsymbol{v}_{\rm turb}(\boldsymbol{x})$, is a randomly oriented vector at $\boldsymbol{x}$ with magnitude $v_{\rm turb}$. This perturbation will approximate the turbulent pressure support used in finding the initial equilibrium. The second term, $\boldsymbol{v}_{\rm sol}(\boldsymbol{x})$, is a solenoidal velocity field approximating large-scale velocity gradients within the model cloud. Since observations (e.g. Ossenkopf and Mac Low 2002) indicate most of the energy is at large scales, the solenoidal perturbation scales as

$$v_{\rm sol}^2(k) \propto \frac{1}{k^\alpha} \tag{3.4}$$

where α is 4 in our fidducial case. The exponent $\alpha > 0$ ensures that most of the energy is at the largest scales, as observed. The solenoidal contribution is normalized so that the RMS contribution is $v_{\rm sol}$.

3.2 Boundary Conditions

Since we are modelling an isolated cloud, we must choose consistent boundary conditions for the six boundaries of the computational domain located at $x = \pm X$, $y = \pm Y$, and $z = \pm Z$.

For the hydrodynamic variables ($\rho_{\rm n}$ and $\boldsymbol{v}_{\mathbf{n}}$) we impose reflective boundary conditions on all the boundaries. If, for example, the boundary was located at $x = 0$, the boundary conditions would take the form:

$$\rho_{\rm n}(-X - \epsilon, y, z) = \rho_{\rm n}(-X + \epsilon, y, z) \tag{3.5a}$$

$$v_{\mathrm{n,x}}(-X-\epsilon,y,z) = -v_{\mathrm{n,x}}(-X+\epsilon,y,z) \tag{3.5b}$$

$$v_{\mathrm{n,y}}(-X-\epsilon,y,z) = v_{\mathrm{n,y}}(-X+\epsilon,y,z) \tag{3.5c}$$

$$v_{\mathrm{n,z}}(-X-\epsilon,y,z) = v_{\mathrm{n,z}}(-X+\epsilon,y,z)\ . \tag{3.5d}$$

This set of boundary conditions implies that the component of the velocity perpendicular to the boundary vanishes and, as a result, prevents matter from entering or leaving the computational domain.

For the magnetic field variables, we impose different sets of boundary conditions depending on the boundary. For the x- and y-boundaries, we impose the reflective boundary conditions used for the velocity.

$$B_{\mathrm{n,x}}(-X-\epsilon,y,z) = -B_{\mathrm{n,x}}(-X+\epsilon,y,z) \tag{3.6a}$$

$$B_{\mathrm{n,y}}(-X-\epsilon,y,z) = B_{\mathrm{n,y}}(-X+\epsilon,y,z) \tag{3.6b}$$

$$B_{\mathrm{n,z}}(-X-\epsilon,y,z) = B_{\mathrm{n,z}}(-X+\epsilon,y,z)\ . \tag{3.6c}$$

This makes the magnetic field components perpendicular to the boundary vanish and prevents flux from crossing these boundaries. For the Z-boundaries, we cannot use the same boundary conditions since our initial state will have a flux across these boundaries. Instead, we impose the condition that the field lines must be perpendicular to the boundary, $B_x(x,y,\pm Z) = 0$, $B_y(x,y,\pm Z) = 0$.

$$B_{\mathrm{n,x}}(x,y,+Z+\epsilon) = -B_{\mathrm{n,x}}(x,y,+Z-\epsilon) \tag{3.7a}$$

$$B_{\mathrm{n,y}}(x,y,+Z+\epsilon) = -B_{\mathrm{n,y}}(x,y,+Z-\epsilon) \tag{3.7b}$$

$$B_{\mathrm{n,z}}(x,y,+Z+\epsilon) = B_{\mathrm{n,z}}(x,y,+Z-\epsilon)\ . \tag{3.7c}$$

This ensures that the magnetic flux through the boundaries at $z = \pm Z$ is constant through-

out the simulation.

The boundary conditions for derived quantities such as $\rho_{\rm i}$, $\eta_{\parallel}$, $\eta_{\perp}$, $\eta_{\rm H}$, etc. acquire their boundary values from those quantities from which they are derived.

In addition to these boundary conditions, we impose a floor on the value of the density at $n = 1\,{\rm cm}^{-3}$. This prevents the Alfvén speed in the low-density gas from becoming too large, resulting in numerical problems.

3.3 Parameter Study

We perform a number of simulations varying the initial mass-to-flux ratio μ_0, the ionization constant $K_{\rm CR}$, the solenoidal velocity perturbation $v_{\rm sol}$, and the turbulent support perturbation $v_{\rm turb}$.

To study the effect of the mass-to-flux ratio, we consider three values: $\mu_0 = 0.9$, 0.75, and 0.5. Mass-to-flux ratios less than 0.5 are not expected to have quantitative differences from those at $\mu_0 = 0.5$. Runs with initially supercritical mass-to-flux ratios are not investigated since these model clouds would not be in equilibrium and would require a different initial state at the start of the simulation. Additionally, it should be noted that since runs farther from critical take longer to develop supercritical cores, there will be fewer runs with $\mu_0 = 0.5$ due to CPU time limitations.

The ionization constant $K_{\rm CR}$ can take on three different values, with $K_{\rm CR} = 3 \times 10^{-3}$ being the fiducial case. We also consider the case of lower ionization constant $K_{\rm CR} = 1 \times 10^{-3}$ and a higher ionization constant $K_{\rm CR} = 5 \times 10^{-3}$ (see Fig. 2.1).

The turbulent support contribution $v_{\rm turb}$ can take the value $v_{\rm turb} = 0.0$ or $v_{\rm turb} = 2C$. A larger value for $v_{\rm turb}$ results in a more extended initial cloud. These extended clouds have more mass near the computational boundary, increasing the influence the boundary has on the evolution of the cloud. For this reason, we do not study larger values of $v_{\rm turb}$.

For the solenoidal velocity perturbation, $v_{\rm sol}$, we study a wider range of perturbations,

ranging from $v_{\rm sol} = 0.5C$ to $v_{\rm sol} = 4.0C$. These values range from subsonic to trans-Alfvénic, the range of values expected in molecular clouds.

We also perform simulations at two different resolutions. High resolution runs (those with the 'H' prefix in Table 3.3) have a central grid spacing of $0.01\,\mathrm{pc}$, while low resolution runs (those with the 'L' prefix) have a central grid spacing of $0.02\,\mathrm{pc}$.

Table 3.1: Runs

Run	Initial μ_0	$K_{\rm CR}$	$v_{\rm turb}\,(C)$	$v_{\rm sol}\,(C)$
H1	0.75	1×10^{-3}	1.0	1.0
H2	0.75	3×10^{-3}	1.0	1.0
H3	0.90	3×10^{-3}	2.0	2.0
L16	0.50	1×10^{-3}	1.0	1.0
L15	0.50	3×10^{-3}	1.0	1.0
L27	0.50	3×10^{-3}	0.0	0.3
L22	0.50	5×10^{-3}	0.0	2.0
L11	0.75	1×10^{-3}	1.0	1.0
L12	0.75	1×10^{-3}	1.0	1.0
L17	0.75	3×10^{-3}	1.0	0.5
L28	0.75	5×10^{-3}	0.0	2.0
L29	0.75	5×10^{-3}	0.0	0.5
L13	0.90	1×10^{-3}	1.0	1.0
L20	0.90	3×10^{-3}	0.0	0.5
L14	0.90	3×10^{-3}	1.0	1.0
L26	0.90	3×10^{-3}	2.0	0.5
L25	0.90	3×10^{-3}	2.0	2.0
L24	0.90	3×10^{-3}	2.0	4.0
L21	0.90	5×10^{-3}	2.0	4.0
L23	0.90	5×10^{-3}	2.0	2.0

Chapter 4

Implementation

4.1 Multiprocessor Communication

The problem we are attempting to solve would be intractable without the use of multiple processors. By using multiple processors and MPI (*Message Passing Interface*) communication, the computational domain can be subdivided into multiple rectangular subdomains with a single processor responsible for each subdomain. Using MPI, the values of physical variables along shared faces – *ghost zones* – can be passed from one processor to the neighboring processor. To balance the computational load across these processors, the number of zones assigned to each processor is equal. Since the grid is nonuniform, this does not correspond to each processor being assigned an equal volume of the computational domain.

4.2 Overview of Code Structure

We provide an overview of the structure of the ZEUS-MP code and the relevant routines. We will not cover the initialization routines, just the main loop which evolves the system. A flow chart can be found in Figure 4.1. Routines which are never used, such as the radiative transport routines, are omitted.

The first step is to calculate the gravitational potential (Step *Gravity* in Figure 4.1). Before the calculation can be done, the gravitational potential on the boundary must be specified. This is done in the routine **gpbv3d** (see §4.4 for details of this routine). Once

the potential on the boundary has been specified, the conjugate gradient (CG) solver solves for the potential at all zones within the computational domain (relevant routine: **grav3d_cg**).

After the gravitational potential has been calculated, the source step is applied (*Source Step* in Figure 4.1). This step serves two purposes. First, it updates the fluid velocity using the pressure, gravitational, and magnetic forces (relevant routine: **forces_d**). Second, it updates the magnetic field using the nonideal routines (relevant routine: **ctod**; see §4.5).

Next, the transport step is applied (*Transport* in Figure 4.1). This updates the fluid variables using van Leer advection (relevant routine: **transprt_3d**) and the magnetic field using constrained transport (relevant routine: **ct**).

Once the fluid variables have been updated, a new timestep can be calculated (*Timestep* in Figure 4.1. The relevant routines are **newdt** and **nudt**.

Finally, if data needs to be output, it is (relevant routine: **dataio**), and the cycle starts anew.

4.3 The Grid

Zeus-MP employs a control volume approach where the physical variables are solved on two staggered grids. The velocity $\boldsymbol{v}$ and magnetic field $\boldsymbol{B}$ components are located on the zone faces, and the density ρ is located at zone center (see Figure (4.4)). This staggered grid approach reduces the number of interpolations in the differencing of the equations of motion and ensures that the magnetic field remains divergence-free (to machine accuracy).

Although Zeus does not support adaptive mesh refinement (AMR), the fact that we are simulating an isolated object allows for a nonuniform grid to be employed, greatly reducing the computational requirements. Since the model cloud is expected to flatten along the field lines, the grid is nonuniform in the direction of the initial magnetic field,

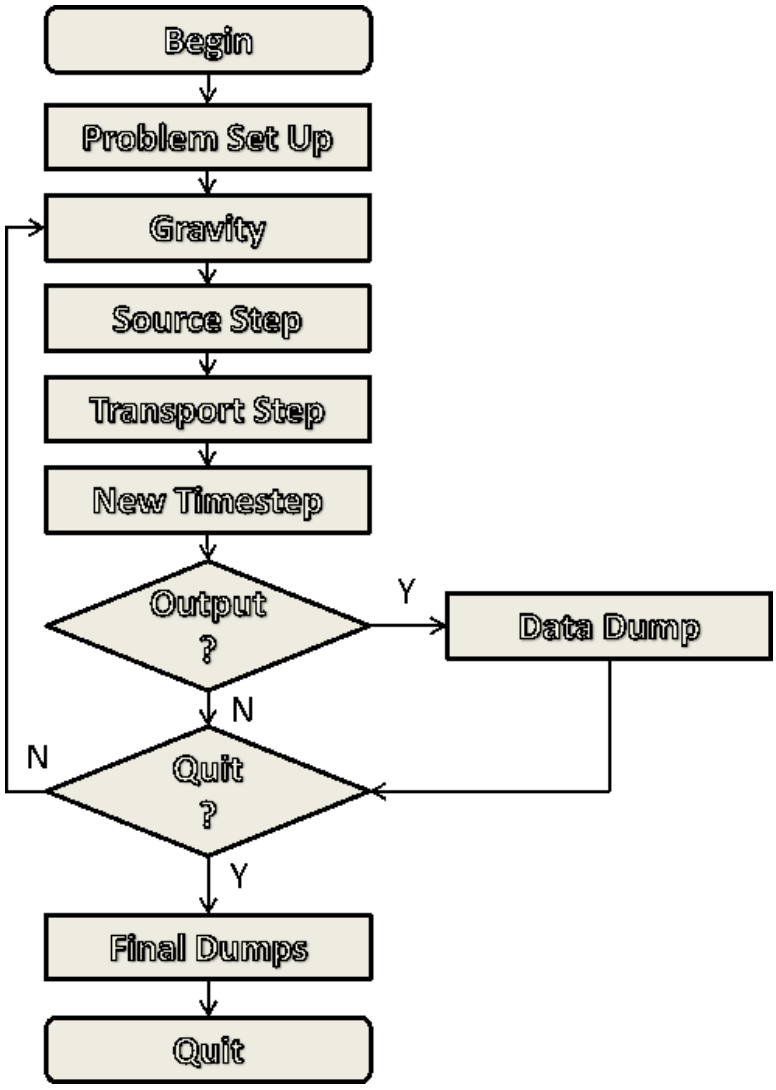

Figure 4.1: The program control for Zeus-MP/2. Modifications were made to the gravity and source steps.

with finer mesh spacing at the midplane. Similarly, since we do not require the low-density buffer region to be well resolved, the mesh spacing in the x- and y-directions is uniform within a central region and increasing logarithmically beyond that region (see Fig. 4.2).

4.4 Modification of the Gravity Solver

To solve the Poisson equation for an isolated object, the values on the boundary of the computational domain must be specified. The publicly available version of Zeus MP/2 provides a solver which calculates the monopole and quadrupole moments for each processor around the local center of mass and uses those values to calculate the potential on the boundary. This method is subject to several limitations:

- Since each processor calculates its moments around its local center of mass, the solution will be dependant on the tiling of the processors over the computational domain.
- The Poisson solver does not use higher moments. It is unlikely that the solution will be accurate.[1]
- The Poisson solver does not include the outer moments. If there is mass near the boundary, its contribution to the potential will not be accounted for.

Due to these issues, the boundary solver has been completely rewritten. To calculate the boundary potential, we use the multipole expansion of the potential equation (4.1).

[1]Clearly, there are situations where this is a reasonable approximation; however, those situations are dependent on the tiling of the processors. For this to be accurate, each processor must have a local density distribution with only a monopole and quadrupole moment about its local center of mass. This is a rather restrictive class of mass distributions.

$$\Phi(r,\theta,\phi) = 4\pi G \sum_{\ell=0}^{\infty} \sum_{m=-\ell}^{\ell} \frac{1}{2\ell+1} Y_\ell^m(\theta,\phi) \int dx' Y_\ell^{*m}(\theta',\phi') \frac{r_<^\ell}{r_>^{\ell+1}} \rho(r') \tag{4.1a}$$

$$= G \sum_{\ell=0}^{\infty} \sum_{m=-\ell}^{\ell} \frac{(l-m)!}{(l+m)!} \int dx' P_\ell^m(\theta',\phi') P_\ell^m(\theta,\phi) e^{-im\phi'} e^{im\phi} \frac{r_<^\ell}{r_>^{\ell+1}} \rho(r') \ , \tag{4.1b}$$

where $r_< = \min(r, r')$ and $r_> = \max(r, r')$. We define moments

$$Q_{\ell m}^{\text{inner,even}}(r) = \frac{(\ell-m)!}{(l+m)!} \int_{r'<r} dx' P_\ell^m(\cos\theta) \rho(x') \cos(m\phi)' r_<^\ell \tag{4.2a}$$

$$Q_{\ell m}^{\text{inner,odd}}(r) = \frac{(\ell-m)!}{(l+m)!} \int_{r'<r} dx' P_\ell^m(\cos\theta) \rho(x') \sin(m\phi)' r_<^\ell \tag{4.2b}$$

$$Q_{\ell m}^{\text{outer,even}}(r) = \frac{(\ell-m)!}{(l+m)!} \int_{r'>r} dx' P_\ell^m(\cos\theta) \rho(x') \cos(m\phi)' \frac{1}{r_<^{\ell+1}} \tag{4.2c}$$

$$Q_{\ell m}^{\text{outer,odd}}(r) = \frac{(\ell-m)!}{(l+m)!} \int_{r'>r} dx' P_\ell^m(\cos\theta) \rho(x') \sin(m\phi)' \frac{1}{r_<^{\ell+1}} \ . \tag{4.2d}$$

Then the potential can be written as

$$\begin{aligned} \Phi(r,\theta,\phi) =& G \sum_{\ell=0}^{\infty} \Bigg\{ \frac{Q_{\ell 0}^{\text{inner}}(r)}{r^{\ell+1}} + Q_{\ell 0}^{\text{outer}}(r) r^\ell \\ &+ 2 \sum_{m=1}^{\ell} \Bigg[\left(\frac{Q_{lm}^{\text{inner,even}}(r)}{r^{\ell+1}} + Q_{lm}^{\text{outer,even}}(r) r^\ell \right) \cos(m\phi) \\ &+ \left(\frac{Q_{lm}^{\text{inner,odd}}(r)}{r^{\ell+1}} + Q_{lm}^{\text{outer,odd}}(r) r^\ell \right) \sin(m\phi) \Bigg] \Bigg\} \ . \end{aligned} \tag{4.3}$$

Initially, the global center of mass is calculated. Each processor then calculates its local contribution to the global moments. Since the moments are dependant on the radial distance from the center of mass, the moments are binned according to radial distance with bin width Δr. The associated Legendre functions $P_\ell^m(x)$ are calculated using the recursion relations

$$(\ell - m + 1)P^m_{\ell+1}(x) = (2\ell + 1)xP^m_\ell(x) - (\ell + m)P^m_{\ell-1}(x) \tag{4.4a}$$

$$P^\ell_{\ell+1}(x) = x(2\ell + 1)P^\ell_\ell(x) \tag{4.4b}$$

$$P^\ell_\ell(x) = (-1)^\ell(2\ell - 1)!!(1 - x^2)^{\ell/2} \ . \tag{4.4c}$$

The moments are only calculated for values $\ell \leq \ell_{max}$. These arrays are passed to each processor. As the value of ℓ_{max} increases, the amount of data passed through interprocessor communication is increased and slows the code dramatically. Thus, the value of ℓ_{max} must be chosen to be sufficiently large to ensure convergence but small enough for computational efficiency. The local moments from each processor are combined and used to calculate the boundary values for the gravitational potential.

4.5 Faraday's Law of Induction in the Presence of Ambipolar Diffusion and Ohmic Dissipation

In this section we outline the implementation of the nonideal MHD update in the ZEUS-MP code.

4.5.1 Constrained Transport

To ensure that the magnetic field remains divergence-free (to machine accuracy), the Zeus code employs constrained transport. Instead of working with the magnetic field directly, we instead work with the flux Φ_B through the surface of each zone. Faraday's law of induction becomes

$$\frac{d\Phi_B}{dt} = -c \int_S \boldsymbol{\nabla} \times \boldsymbol{E} \cdot d\boldsymbol{S} \tag{4.5a}$$

$$= \oint_C \boldsymbol{v} \times \boldsymbol{B} \cdot d\boldsymbol{\ell} \tag{4.5b}$$

$$\equiv \oint_C \boldsymbol{\varepsilon} \cdot d\boldsymbol{\ell} \ , \tag{4.5c}$$

where C is the closed boundary of the surface S. The quantity $\boldsymbol{\varepsilon} = \boldsymbol{v} \times \boldsymbol{B}$ is the electromotive force (EMF) acting along the curve C. As Evans and Hawley (1988) pointed out, this will ensure that the magnetic field remains divergence-free even when it is differenced, provided that the same EMFs are used in all updates to the magnetic field. In its differenced form, the update becomes:

$$\begin{aligned}\frac{\Phi^{n+1}_{1;i,j,k} - \Phi^{n}_{1;i,j,k}}{\Delta t} =& \varepsilon_{2;i,j,k}\Delta x_{2;i,j,k} + \varepsilon_{3;i,j+1,k}\Delta x_{3;i,j+1,k} - \varepsilon_{2;i,j,k+1}\Delta x_{2;i,j,k+1} \\ & - \varepsilon_{3;i,j,k}\Delta x_{3;i,j,k}\end{aligned} \tag{4.6a}$$

$$\begin{aligned}\frac{\Phi^{n+1}_{2;i,j,k} - \Phi^{n}_{2;i,j,k}}{\Delta t} =& \varepsilon_{1;i,j,k+1}\Delta x_{1;i,j,k+1} + \varepsilon_{3;i,j,k}\Delta x_{3;i,j,k} - \varepsilon_{1;i,j,k}\Delta x_{1;i,j,k} \\ & - \varepsilon_{3;i+1,j,k}\Delta x_{3;i+1,j,k}\end{aligned} \tag{4.6b}$$

$$\begin{aligned}\frac{\Phi^{n+1}_{3;i,j,k} - \Phi^{n}_{3;i,j,k}}{\Delta t} =& \varepsilon_{1;i,j,k}\Delta x_{1;i,j,k} + \varepsilon_{2;i+1,j,k}\Delta x_{1;i+1,j,k} - \varepsilon_{1;i,j+1,k}\Delta x_{1;i,j+1,k} \\ & - \varepsilon_{2;i,j,k}\Delta x_{2;i,j,k} \ .\end{aligned} \tag{4.6c}$$

The indices i, j, and k correspond to zone indices and Φ_1, Φ_2, and Φ_3 are the fluxes in each of the three directions. If the initial fluxes through the zone faces sum up to zero, the final fluxes will also do so. Although this method does ensure that the magnetic field remains divergence free, it does not ensure the accuracy or the stability of the solution.

4.5.2 Method of Characteristics

The underlying mechanism for determining the EMFs must ensure that the MHD waves are propagated accurately. The longitudinal-compressive modes – the fast and slow magnetosonic modes – can be handled by the source-step finite-differencing algorithms; however, these methods will not accurately propagate the transverse-noncompressive Alfvén waves. By employing the method of characteristics, improved accuracy in the update of the magnetic field can be achieved.

Although the routine for advecting the magnetic field has not been modified from its publicly available form, the method used will be important in understanding the stability criterion for the nonideal source update outlined later (§4.5.3).

Under ideal MHD, the EMFs can be expressed as

$$\varepsilon_{1;i,j,k} = v^*_{2;i,j,k} B^*_{3;i,j,k} - v^*_{3;i,j,k} B^*_{2;i,j,k} \tag{4.7a}$$

$$\varepsilon_{2;i,j,k} = v^*_{3;i,j,k} B^*_{1;i,j,k} - v^*_{1;i,j,k} B^*_{3;i,j,k} \tag{4.7b}$$

$$\varepsilon_{3;i,j,k} = v^*_{1;i,j,k} B^*_{2;i,j,k} - v^*_{2;i,j,k} B^*_{1;i,j,k} \ . \tag{4.7c}$$

The starred quantities represent the time-centered[2] values of the velocity and magnetic field located at the zone-edges, the same location as the EMFs. To calculate the time-centered values, we employ the method of characteristics.

To illustrate the method of characteristics in the context of Alfvén waves we consider the simplified case of a uniform-density distribution with a magnetic and velocity field which only varies in the x direction.

$$\boldsymbol{B} = B_x \hat{\boldsymbol{e}}_x + B(x) \hat{\boldsymbol{e}}_y \tag{4.8a}$$

[2] *Time centered* indicates the value of a quantity at an intermediate time. For example, if the initial time is t and the time after the update is $t + \Delta t$ then the time-centered value is located at $t + \Delta t/2$. Schematically, if the initial value for a quantity is q^n and the updated value is q^{n+1}, then the time-centered value is $q^{n+1/2}$.

$$\boldsymbol{v} = v_x \hat{\boldsymbol{e}}_x + v(x)\hat{\boldsymbol{e}}_y \ . \tag{4.8b}$$

In this simplified case, the advection equations become:

$$\frac{\partial B}{\partial t} = B_x \frac{\partial v}{\partial x} - v_x \frac{\partial B}{\partial x} \tag{4.9a}$$

$$\frac{\partial v}{\partial t} = \frac{B_x}{4\pi\rho} \frac{\partial B}{\partial x} - v_x \frac{\partial B}{\partial x} \ . \tag{4.9b}$$

By multiplying Equation 4.9a by $(4\pi\rho)^{-1/2}$ and then adding and subtracting this equation with Equation 4.9b yields the two characteristic equations

$$\frac{Dv}{Dt} \pm \frac{1}{\sqrt{4\pi\rho}} \frac{DB}{Dt} = 0 \ , \tag{4.10}$$

where the comoving derivative D/Dt is given by

$$\frac{D}{Dt} \equiv \frac{\partial}{\partial t} + (v_x \mp v_A) \frac{\partial}{\partial x} \ . \tag{4.11}$$

The Alfvén speed of the background state is given by $v_A = B_x/\sqrt{4\pi\rho}$. Equation 4.10 relates the velocity and magnetic field along forward- and backward-facing characteristics $C^{\pm}$. If the edge is located at x^*, the two characteristics that intersect at x^* can be used to trace back to find the *footprints* $x^{\pm}$ – the origins of the two characteristics at time t. Equation 4.10 can then be used to relate the value of the magnetic field and velocity at $x^{\pm}$ ($B^{\pm}$ and $v^{\pm}$, respectively) to the values at x^*:

$$\frac{v^* - v\pm}{\Delta t/2} \pm \frac{1}{\sqrt{4\pi\rho^{\pm}}} \frac{B^* - B^{\pm}}{\Delta t/2} = 0 \ . \tag{4.12}$$

For $B^{\pm}$ and $v^{\pm}$, the upwind values are determined by the characteristic speeds $v_x \pm v_A$. For simplicity, the value of $\rho^{\pm}$ is set to the average value for the zone containing $x^{\pm}$. Once these values have been determined, the two equations 4.12 can be solved directly and the values of v^* and B^* determined. These can then be substituted in Equation 4.7 in order to

solve for the EMFs.

Although the multidimensional case is more complicated (a discussion can be found in Appendix C1 of Hayes et al. (2006)), the one dimensional case is sufficient for the purpose of explaining the method.

4.5.3 The Ambipolar Diffusion and Ohmic Dissipation Update

The advection of the magnetic field is done using the constrainted transport (CT) method. The nonideal terms in Faraday's law,

$$\frac{\partial \boldsymbol{B}}{\partial t} - \boldsymbol{\nabla} \times (\boldsymbol{v} \times \boldsymbol{B}) = -\boldsymbol{\nabla} \times \left(\eta_{\parallel} \boldsymbol{j}_{\parallel} + \eta_{\perp} \boldsymbol{j}_{\perp} + \eta_H \boldsymbol{e}_B \times \boldsymbol{j}_{\perp} \right) , \tag{4.13}$$

are included as a source contribution where $\boldsymbol{j} = (c/4\pi)\boldsymbol{\nabla} \times \boldsymbol{B}$. While each componet of the magnetic field is located on a face of the zone (see Fig. 4.4), the EMFs are located on the edges of the zone (see Fig. 4.5). Central differencing of the relation $\boldsymbol{j} = (c/4\pi)\boldsymbol{\nabla} \times \boldsymbol{B}$ yields a single component on each of the edges:

$$(\nabla \times B)_1 (i,j,k) = \frac{B_3(i,j,k) - B_3(i,j-1,k)}{\mathrm{dvl}_{2b}(j)} - \frac{B_2(i,j,k) - B_2(i,j,k-1)}{\mathrm{dvl}_{3b}(k)} \tag{4.14a}$$

$$(\nabla \times B)_2 (i,j,k) = \frac{B_1(i,j,k) - B_1(i,j,k-1)}{\mathrm{dvl}_{3b}(k)} - \frac{B_3(i,j,k) - B_3(i-1,j,k)}{\mathrm{dvl}_{1b}(i)} \tag{4.14b}$$

$$(\nabla \times B)_3 (i,j,k) = \frac{B_2(i,j,k) - B_2(i-1,j,k)}{\mathrm{dvl}_{1b}(i)} - \frac{B_1(i,j,k) - B_1(i,j-1,k)}{\mathrm{dvl}_{2b}(j)} \tag{4.14c}$$

where $(\nabla \times B)_1$, $(\nabla \times B)_2$, and $(\nabla \times B)_3$ are the parallel components of the curl on the 1-, 2-, and 3-edges, respectively. To find EMFs, all three components of the current are needed to be calculated on each edge. The remaining components of the curl perpendicular to the edge are found through interpolation:

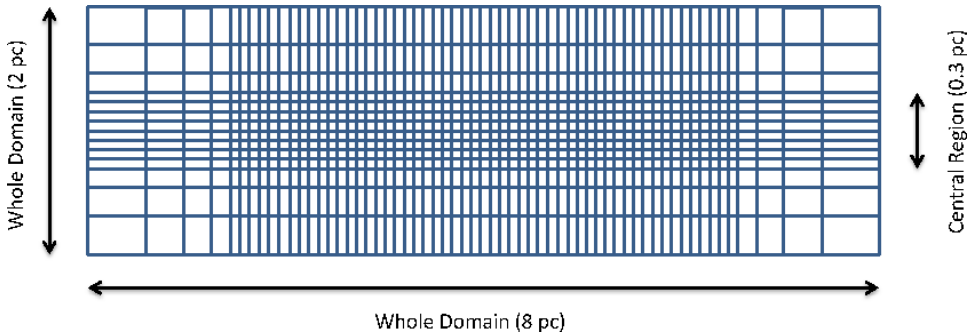

Figure 4.2: The nonuniform grid. The short axis corresponds to the +z direction (the direction of the initial magnetic field). The other direction is the $+x$ or $+y$ directions. The grid is finer in the central region where the cores will ultimately form and logarithmically increasing in spacing away from the center. The number of grid zones depicted in the figure does not correspond to the actual number of zones.

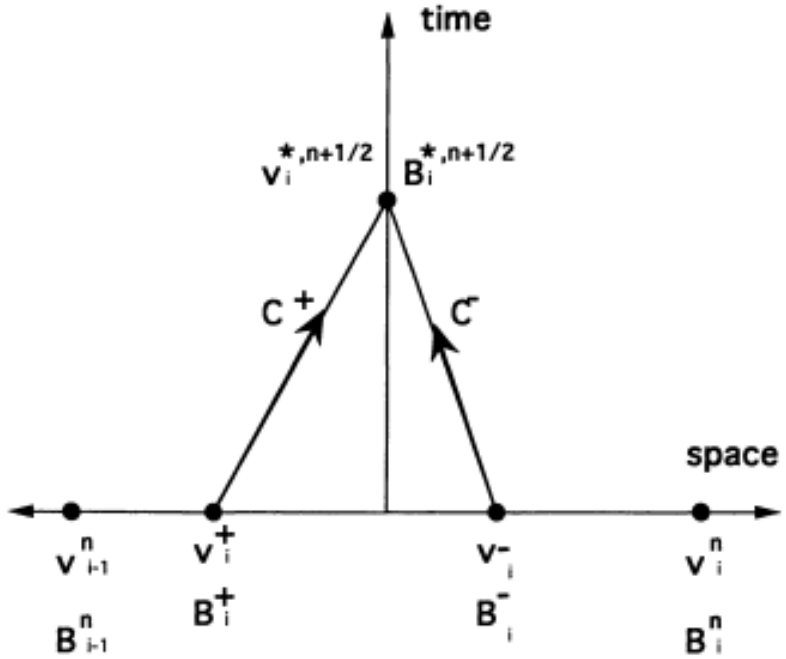

Figure 4.3: Space-time diagram illustrating how the characteristics $C^{\pm}$ which intersect at $t^{n+1/2}$ can be traced back to their footprints $x^{\pm}$ at time t^n. Source: Stone and Norman (1992).

$$\left(\boldsymbol{j}^3\right)_1(i,j,k) = \frac{1}{4}\left(\boldsymbol{j}_1(i,j,k) + \boldsymbol{j}_1(i,j,k+1) + \boldsymbol{j}_1(i-1,j,k) + \boldsymbol{j}_1(i-1,j,k+1)\right) \ , \tag{4.15}$$

where $\boldsymbol{j}^i_j$ is the j-component of the current living on the i^{th}-edge. The parallel and perpendicular components can then be calculated using the interpolated magnetic field

$$B^3_1 = \frac{1}{2}\left[B_1(i,j,k) + B_1(i,j-1,k)\right] \ . \tag{4.16}$$

When evaluating the EMF, only components of $\boldsymbol{j}_\parallel$ and $\boldsymbol{j}_\perp$ parallel to the edge contribute, so we drop terms perpendicular to the edge from this point on.

$$\boldsymbol{j}^3_\parallel = \frac{B^3_1}{\sqrt{\boldsymbol{B}^3 \cdot \boldsymbol{B}^3}} \ , \tag{4.17}$$

where $\hat{\boldsymbol{j}}^3_\parallel$ is the projection of $\boldsymbol{j}_\parallel$ onto the 3-edge. The EMFs can then be calculated

$$\varepsilon_1(i,j,k) = \hat{\eta}^1_\parallel \hat{\boldsymbol{j}}^1_\parallel(i,j,k) + \hat{\eta}^1_\perp \hat{\boldsymbol{j}}^1_\perp(i,j,k) \tag{4.18}$$

$$\varepsilon_2(i,j,k) = \hat{\eta}^2_\parallel \hat{\boldsymbol{j}}^2_\parallel(i,j,k) + \hat{\eta}^2_\perp \hat{\boldsymbol{j}}^2_\perp(i,j,k) \tag{4.19}$$

$$\varepsilon_3(i,j,k) = \hat{\eta}^3_\parallel \hat{\boldsymbol{j}}^3_\parallel(i,j,k) + \hat{\eta}^3_\perp \hat{\boldsymbol{j}}^3_\perp(i,j,k) \ , \tag{4.20}$$

where ε_1, ε_2, ε_3 are the EMFs along the 1-, 2-, and 3-edges, respectively. Once the EMFs are known, the updated fluxes can be calculated using equations 4.6.

4.5.4 The Timestep

The inclusion of ambipolar diffusion and ohmic dissipation in the code drastically shortens the timestep, with the limiting timestep being

$$\tau_{\mathrm{OD,AD}} = \frac{2\Delta x^2}{\max\left(\eta_{\parallel}, \eta_{\perp}, \eta_{\mathrm{H}}\right)} \ . \tag{4.21}$$

This is the expected timestep for a diffusive process; however, this timestep also ensures that the characteristics used in advecting the magnetic field (see §4.5.2) do not change appreciably over the course of the timestep (Mac Low et al. 1995).

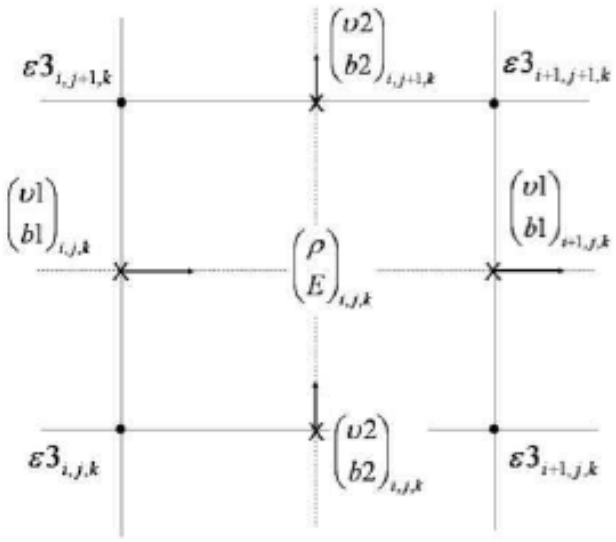

Figure 4.4: The grid.

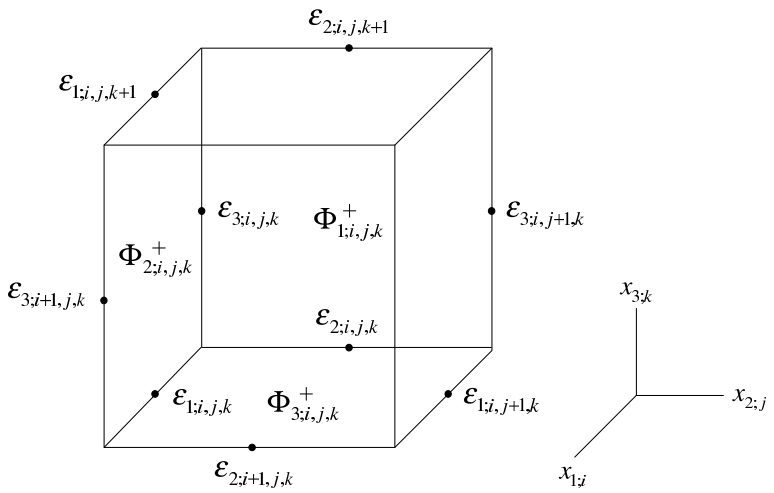

Figure 4.5: The EMF grid. Due to the method for differencing used in calculating the EMFs, the resulting EMFs are located on the edges of zones while the fluxes are located on the centers of the faces.

Chapter 5

Results

In this chapter we discuss the results of the simulations done in our parameter study. This chapter is divided into three sections. In §5.1 we survey how a typical cloud evolves from its initial equilibrium state to its state at the end of the run. In §5.2 we discuss bulk properties of the model cloud, including the distribution of column densities and mass-to-flux ratios. In §5.3, the properties of individual cores within the model clouds are described.

Within the computational domain, we identify two separate structures: the cloud and the cores. The cloud consists of any gas with a volume density exceeding a threshold $n_{\rm cloud}$ which, for our purposes, is taken to be $n_{\rm cloud} = 500\ {\rm cm}^{-3}$. The reason for defining the cloud to be above a certain threshold instead of simply chosing the cloud to be all the gas in the computational domain is to eliminate the effect of the buffer regions when considering bulk properties of clouds. As discussed in §3.1, these buffer regions consist of low-density gas whose purpose is to create a buffer between the computational boundary and the interior, high-density region of interest. Including these buffer regions would skew column densities, mean thermal wavelengths, and other quantities of interest. The value of $500\ {\rm cm}^{-3}$ was chosen because it is low enough that it could be reasonable definition for a cloud boundary but large enough that it would exclude much of the gas in the buffer regions.

The *cores* consist of the high-density fragments which will ultimately become gravitationally unstable and collapse. For our purposes, we define a core to be any collection of gas with a volume density greater than $n_{\rm core}$, where $n_{\rm core} = 2 \times 10^4\ {\rm cm}^{-3}$. This choice

corresponds to the approximate volume density above which astronomers are able to observe NH_3, a common tracer of prestellar fragments. This is not a unique choice, but is a useful operational definition of a *core*.

5.1 Evolution of a Typical Cloud

The model cloud (L24), initially supported by the turbulent pressure and magnetic forces (see Fig. 5.1 (a)), begins to contract along the magnetic field lines as the initial velocity perturbation dissipates due to shocks and ambipolar diffusion and the turbulent support is reduced (see Figs. 5.1 (b) and (c)). As the contraction progresses, the volume of the cloud (Fig. 5.3 (a)) decreases relative to the initial cloud while the overall mass of the cloud with a density greater than $500\ \mathrm{cm}^{-3}$ increases (Fig. 5.3 (b)). As can be seen in Fig. 5.3 (c), most of the kinetic energy has dissipated within the first million years. The cloud contracts further and the kinetic energy begins to increase again due to release of gravitational potential energy. Even though the cloud has settled into a flattened state, it continues to evolve. Density enhancements – *fragments* – begin to grow as gravity draws the neutral gas through the magnetic field. Once a fragment becomes supercritical, the peak density begins to increase rapidly (Fig. 5.4 (a)).

Density. As the cloud initially contracts along the magnetic field lines, the density increases and the cloud becomes increasingly flattened. In this flattened state, the density slowly increases as gravity draws the neutrals through the magnetic field due to ambipolar diffusion. Once a fragment becomes supercritical, the density increases much more rapidly (see Fig. 5.4 (a)).

Kinetic Energy. Initially, the kinetic energy rapidly decreases (see 5.3 (c)) due to both shocks (when the initial velocity perturbation is sufficiently high) and ambipolar diffusion. As the cloud flattens along the field lines, gravitational potential energy is converted into kinetic energy resulting in an increase in the kinetic energy (see Fig. 5.3 (c) between

$t = 1.5$ Myr and $t = 2.0$ Myr). As the cloud settles into its flattened state, the kinetic energy begins to decrease again as the wave energy is disspated by ambipolar diffusion.

Magnetic Field. In the initial state, the magnetic field lines are almost straight and parallel. Once the velocity perturbation is introduced, the field lines bend and become more disordered, with the extent of the disorder depending on the magnitude of the initial perturbation. As shocks and ambipolar diffusion dissipate the kinetic energy, the field lines begin to straighten out and remain relatively straight until fragments approach the critical state for collapse. Collapsing fragments evolve on timescales much smaller than the ambipolar diffusion time[1] which results in the field lines being dragged along with the infalling gas. This results in the characteristic hourglass morphology (e.g. Fig. 1.1(a)).

5.2 Cloud Properties

5.2.1 Column Density Distribution

Since observations of extinction of starlight in molecular clouds – used as a proxy for column density – show that they are distributed lognormally, it is important to check where the model clouds display this property. The angle θ is measured relative to the direction of the initial magnetic field (see Fig. 5.7).

For angles $\theta = 0°$ and $\theta = 30°$, the column density distribution fits well to a lognormal; however, for lines-of-sight which look through the plane of the disk ($\theta = 60°$ and $\theta = 90°$), a low-density tail develops which makes the fit less accurate. By only including high-column densities, thus excluding the low column density tail, a good fit can be found again (see Fig. 5.6). The low-mass tail is due to lines-of-sight which go through low-density gas above and below the midplane, not rays which cross the midplane of the cloud.

[1] At later stages in the collapse, ambipolar diffusion will *reawaken*; however, this is beyond the scope of this thesis.

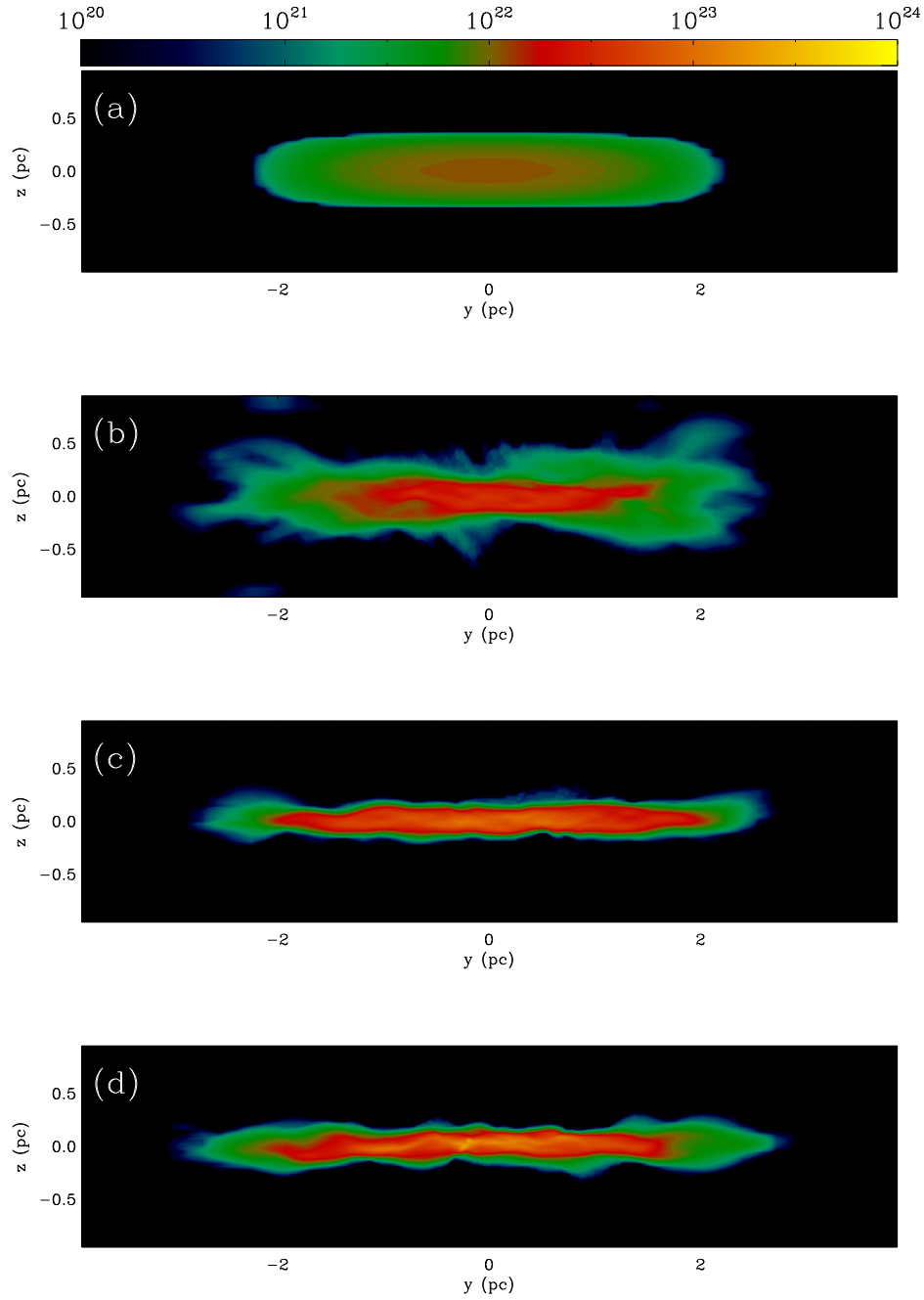

Figure 5.1: Evolution of a typical cloud. The plots show the column density as viewed perpendicularly from the initial magnetic field. The times are (a) $t = 0.0\,\mathrm{yr}$, (b) $t = 1.58\,\mathrm{Myr}$, (c) $t = 3.20\,\mathrm{Myr}$, and (d) $t = 4.59\,\mathrm{Myr}$.

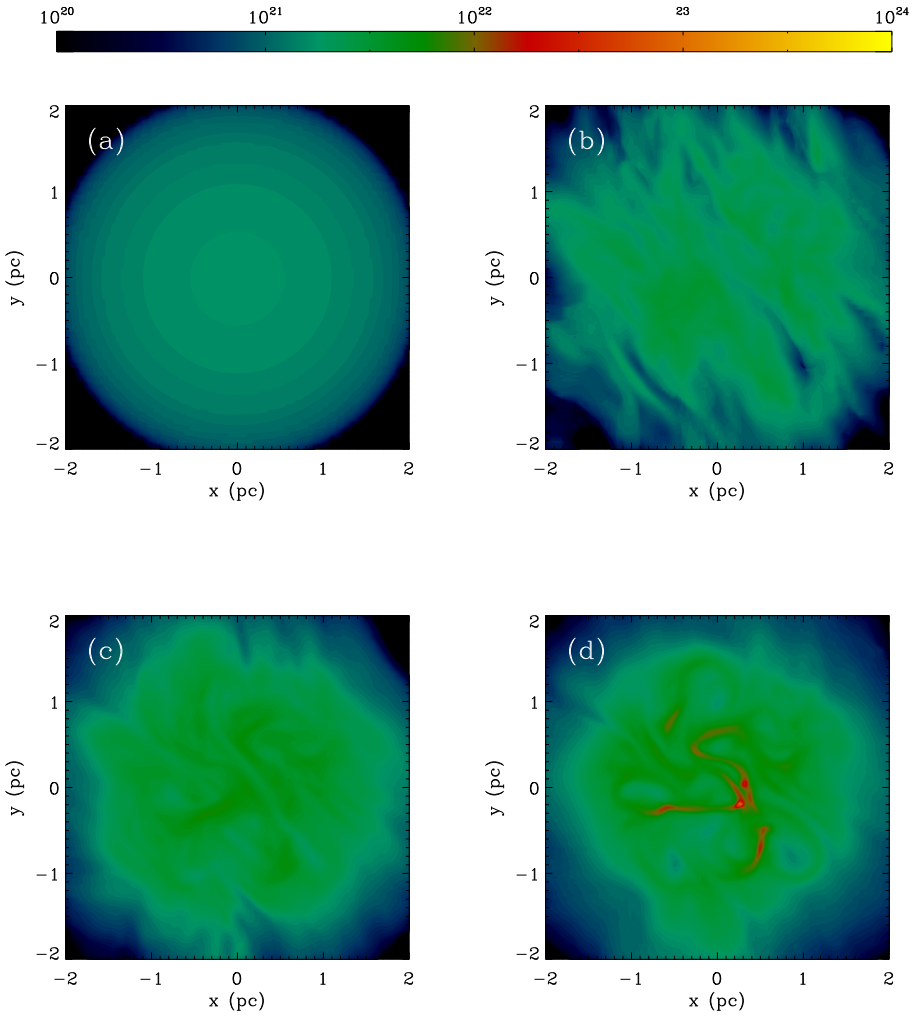

Figure 5.2: Evolution of a typical cloud. The plots show the column density as viewed along the initial magnetic field at times (a) $t = 0.0\,\mathrm{yr}$, (b) $t = 1.58\,\mathrm{Myr}$, (c) $t = 3.20\,\mathrm{Myr}$, and (d) $t = 4.59\,\mathrm{Myr}$.

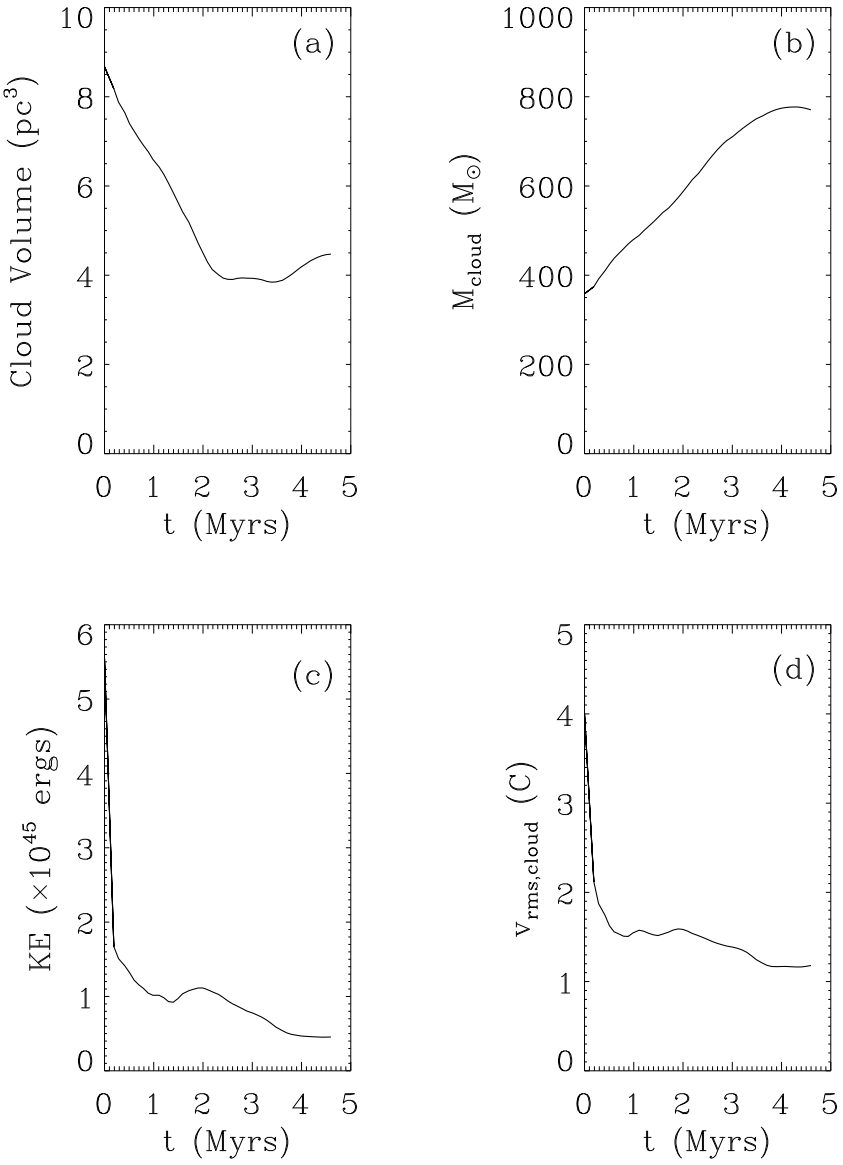

Figure 5.3: Time evolution of quantities within a typical cloud. The cloud is defined as all gas above $500\,\mathrm{cm}^{-3}$. (a) Volume of the cloud. (b) The mass of the cloud. (c) Kinetic energy within the computational domain. Most of the energy is quickly dissipated due to ambipolar diffusion and shocks. The slight increase in kinetic energy around $2\,\mathrm{Myrs}$ is due to gravitational energy being released as the cloud contracts. (d) The RMS velocity of the gas within the cloud.

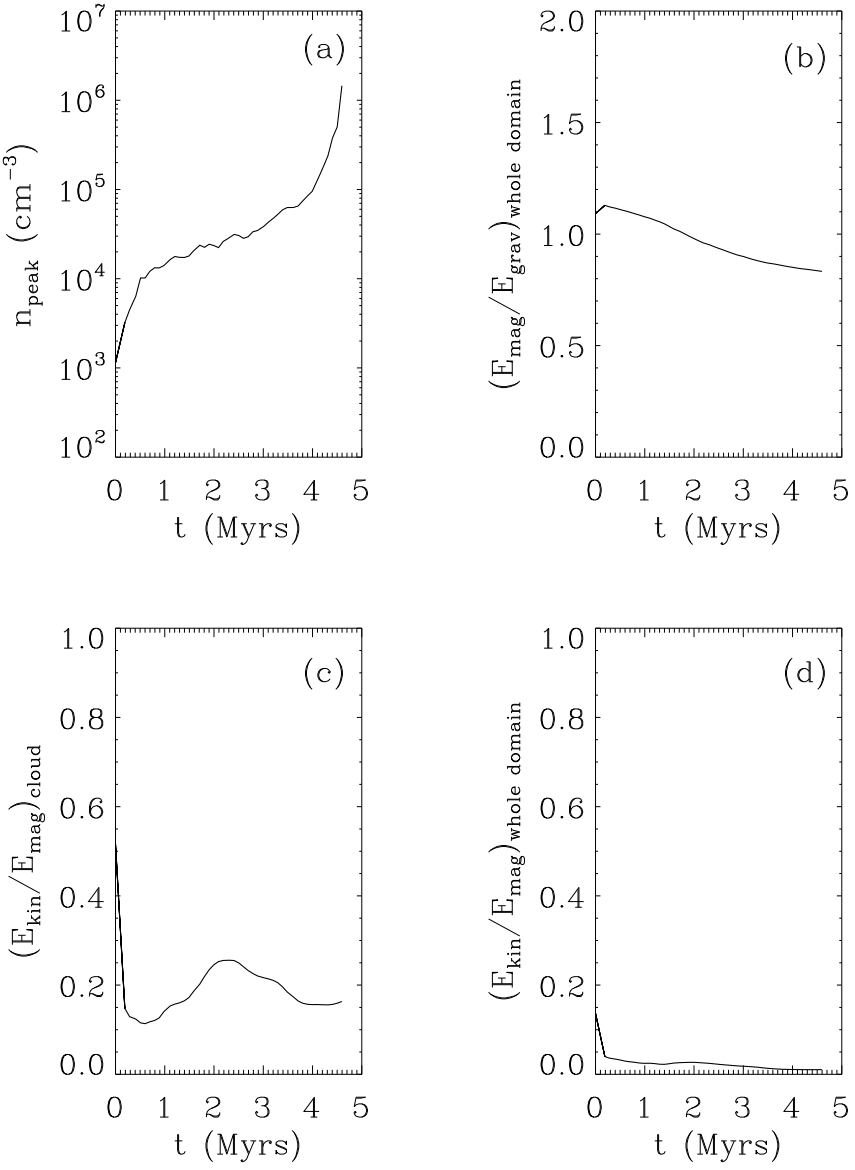

Figure 5.4: Time evolution of quantities within a typical cloud. (a) Peak density. (b) Ratio of magnetic and gravitational energies. (c) Ratio of the kinetic energy within the cloud and the magnetic energy of the cloud. (d) Ratio of the kinetic and magnetic energies for the entire computational domain.

This trend is seen in all the runs, including runs with subsonic initial perturbations. This contradicts the notion that lognormal linewidths are a sign of supersonic turbulence within the cloud. Tassis et al. (2010) have also shown that a Bonnor-Ebert-like density distribution,

$$\rho(r) = \begin{cases} \rho_c a^2 / \left(a^2 + r^2\right) & r < R \\ 0 & r \geq R \,, \end{cases} \tag{5.1}$$

also results in a lognormal column density distribution with the parameter a determining the relative prominance of the high column density tail. These results indicate that lognormal column density distributions could be quite common, and it shouldn't be used as an indicator for supersonic turbulence (Tassis et al. 2010).

5.2.2 Projection Effects and the Mass-to-Flux Ratio

As discussed in §1.2.1, the stability of a molecular cloud depends mainly on its mass-to-flux ratio. This quantity is the ratio of the mass in a flux tube and the actual flux through the flux tube. Since flux tubes are not necessarily straight, it is very difficult to observe the relevant mass-to-flux ratio. Additionally, since astronomers only observe the column density and magnetic field along a line-of-sight, projection effects become important. The observed mass-to-flux ratio $\mu_{\rm obs}$, defined by the ratio of the observed column density and the observed line-of-sight magnetic field,

$$\mu_{\rm obs} = \frac{N_{\rm los}}{\langle B_{\rm los} \rangle} \Bigg/ \left(\frac{M}{\Phi_{\rm B}}\right)_{\rm crit} \,, \tag{5.2}$$

$$\langle B_{\rm los} \rangle = \int \Theta(\rho - \rho_{\rm min}) \boldsymbol{B} \cdot d\boldsymbol{s} \Bigg/ \int \Theta(\rho - \rho_{\rm cloud}) \, ds \,, \tag{5.3}$$

has implications for the stability of a molecular cloud or core only if it can be related back to the actual mass-to-flux ratio μ. The quantity $\Theta(x)$ is the Heaviside function

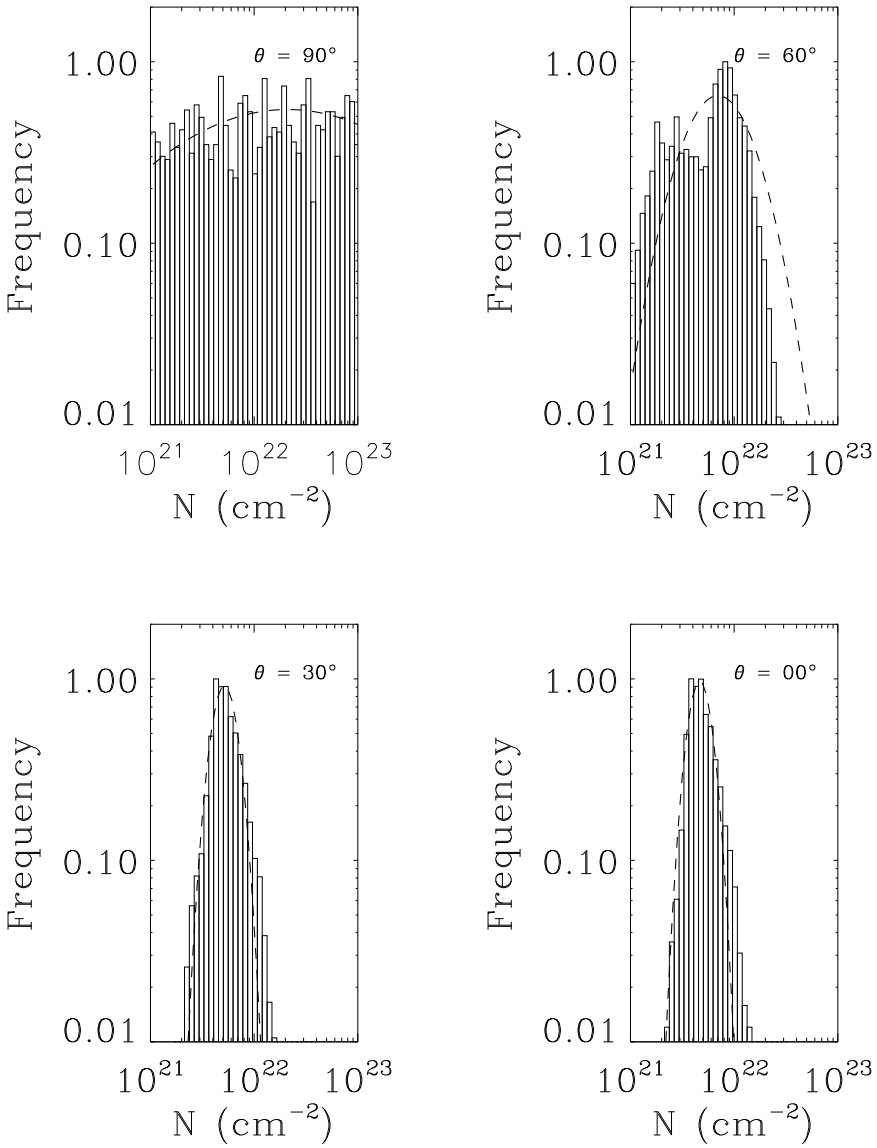

Figure 5.5: Column density distribution for a typical run (H3) as observed from different viewing angles. The dashed line is a fit of the data to a lognormal distribution.

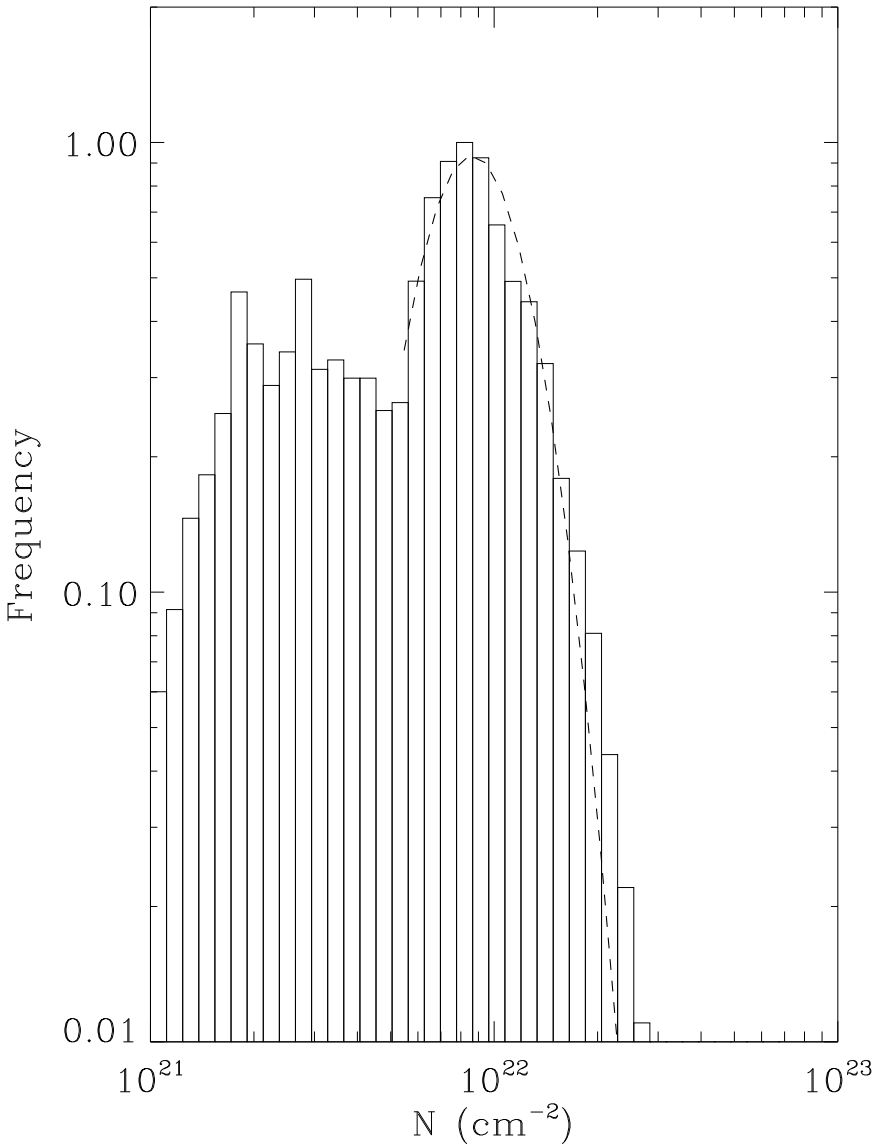

Figure 5.6: Column density distribution for run H3 at viewing angle $\theta = 60°$. Unlike the previous plot, the dashed line is only a fit to column densities $\sigma > 4 \times 10^{22}\,\mathrm{cm}^{-2}$.

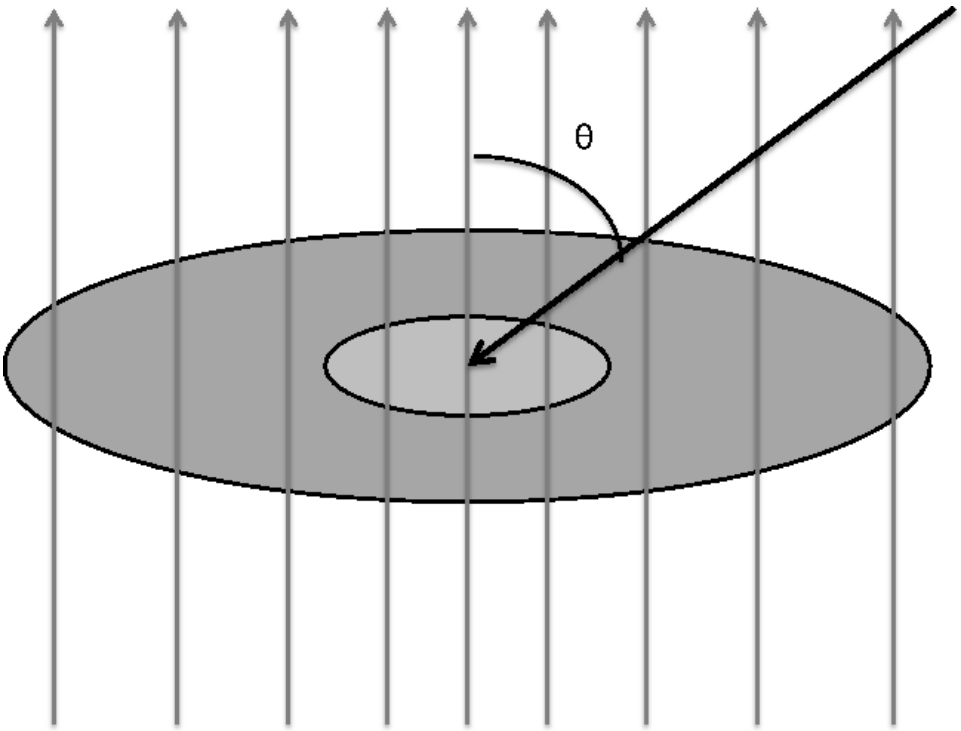

Figure 5.7: The line-of-sight angles are measured with respect to the +z axis, the direction of the initial magnetic field. The clouds formed are flattened along the magnetic field lines, resulting in oblate clouds.

$$\Theta(x) = \begin{cases} 0 & x < 0 \\ 1 & x \geq 0 \, , \end{cases} \tag{5.4}$$

To understand the effect of projection, we sample, as in the case of the column densities, the mass-to-flux ratio along multiple lines of sight, all at the same inclination angle θ with respect to the z axis (see Figure 5.8). The projection effects associated with the mass-to-flux ratio can be decomposed into two effects. First, at a given inclination θ relative to the magnetic field the line-of-sight field is given by $B_{\rm los} = B\cos\theta$. Assuming all lines of sight are equally likely, the expected line-of-sight magnetic field becomes $\langle B_{\rm los}\rangle = \frac{1}{2}B$; thus, on average, the magnetic field strength will be underestimated by a factor of 2. Second, the relevant column density used in calculating the mass-to-flux ratio is the column density along the direction of the magnetic field. If cores are flattened disks with the magnetic field aligned with the minor axis, the line-of-sight column density $N_{\rm los}$ can be related to the column densty along the flux tube by $N_{\rm los} = N_{\rm flux}\left(\cos\theta\right)^{-1}$. This results in the observed mass-to-flux ratio $\left(M/\Phi_{\rm B}\right)_{\rm obs}$ being related to the actual mass-to-flux ratio $\left(M/\Phi_{\rm B}\right)_{\rm actual}$ by $\left(M/\Phi_{\rm B}\right)_{\rm actual} = \left(M/\Phi\right)_{\rm obs}\langle\cos^2\theta\rangle = \left(M/\Phi_{\rm B}\right)_{\rm obs}/3$. Thus, we expect the relevant mass-to-flux ratios to be overestimated on average by a factor of 3.

Figure 5.8 shows the effects of projection for model H3, a typical run. In the "final" state, the magnetic field lines are predominatly aligned with the $+\boldsymbol{z}$ axis, the same direction as the initial magnetic field. Thus, observations of the mass-to-flux ratio along the initial magnetic field direction ($\theta = 0^\circ$) should provide a good indicator of the actual mass-to-flux ratio. In this case, the largest observed μ_0 is less than 2; this agrees with axisymmetric simulations of magnetically supported cores which find that the mass-to-flux ratio asymptotes to 2 as a typical core collapses.

As the observing angle changes, the spread in observed mass-to-flux ratios increases, with the extreme case being viewing the flattened cloud edge-on ($\theta = 90^\circ$). In this case, the observed column densities are much higher (see discussion above) and the observed

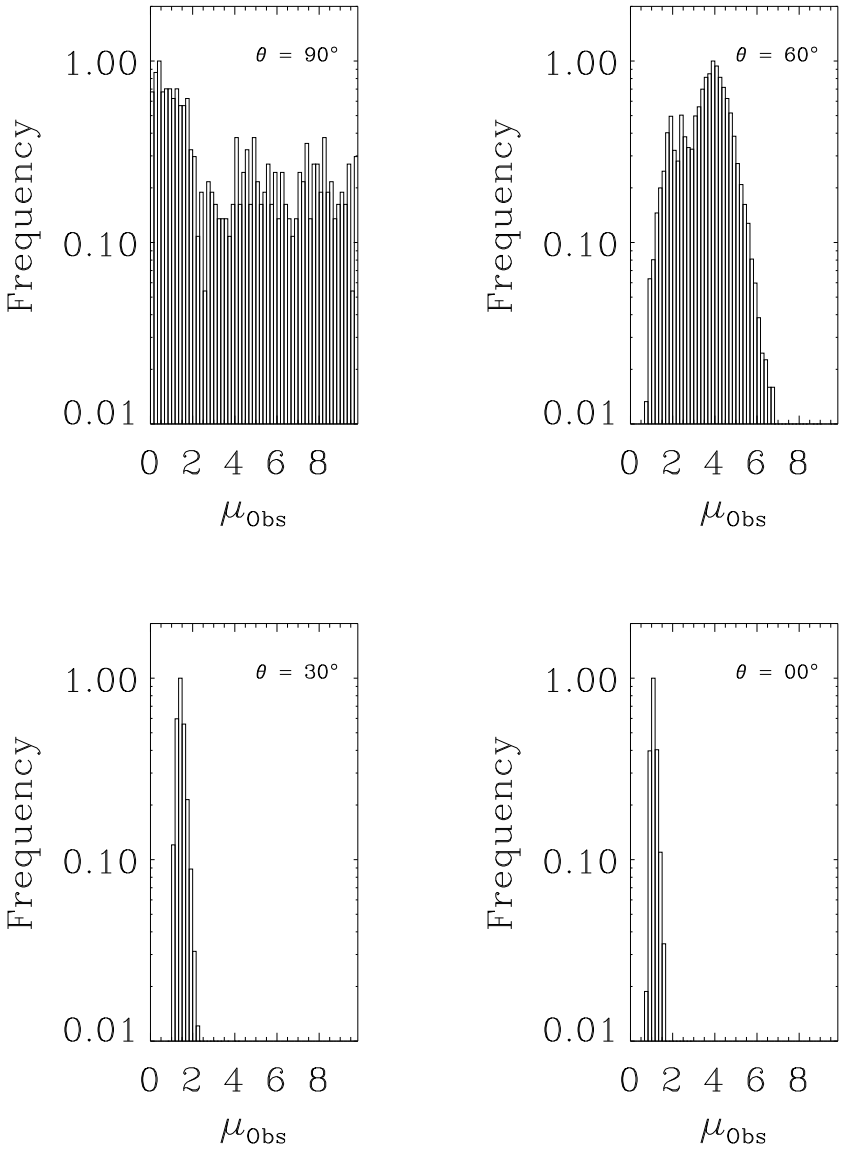

Figure 5.8: The distribution of mass-to-flux ratios for four different viewing angles for run H3.

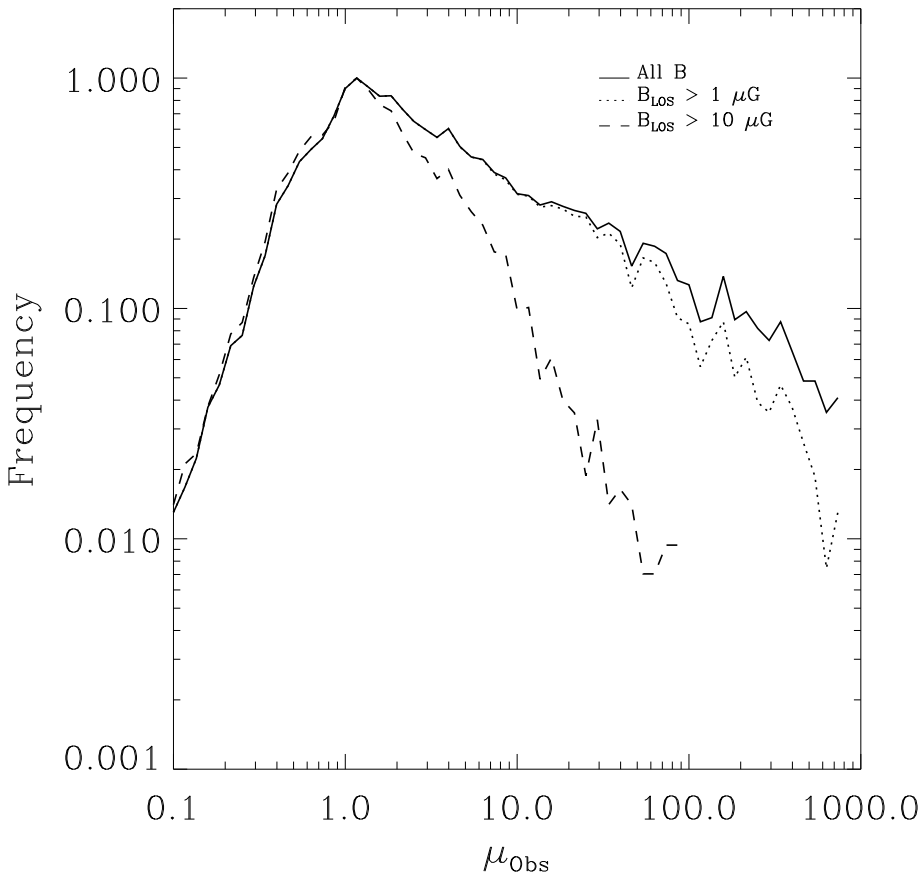

Figure 5.9: The distribution of mass-to-flux ratios for random viewing angles for run H3. The solid line shows the distribution from all the lines of sight. The dot-dash line shows the distribution for all lines of sight for which $B_{\rm los} > 1\mu$G. The dashed line refers to all lines of sight for which $B_{\rm los} > 10\mu$G.

magnetc field is due to fluctuations within the cloud, not the true mean field of the cloud.

Since the orientation of the cloud and the mean magnetic field is unknown, we instead sample random lines of sight and look at the distribution. Figure 5.9 shows the distribution of mass-to-flux ratios for three different cases. Despite the fact that the cloud is subcritical, the observed mass-to-flux ratio *appears* to be supercritical. The extremes in mass-to-flux ratio, however, are due to the very weak magnetic field or the very low column density part of a cloud. In Figure 5.9, if we only include lines of sight where the average $B_{\rm los}$ is greater than $1\,\mu$G (dotted line) or $10\,\mu$G (dashed line), the large-μ tail begins to disappear. Since observations of interstellar magnetic fields are limited to strong fields, the exclusion of small observed fields makes sense .

Even though in this run (H3) the initial mass-to-flux ratio is 0.9 times critical, there are lines of sight for which the mass-to-flux ratio is observed to be much more subcritical. This primarily is due to lines of sight with low column density, which are unrepresentative of the mean properties of the model cloud and far from values usually probed by observations.

For each cloud, we generate 30000 random lines-of-sight and calculate the mean observed mass-to-flux-ratio for three cases. The first case includes all lines-of-sight. The second case only includes lines-of-sight which have $|B_{\rm los}| > 1\,\mu$G. The final case only includes lines-of-sight with $|B_{\rm los}| > 1\,\mu$G in the average. The motivation for this is to see the effect of excluding the small values of the line-of-sight magnetic field since those are the lines-of-sight which result in the large values of $\mu_{\rm obs}$.

The average values for each model cloud are then used to relate the observed mass-to-flux ratios to the initial mass-to-flux ratio:

$$\mu_{\rm obs} = C_1 \mu_0 + C_2\,. \tag{5.5}$$

For the simple case of a infinite flattened disk with perfectly straight magnetic field lines, the values of the fit should be $C_1 = 3$ and $C_2 = 0$. For the model clouds, the results

are shown in Figure 5.10. When excluding the small values of the line-of-sight magnetic field, the fit improves greatly; however, the parameters of the fit change depending on the threshold chosen (see Table 5.1) making it difficult to take advantage of this improvement.

When including all lines-of-sight, there is a large scatter in the data. The best fit is

$$\mu_{\rm obs} = (6.78 \pm 1.83)\,\mu_0 + (-1.60 \pm 1.41)\ . \tag{5.6}$$

The fact that C_2 is non-zero is likely due to the MHD waves within the cloud; however, we have not investigated this possibility fully.

5.2.3 Filamentary Sturcture Within Molecular Clouds

Recent observations (Men'shchikov et al. 2010; André et al. 2010) have seen high-density filaments in star-forming regions, leading to proposals that cores form in gaseous filaments within molecular clouds. Figure 5.11 shows the column-density distribution from model cloud H2 looking along the +z-axis. Filamentary structures can be seen in the column densities; however, when looking at the maximum volume densities along the same lines of sight (Fig. 5.12), the filamentary structures are less apparent.

This should be contrasted with the result of run H1, a run with the same initial values for $v_{\rm turb}$, $v_{\rm sol}$, and μ_0 (see Fig. 5.13)[2]. Run H1 uses an ionization parameter of $K_{\rm CR} = 1 \times 10^{-3}\,{\rm cm}^{-3}$. The smaller ionization results in a larger Alfvén wavelength $\lambda_{\rm A}$ (see Eqn. 1.13) which reduces the amount of small scale structure within the cloud.

5.2.4 Decay of the Velocity Perturbation

In the parameter study, the initial velocity perturbation is varied from subsonic to supersonic (but subAlfvénic) values (see Table 3.3). This perturbation affects the subsequent evolution of the cloud and the formation of cores; however, the perturbation also decays

[2] Although the initial parameters for the velocity perturbation are the same, the realization of the random velocity field is different.

Table 5.1: Best-Fit to Equation 5.5

Case	C_1	C_2
All $B_{\rm los}$	6.78	-1.6
$\lvert B_{\rm los}\rvert > 1\,\mu$G	1.47	0.39
$\lvert B_{\rm los}\rvert > 10\,\mu$G	0.91	0.32

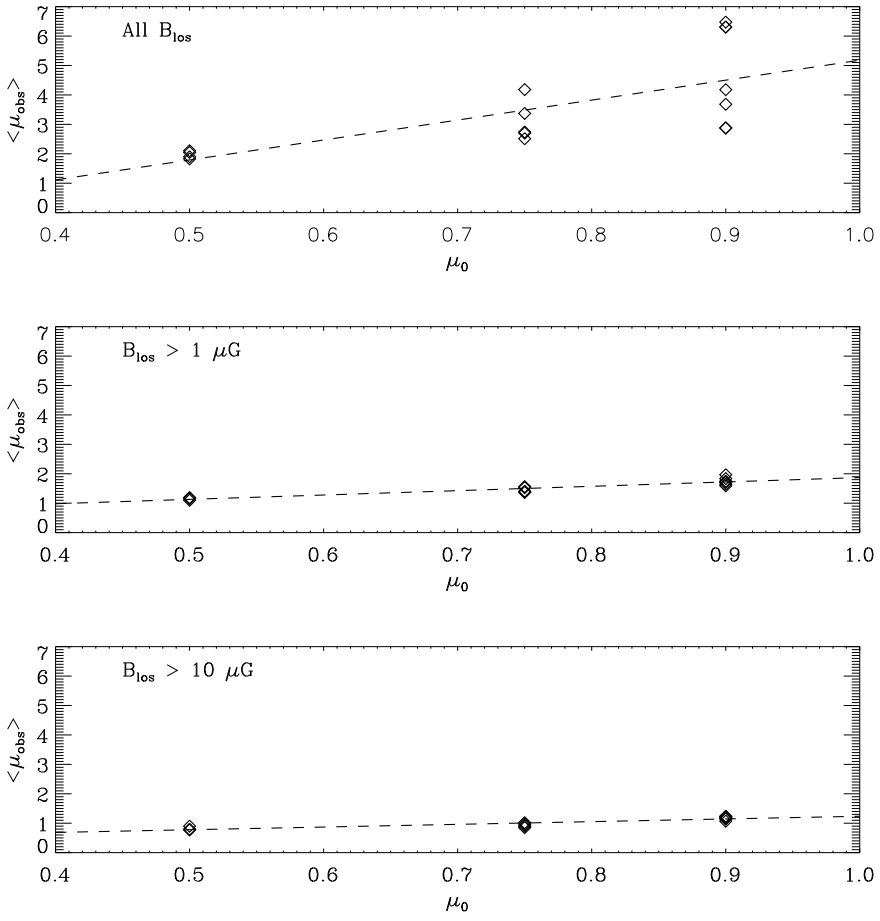

Figure 5.10: Fit of the mean $\mu_{\rm obs}$ to the actual μ_0. *Top:* All lines-of-sight are included in the calculation of the average. *Middle:* Only lines-of-sight with $|B_{\rm los}| > 1\,\mu$G are included. *Bottom:* Only lines-of-sight with $|B_{\rm los}| > 10\,\mu$G are included. In each case, the dashed line is the fit to the data.

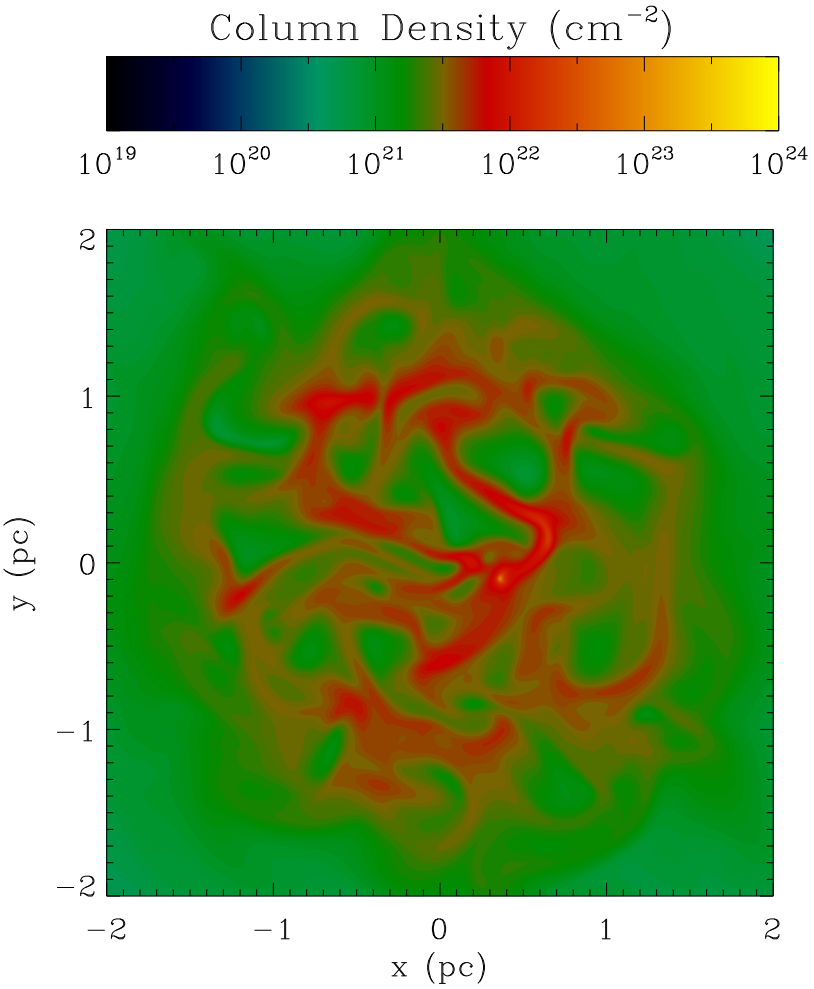

Figure 5.11: Column-density plot for Run H2 at viewing angle $\theta = 0°$.

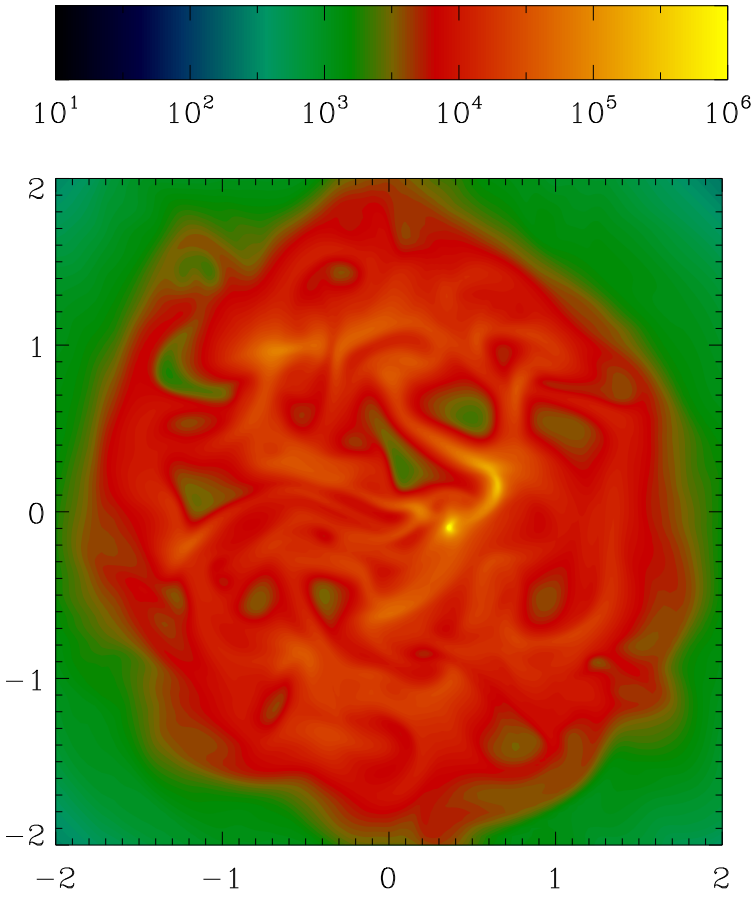

Figure 5.12: Maximum density along a line of sight for model H2 at viewing angle $\theta = 0°$.

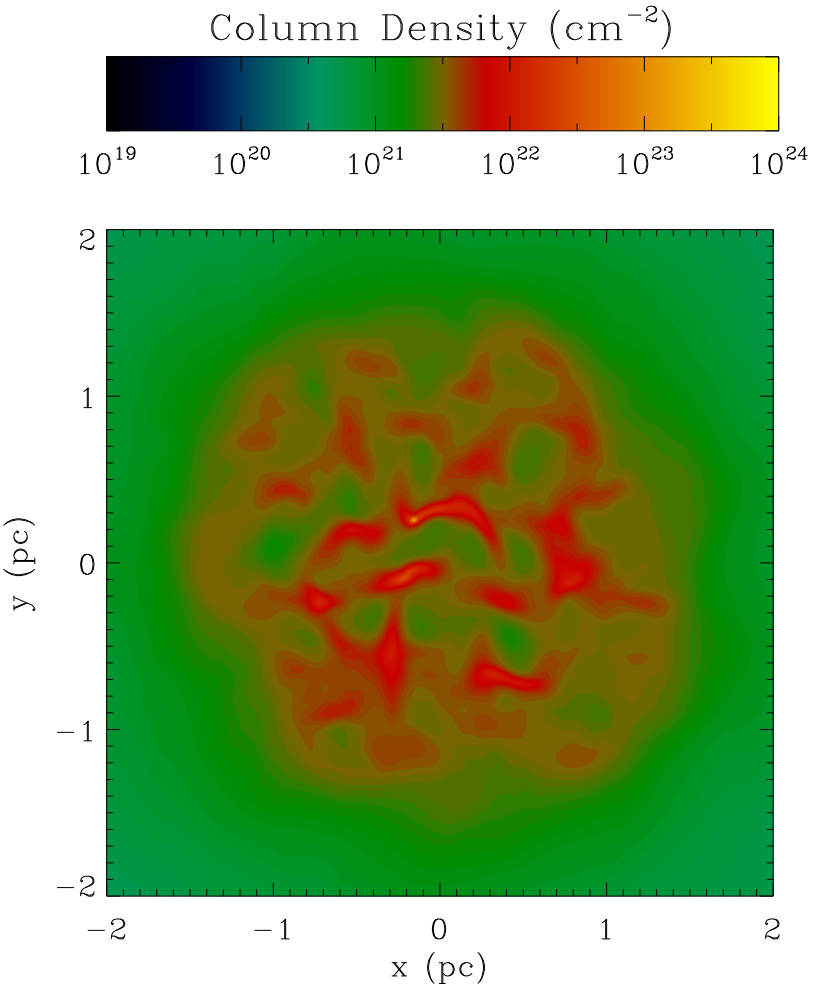

Figure 5.13: Column-density plot for Run H1. This run has the same values for $v_{\rm turb}$ and $v_{\rm sol}$ as H2 (although not the same realizations of the velocity field) but has a different ionization ($K_{\rm CR} = 1 \times 10^{-3}$).

as the cloud evolves. As discussed in §5.1, for a typical model cloud a significant fraction of the kinetic energy is dissipated within the first million years due to shocks and ambipolar diffusion.

The velocity dispersion in the cloud at the end of the run depends on a variety of factors. The rate at which ambipolar diffusion dissipates wave energy depends on the ionization within the cloud. The longer it takes for the cloud to produce supercritical fragments, the longer ambipolar diffusion has to dissipate the wave energy. Figure 5.14 shows the final velocity dispersion in the cloud versus the initial solenoidal velocity perturbation for the three mass-to-flux ratios used in the parameter study. In all cases, the final velocity dispersions are roughly sonic, regardless of the ionization or mass-to-flux ratio. For $\mu_0 = 0.9$, there is a slight increase in the final velocity dispersion with $v_{\rm sol}$ which is likely due to the shorter evolutionary timescale of the cloud.

Although the velocity dispersion in the final state is universally sonic, we have not considered the possibility of energy injection or driving. The injection of energy from internal or external sources over the life of the cloud could replenish some (or all) of the kinetic energy within the cloud, increasing the velocity dispersion at the end of the run. Since clouds that have not yet given birth to stars (the ones of interest here) have no internal sources of turbulent energy, one has to rely on external sources for replenishing the rapidly decaying turbulence or to "initial" large-scale oscillations of the cloud, left over from their formation mechanism(s).

5.3 Collective Core Properties

Within a model cloud, there are individual high-density fragments (or *cores*) which are the progenitors of one or more stars. In this section we discuss the properties of these cores and the dependence of these properties on the initial conditions of model clouds.

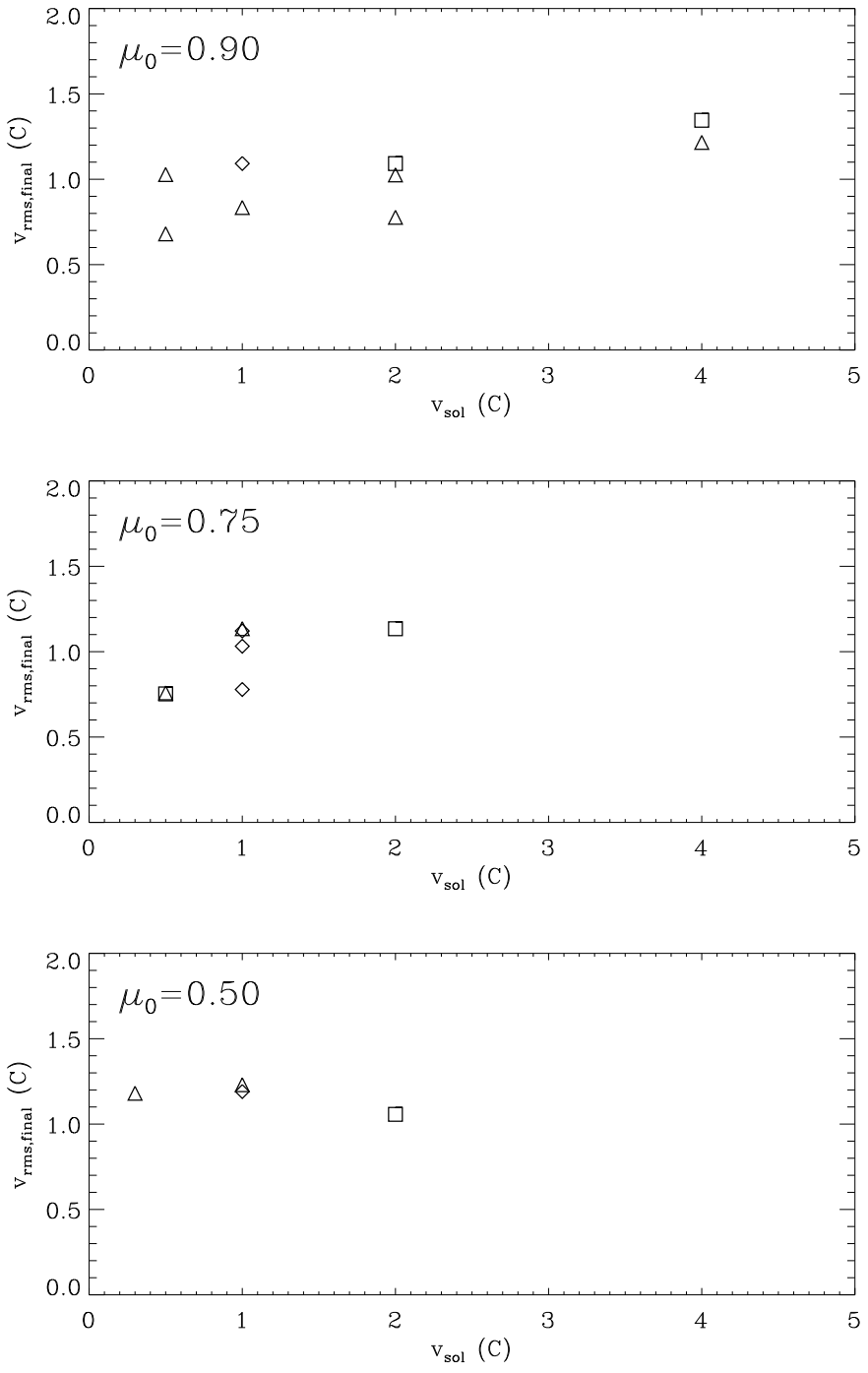

Figure 5.14: The final RMS velocity for the cloud versus the initial solenoidal velocity perturbation ($v_{\rm sol}$) for $\mu_0 = 0.9$ (top), $\mu_0 = 0.75$ (middle), and $\mu_0 = 0.50$ (bottom). Squares correspond to runs with $K_{\rm CR} = 0.005$, triangles correspond to $K_{\rm CR} = 0.003$, and diamonds correspond to runs with $K_{\rm CR} = 0.001$.

5.3.1 The B-ρ Relation

One of the simplest predictions of the magnetically-regulated theory of star formation is the relation between the central density of a collapsing object and its magnetic field. As discussed previously, once a core is moderately supercritical ($\mu \approx 2$), the mass-to-flux ratio does not change significantly until ambipolar diffusion reawakens at densities beyond the scope of this project (Desch and Mouschovias 2001; Tassis and Mouschovias 2007; Kunz and Mouschovias 2010). During this near-flux-freezing collapse, the magnetic field strength scales as $B_c \propto \rho^{0.47}$.

Figure (5.15) shows the central magnetic field versus central density for the simulated cores. Fitting to all cores, we find that $B_c \propto n^{0.371\pm0.005}$, smaller than expected. If cores with low densities are excluded, however, the fitted curve becomes $B_c \propto n^{0.473\pm0.046}$. Although axisymmetric simulations find an expontent of 0.47, identical to the best-fit value, this high degree of agreement is likely a coindidence. The variance in the fit is unable to distinguish between an exponent of 0.5 and one of 0.47. Additionally, since we do not resolve these high-density regions well, it is unlikely that the code would accurately capture the slight effect of ambipolar diffusion. The smaller slope found when including the low-density cores is likely due to the fact that the $B-\rho$ relation makes a smooth transition between B_c being almost independent of density (during the ambipolar diffusion controlled evolution; see Fig 3) and the $B_c \propto \rho^{1/2}$ relation (after dynamical contraction sets in).

Since this relation is seen in both simulations (e.g. Fiedler and Mouschovias 1992; Basu and Mouschovias 1994; Desch and Mouschovias 2001) and in observations (Crutcher 1999), this result should not be viewed as a new prediction but instead as a validation of the code.

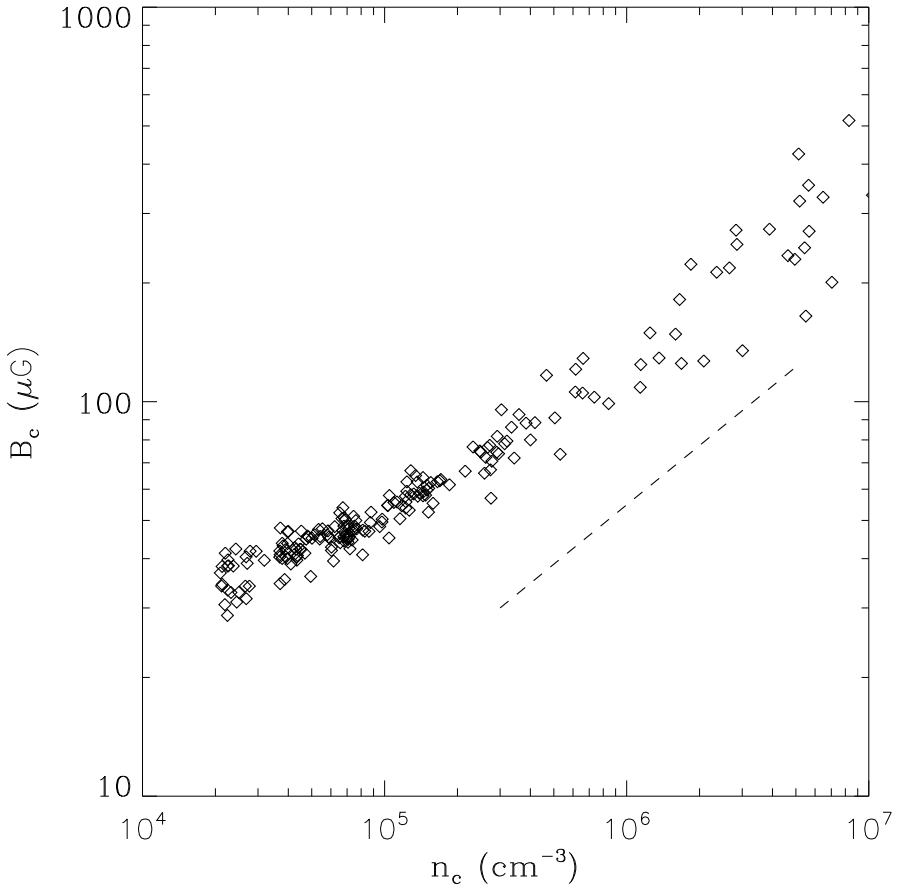

Figure 5.15: Central magnetic field versus central density for the simulated cores. The dashed line indicates a slope of $1/2$, which is expected by theory.

5.3.2 Core Properties

Within the cloud there are higher-density fragments which become unstable and collapse. As a threshold we use $n_{\rm core} = 2 \times 10^4 \ {\rm cm}^{-3}$ to define the boundaries of the cores. This roughly corresponds to the density at which $\rm NH_3$ becomes observable in molecular clouds. This threshold is not unique as the equations can be made dimensionless, and, as a result, the choice of threshold density for defining core contours can play an important role in determining the core properties.

To decompose the gas with $n_{\rm n} > n_{\rm core}$ into individual cores within the model cloud we employ the CLUMPFIND package (Williams et al. 1994). CLUMPFIND works by contouring the data at increasingly larger thresholds until disconnected objects are found. In addition to the data, it requires two important parameters as input: the minimum threshold (which we take to be $n_{\rm core}$ for our purposes) and the step ($\Delta n_{\rm step}$) with which it increases the threshold density. In a study of the effect of changing these parameters in an observational setting, Pineda et al. (2009) found that while the changing of the initial threshold can modify results slightly, very different results can be achieved by changing the step $\Delta n_{\rm step}$.

We modify the CLUMPFIND algorithm in two ways. First, we preprocess our density data by applying a smoothing function. This serves to smooth out undesirable fluctuations at the grid level. The smoothing function takes the form

$$\bar{\rho}_{\rm n}(\boldsymbol{x_0}) = A \int \rho(\boldsymbol{x}) \exp\left(-\frac{(\boldsymbol{x}-\boldsymbol{x_0})^2}{2\sigma^2}\right) dV \ , \tag{5.7}$$

where A is a normalization factor for the Gaussian and σ is the smoothing parameter. The domain of the integral is taken to be the zone centered at $\boldsymbol{x_0}$ and all it's neighboring zones, including those on the diagonals. For our purposes, the smoothing factor is taken to be $\sigma = \Delta x$, the local grid spacing.

5.3.3 Core Masses

Cores exhibit a distribution of masses within any molecular cloud. If molecular clouds were simply uniform clouds of gas, the cloud would fragment into cores each with roughly the Jeans mass. Why then do we see a distribution of core masses? Simulations of turbulence – both hydrodynamic and magnetohydrodyamic – have found that the densities are distributed lognormally. This distribution of densities results in a distribution of thermal masses which fits the distribution of core masses; however, there is a high-mass tail to the mass function which is not explained.

Using the results of Morton (1991), Kunz and Mouschovias (2009a) constructed a mass function based on the variation of the mass-to-flux ratio. Since the wavelength of optimal growth increases near the critical mass-to-flux ratio, a distribution of values of μ_0 results in a distribution of masses. Kunz and Mouschovias (2009a) used this fact to construct a mass function which agreed well with the observed mass function of more than 300 cores in Orion.

Figure 5.16 shows the core mass function compiled from all the runs. The mass function takes the qualitatively correct form, with a turnover and a high-mass tail. Fit to a power-law (dashed line), the high-mass end of the mass function has a slope of -1.48 ± 0.12.

As previously mentioned, the mass function of Kunz and Mouschovias (2009a) depends on the increase in the fragmentation lengthscale near the critical mass-to-flux ratio. Figure 5.17 shows the nearest-neighbour spacing versus the mass-to-flux ratio. There is no clear dependence of the inter-core spacing on the mass-to-flux ratio. Although there is no clear dependence of the spacing on μ_0, the mass does show a dependence on μ_0 (see Fig. 5.18). Cores formed in the highly subcritical clouds ($\mu_0 = 0.5$) have, on average, masses comparable to the thermal critical mass whereas there is a broader distribution of average masses for clouds closer to critical. The linear analysis indicates that the increase in fragmentation length (and thus average mass) should be more pronounced for

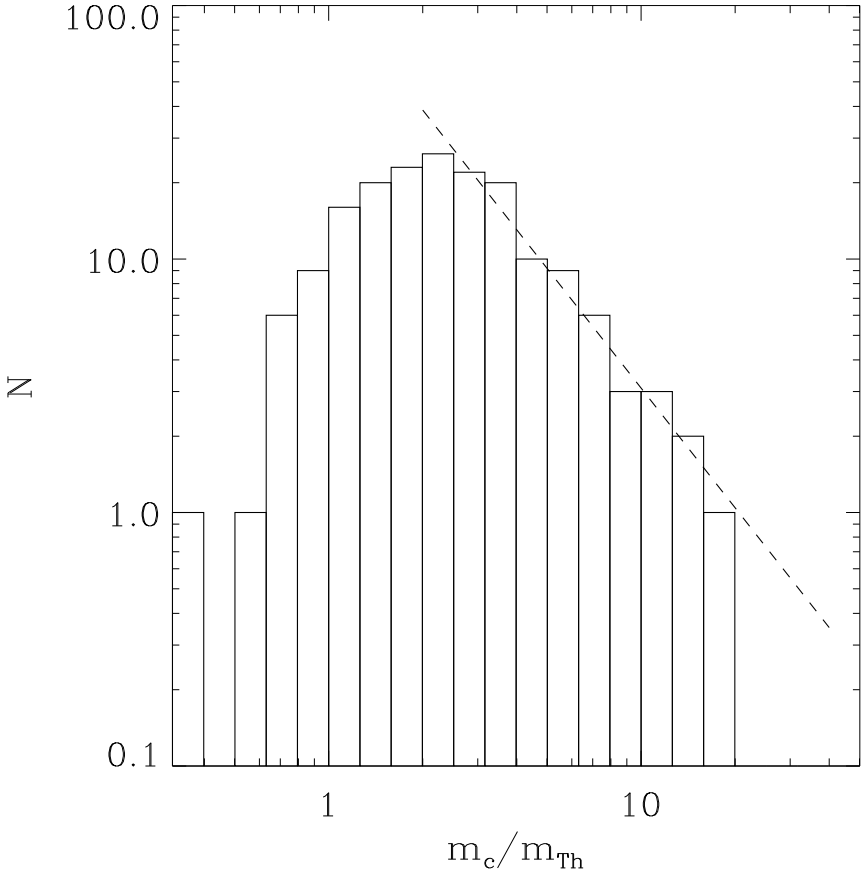

Figure 5.16: The distribution of core masses from all the runs. The masses are normalized to the mean thermal mass for the run.

higher values of the ionization parameter $K_{\rm CR}$; however, this does not seem to hold true in Figure 5.18. The reason for this is that for many of the runs the velocity perturbation is supersonic. Just as in equation 3.2, the velocity perturbation can be thought of as a scale-dependent pressure. The increased turbulent energy at larger lengthscales acts to suppress the growth of longer wavelengths, resulting in smaller cores.

Of the three mass-to-flux ratios studied in the parameter study, the largest variation in mean masses is seen in the runs with $\mu_0 = 0.9$. For the runs with $\mu_0 = 0.9$, only those runs with subsonic solenoidal velocity perturbations ($v_{\rm sol}$) show significant increases in the mean core masses (Fig. 5.19). There is no correlation seen between the mean core masses and the turbulent support (Fig. 5.21). The turbulent support contribution to the velocity perturbation is short lived, thus it is unlikely to affect the long-term evolution of the cores[3].

5.3.4 Core Shapes

As discussed in §1.1.1, the observations of core shapes indicate that cores are oblate or triaxial in nature. The projected shape of the core is calculated using the two-dimensional moment matrix

$$I_{i,j} = \int \sigma X_i X_j dA \ , \tag{5.8}$$

where σ is the column density along the line-of-sight, X_i is a coordinate on the plane of the sky and the integral is taken over the projected surface of the core. The eigenvalues of this matrix are Ma^2 and Mb^2 where a and b are the lengths of the axes of the core and M is the core mass.

[3]A run was done which included only a turbulent support term in the velocity perturbation without a solenoidal component ($v_{\rm sol} = 0$). Although the run initially demonstated small-scale structure, the perturbation dissipated within a million years leaving the cloud in a flattened, axisymmetric state which ultimately formed a central object but little else. This run was not included in the final parameter study as it is not a realistic initial state for a cloud. Instead, it was done to gauge the lifetime of the turbulent velocity component.

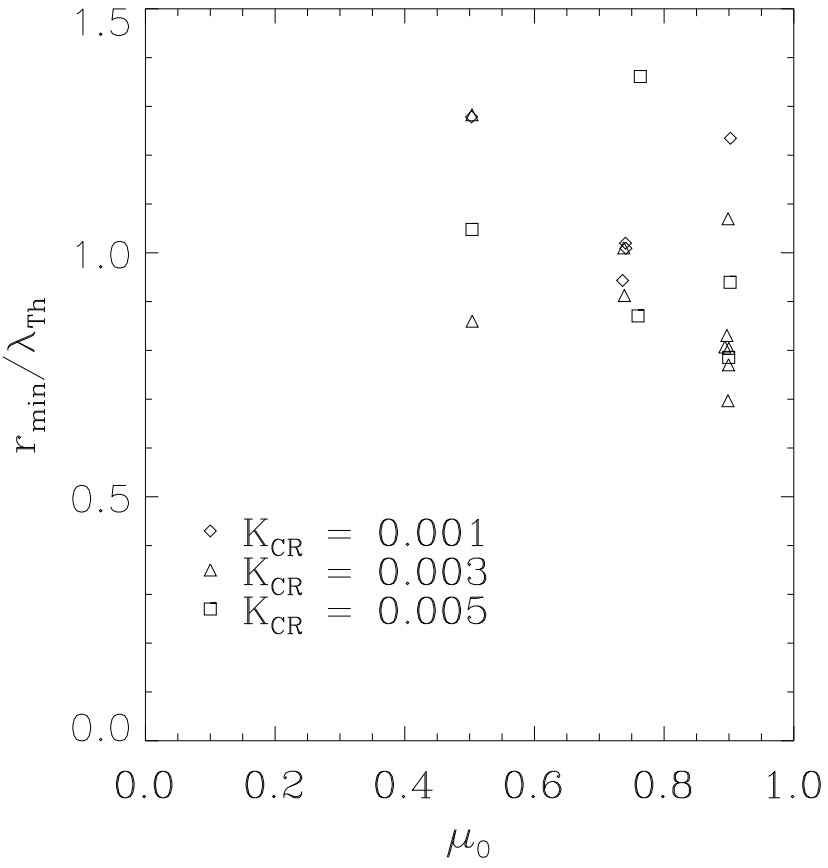

Figure 5.17: The average nearest neighbor spacing versus μ_0 for all the runs. The symbols indicate the ionization constant $K_{\rm CR}$ for the runs.

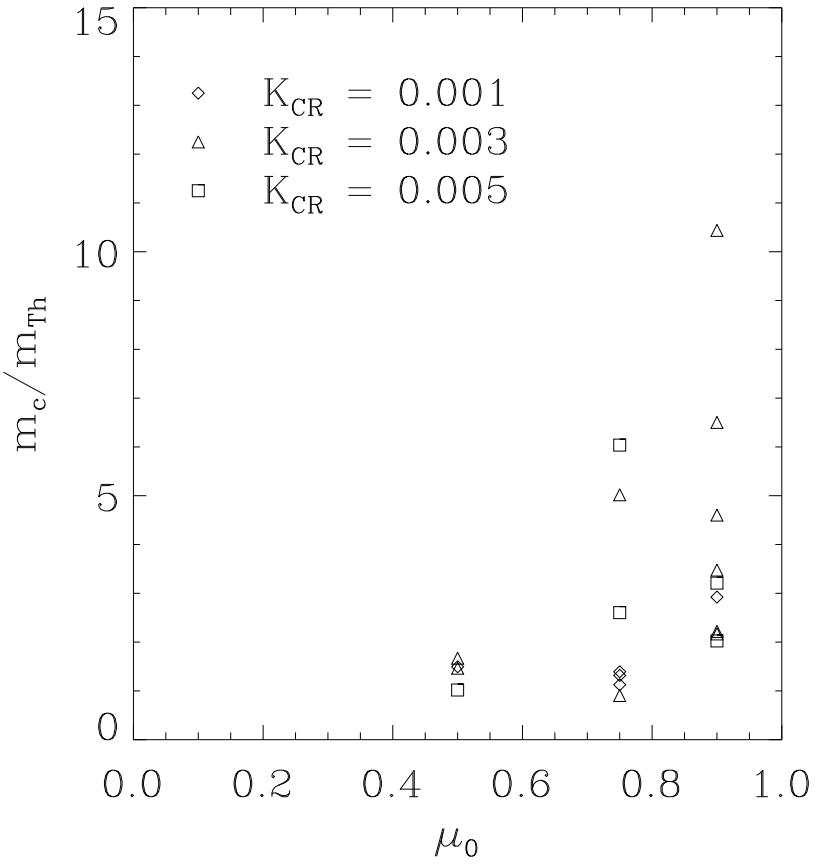

Figure 5.18: The average core mass versus μ_0 for all the runs. The symbols indicate the ionization parameter $K_{\rm CR}$ for the runs.

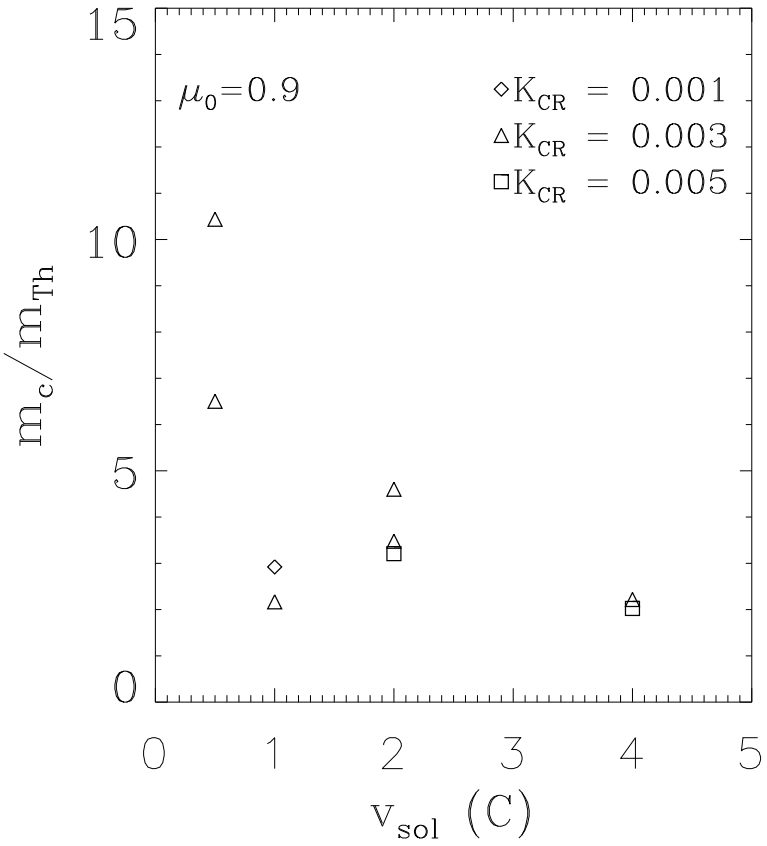

Figure 5.19: The mean mass versus the initial solenoidal velocity perturbation ($v_{\rm sol}$) for all the runs with initial mass-to-flux ratios of $\mu_0 = 0.9$. There is a noticeable trend towards larger masses for smaller velocity perturbations.

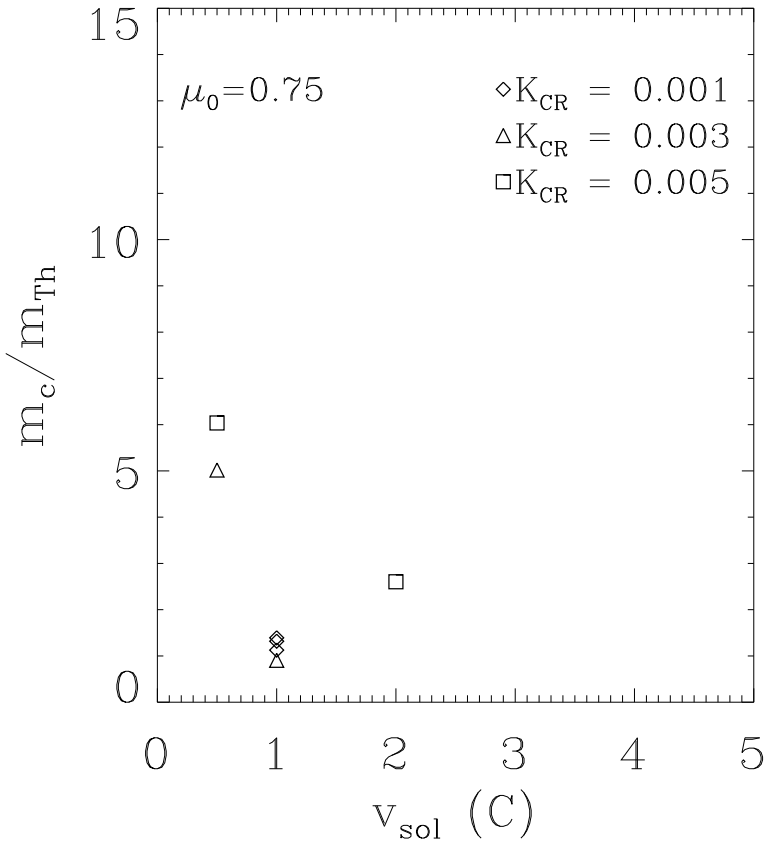

Figure 5.20: The mean mass versus the initial solenoidal velocity perturbation ($v_{\rm sol}$) for all the runs with initial mass-to-flux ratios of $\mu_0 = 0.75$. There is a noticeable trend towards larger masses for smaller velocity perturbations; however, it is not as pronounced as in the $\mu_0 = 0.9$ case.

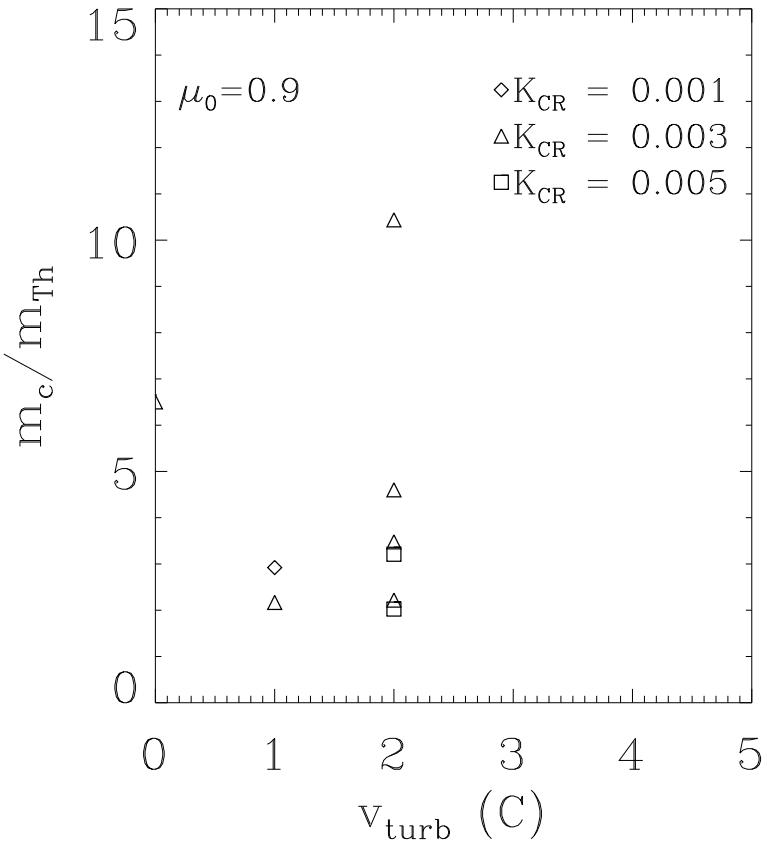

Figure 5.21: The mean mass versus the initial turbulent velocity perturbation ($v_{\rm turb}$) for all the runs with initial mass-to-flux ratios of $\mu_0 = 0.90$. There is no obvious trend.

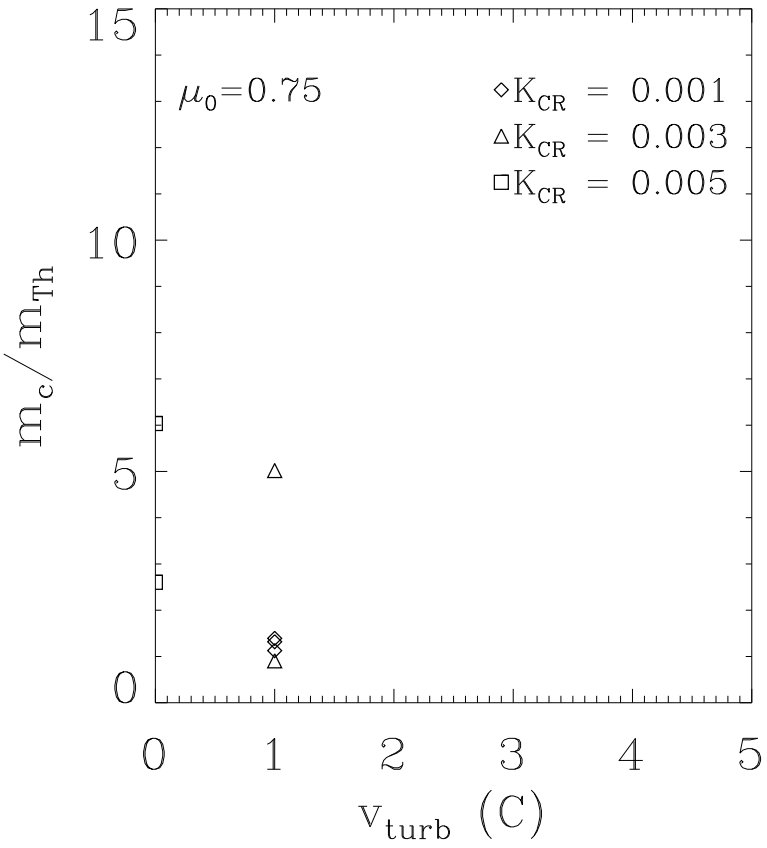

Figure 5.22: The mean mass versus the initial turbulent velocity perturbation ($v_{\rm turb}$) for all the runs with initial mass-to-flux ratios of $\mu_0 = 0.75$. There is no obvious trend.

In a similar fashion, we can calculate the shapes of the cores in the three dimensional simulations using the matrix $I_{i,j}$:

$$I_{i,j} = \int_{\rm core} \rho_{\rm n}(\boldsymbol{x}) x_i x_j dV \ , \tag{5.9}$$

where x_i are the cartesian coordinates and the integral is over the volume of a core. The eigenvalues of this matrix are Ma^2, Mb^2, Mc^2 where $a > b > c$ and M is the core mass. The quantities $\beta = b/a$ and $\gamma = c/a$ are the axes ratios of the core. For all our runs, the minor axis γ is roughly aligned with the mean magnetic field and in all cases is significantly shorter than the major axis. This is due to the flattening of the cloud along the magnetic field lines.

Overall, the simulations form many more triaxial and prolate cores than expected (see Fig. 5.23). A possible explanation is that the strong velocity perturbations are the cause; however, this does not seem to be the case as there is no correlation between the initial or final velocity dispersions and the number of prolate cores. The prolate cores formed in our simulations do differ from those seen in simulations of hydromagnetic turbulence in that for our simulations the magnetic field is always roughly aligned with the minor axis.

5.3.5 Magnetic Field Orientation

For each core, we also look at the relative orientation of the minor axis, as determined in §5.3.4, and the mean magnetic field within the core. We define the mean magnetic field direction by

$$\bar{\boldsymbol{B}} = \frac{1}{M} \int_{\rm core} \rho_{\rm n} \boldsymbol{B} dV \ , \tag{5.10}$$

where M is the mass of the core. The angle between the minor axis and the mean magnetic field is then

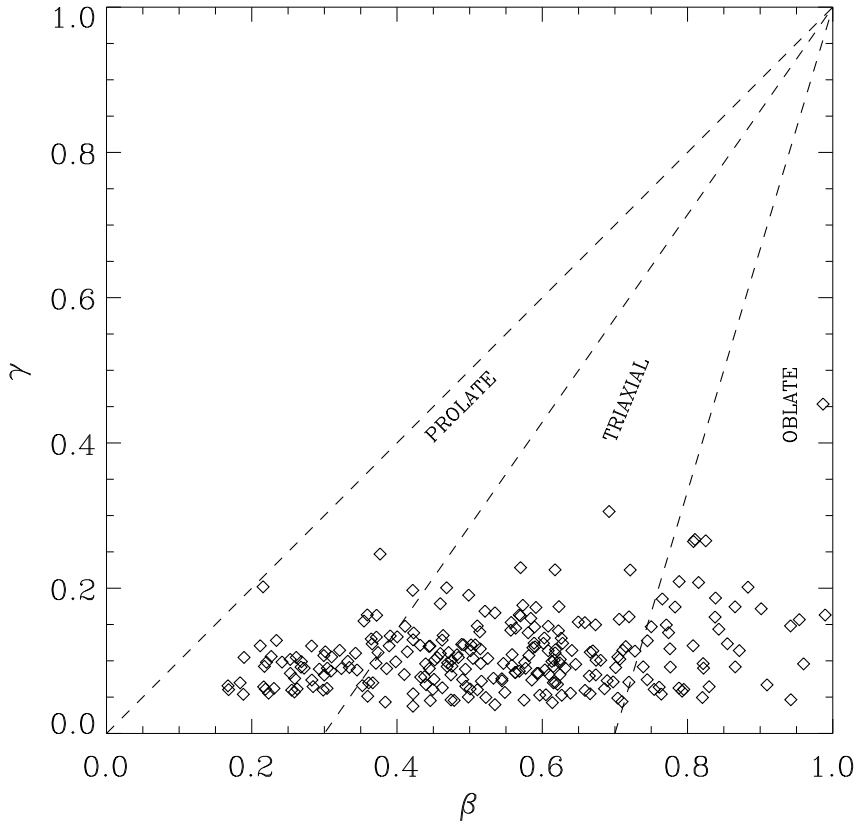

Figure 5.23: The shapes of all the cores in our parameter study. The lengths of the axis are $a > b > c$ and the axis ratios are $\beta = b/a$ and $\gamma = c/a$. The minor axis is significantly shorter than the major axis.

$$\theta = \cos^{-1}\left(\frac{\bar{\boldsymbol{B}}\cdot\hat{\boldsymbol{e}}_{\mathbf{minor}}}{|\bar{B}|}\right) , \tag{5.11}$$

where $\hat{\boldsymbol{e}}_{\mathbf{minor}}$ is a unit vector in the direction of the minor axis of the core. Figure 5.24 shows the average angle θ for each run. The average angle between the magnetic field and the minor axis typically ranges from 5° to 15° with little dependence on the mass-to-flux ratio μ_0, although there does seem to be more variation in the angle as μ_0 nears the critical value. There is no correlation of the average angle with either the final $v_{\rm rms}$ or the initial $v_{\rm sol}$.

The reason for the misalignment between the mean magnetic field and the core minor axis is not due to fluctuations in the magnetic field but fluctuations in the cloud (disk-like) shape. Although the field lines are nearly straight and parallel, undulations in the disk along the field lines (see Fig. 5.25) cause a misalignment between the minor axis and the mean magnetic field.

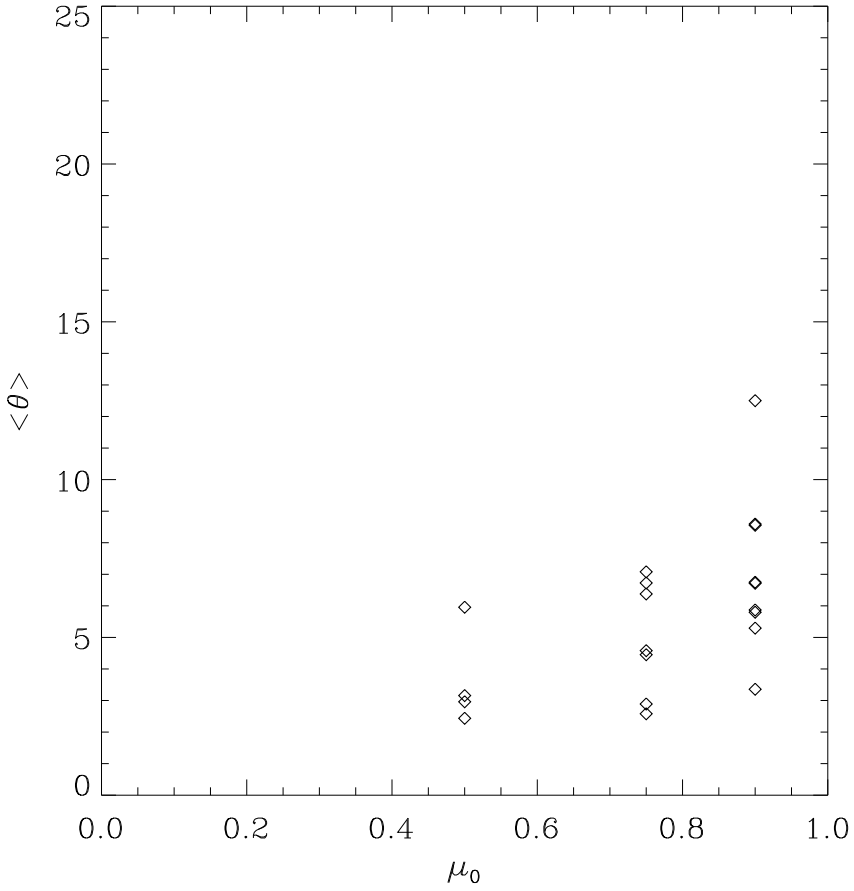

Figure 5.24: Average angle θ between the minor axis of a core and its mean magnetic field for each run.

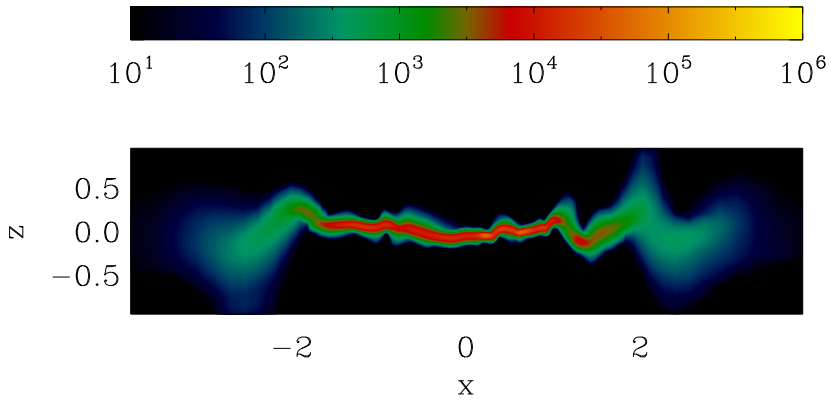

Figure 5.25: The volume density along a slice through the center of model cloud L21.

Chapter 6

Summary and Future Directions

6.1 Summary

We have presented the results of a study investigating the fragmentation of weakly-ionized, magnetically-supported molecular clouds under varied initial mass-to-flux ratios, velocity perturbations, and ionizations. By the end of their respective runs, all the model clouds are flattened along the magnetic field lines with $10 - 20$ cores formed in each. These cores have a broad distribution of masses with larger average masses seen for runs with mass-to-flux ratios near the critical value. The distribution of masses exhibed a shape similar to that of the observed IMF with a high-mass slope of -1.48, consistent with the observed slope, although the exact value varies depending on the distribution of initial mass-to-flux ratios. Although the magnetic field lines remain roughly straight and parallel, the mean field within the cores was still between 5° and 15° from the minor axis due to undulations in the disklike clouds.

All the model clouds, even those with subsonic velocity perturbations, exhibited log-normal distributions of column densities which had previously been thought to be a sign of supersonic turbulence. Also, despite the fact that all the model clouds were magnetically subcritical, the *observed* mass-to-flux ratio along a random line-of-sight was likely to be supercritical, and the correction factor required to account for this is larger than the factor of 3 commonly used.

We also observed the formation of filamentary structures within the simulation; however, unlike in simulations of superAlfvénic turbulence, the magnetic field is aligned per-

pendicular to the major axis of the filament.

6.2 Future Directions

AMR and Increased Resolution. The simulations performed here are resolution limited in that we cannot follow the evolution of individual cores. This fact prevents us from following the evolution of the clouds after the formation of the first few cores. The inclusion of automatic mesh refinement and/or sink particles will allow the simulations to proceed much farther.

Accurate modelling of external driving. Current numerical models of driving inject energy in each zone in the computational domain. Since the likely source for turbulent energy in clouds without protostars is external to the clouds, this method is not physically reasonable. A more realistic method for studying energy injection into model clouds would only inject energy in regions external to the cloud, allowing for the propagation into or reflection off the cloud boundaries. It is not at present clear whether this kind of external source of turbulence will provide support against the self-gravity of a cloud or whether it will actually facilitate its collapse.

References

Alves, F. O., Franco, G. A. P., and Girart, J. M. (2008). Optical polarimetry toward the Pipe nebula: revealing the importance of the magnetic field. *A&A*, 486:L13–L16.

André, P., Men'shchikov, A., Bontemps, S., Könyves, V., Motte, F., Schneider, N., Didelon, P., Minier, V., Saraceno, P., Ward-Thompson, D., di Francesco, J., White, G., Molinari, S., Testi, L., Abergel, A., Griffin, M., Henning, T., Royer, P., Merín, B., Vavrek, R., Attard, M., Arzoumanian, D., Wilson, C. D., Ade, P., Aussel, H., Baluteau, J., Benedettini, M., Bernard, J., Blommaert, J. A. D. L., Cambrésy, L., Cox, P., di Giorgio, A., Hargrave, P., Hennemann, M., Huang, M., Kirk, J., Krause, O., Launhardt, R., Leeks, S., Le Pennec, J., Li, J. Z., Martin, P. G., Maury, A., Olofsson, G., Omont, A., Peretto, N., Pezzuto, S., Prusti, T., Roussel, H., Russeil, D., Sauvage, M., Sibthorpe, B., Sicilia-Aguilar, A., Spinoglio, L., Waelkens, C., Woodcraft, A., and Zavagno, A. (2010). From filamentary clouds to prestellar cores to the stellar IMF: Initial highlights from the Herschel Gould Belt Survey. *A&A*, 518:L102+.

Andre, P., Ward-Thompson, D., and Barsony, M. (2000). From Prestellar Cores to Protostars: the Initial Conditions of Star Formation. *Protostars and Planets IV*, pages 59–+.

Arons, J. and Max, C. E. (1975). Hydromagnetic Waves in Molecular Clouds. *ApJL*, 196:L77+.

Basu, S., Ciolek, G. E., Dapp, W. B., and Wurster, J. (2009a). Magnetically-regulated fragmentation induced by nonlinear flows and ambipolar diffusion. *NewA*, 14:483–495.

Basu, S., Ciolek, G. E., and Wurster, J. (2009b). Nonlinear evolution of gravitational fragmentation regulated by magnetic fields and ambipolar diffusion. *NewA*, 14:221–237.

Basu, S. and Mouschovias, T. C. (1994). Magnetic braking, ambipolar diffusion, and the formation of cloud cores and protostars. 1: Axisymmetric solutions. *ApJ*, 432:720–741.

Benson, P. J. and Myers, P. C. (1989). A survey for dense cores in dark clouds. *ApJS*, 71:89–108.

Bonnor, W. B. (1956). Boyle's Law and gravitational instability. *MNRAS*, 116:351–+.

Brunt, C. M. (2003). Large-Scale Turbulence in Molecular Clouds. *ApJ*, 583:280–295.

Brunt, C. M., Heyer, M. H., and Mac Low, M. (2009). Turbulent driving scales in molecular clouds. *A&A*, 504:883–890.

Ciolek, G. E. and Basu, S. (2006). Formation and Collapse of Nonaxisymmetric Protostellar Cores in Planar Magnetic Interstellar Clouds: Formulation of the Problem and Linear Analysis. *ApJ*, 652:442–457.

Ciolek, G. E. and Mouschovias, T. C. (1993). Ambipolar Diffusion, Interstellar Dust, and the Formation of Cloud Cores and Protostars. I. Basic Physics and Formulation of the Problem. *ApJ*, 418:774–+.

Ciolek, G. E. and Mouschovias, T. C. (1994). Ambipolar diffusion, interstellar dust, and the formation of cloud cores and protostars. 3: Typical axisymmetric solutions. *ApJ*, 425:142–160.

Ciolek, G. E. and Mouschovias, T. C. (1995). Ambipolar Diffusion, Interstellar Dust, and the Formation of Cloud Cores and Protostars. IV. Effect of Ultraviolet Ionization and Magnetically Controlled Infall Rate. *ApJ*, 454:194–+.

Crutcher, R. M. (1999). Magnetic Fields in Molecular Clouds: Observations Confront Theory. *ApJ*, 520:706–713.

Crutcher, R. M. and Kazes, I. (1983). The magnetic field of the NGC 2024 molecular cloud - Detection of OH line Zeeman splitting. *A&A*, 125:L23–L26.

Dapp, W. B. and Basu, S. (2010). Averting the magnetic braking catastrophe on small scales: disk formation due to Ohmic dissipation. *A&A*, 521:L56+.

Desch, S. J. and Mouschovias, T. C. (2001). The Magnetic Decoupling Stage of Star Formation. *ApJ*, 550:314–333.

Ebert, R. (1957). Zur Instabilität kugelsymmetrischer Gasverteilungen. Mit 2 Textabbildungen. *ZAP*, 42:263–+.

Evans, C. R. and Hawley, J. F. (1988). Simulation of magnetohydrodynamic flows - A constrained transport method. *ApJ*, 332:659–677.

Fiedler, R. A. and Mouschovias, T. C. (1992). Ambipolar diffusion and star formation: Formation and contraction of axisymmetric cloud cores. I - Formulation of the problem and method of solution. *ApJ*, 391:199–219.

Fiedler, R. A. and Mouschovias, T. C. (1993). Ambipolar Diffusion and Star Formation: Formation and Contraction of Axisymmetric Cloud Cores. II. Results. *ApJ*, 415:680–+.

Girart, J. M., Rao, R., and Marrone, D. P. (2006). Magnetic Fields in the Formation of Sun-Like Stars. *Science*, 313:812–814.

Goldreich, P. and Kwan, J. (1974). Molecular Clouds. *ApJ*, 189:441–454.

Goodman, A. A., Crutcher, R. M., Heiles, C., Myers, P. C., and Troland, T. H. (1989). Measurement of magnetic field strength in the dark cloud Barnard 1. *ApJL*, 338:L61–L64.

Goodman, A. A., Pineda, J. E., and Schnee, S. L. (2009). The "True" Column Density Distribution in Star-Forming Molecular Clouds. *ApJ*, 692:91–103.

Hartmann, L. (2001). On Age Spreads in Star-forming Regions. *AJ*, 121:1030–1039.

Hartmann, L., Ballesteros-Paredes, J., and Bergin, E. A. (2001). Rapid Formation of Molecular Clouds and Stars in the Solar Neighborhood. *ApJ*, 562:852–868.

Hayes, J. C., Norman, M. L., Fiedler, R. A., Bordner, J. O., Li, P. S., Clark, S. E., ud-Doula, A., and Mac Low, M. (2006). Simulating Radiating and Magnetized Flows in Multiple Dimensions with ZEUS-MP. *ApJS*, 165:188–228.

Heiles, C. and Troland, T. H. (2005). The Millennium Arecibo 21 Centimeter Absorption-Line Survey. IV. Statistics of Magnetic Field, Column Density, and Turbulence. *ApJ*, 624:773–793.

Heyer, M., Krawczyk, C., Duval, J., and Jackson, J. M. (2009). Re-Examining Larson's Scaling Relationships in Galactic Molecular Clouds. *ApJ*, 699:1092–1103.

Heyer, M. H., Williams, J. P., and Brunt, C. M. (2006). Turbulent Gas Flows in the Rosette and G216-2.5 Molecular Clouds: Assessing Turbulent Fragmentation Descriptions of Star Formation. *ApJ*, 643:956–964.

Hezareh, T., Houde, M., McCoey, C., and Li, H. (2010). Observational Determination of the Turbulent Ambipolar Diffusion Scale and Magnetic Field Strength in Molecular Clouds. *ApJ*, 720:603–607.

Hoyle, F. (1953). On the Fragmentation of Gas Clouds Into Galaxies and Stars. *ApJ*, 118:513–+.

Indebetouw, R. and Zweibel, E. G. (2000). Fragmentation Instability of Molecular Clouds: Numerical Simulations. *ApJ*, 532:361–376.

Jeans, J. H. (1902). The Stability of a Spherical Nebula. *Royal Society of London Philosophical Transactions Series A*, 199:1–53.

Johnstone, D. and Bally, J. (2006). Large-Area Mapping at 850 μm. V. Analysis of the Clump Distribution in the Orion A South Molecular Cloud. *ApJ*, 653:383–397.

Jones, C. E., Basu, S., and Dubinski, J. (2001). Intrinsic Shapes of Molecular Cloud Cores. *ApJ*, 551:387–393.

Kainulainen, J., Beuther, H., Henning, T., and Plume, R. (2009). Probing the evolution of molecular cloud structure. From quiescence to birth. *A&A*, 508:L35–L38.

Kazes, I. and Crutcher, R. M. (1986). Measurement of magnetic-field strengths in molecular clouds Detection of OH-line Zeeman splitting. *A&A*, 164:328–336.

Kirk, H., Johnstone, D., and Tafalla, M. (2007). Dynamics of Dense Cores in the Perseus Molecular Cloud. *ApJ*, 668:1042–1063.

Kudoh, T. and Basu, S. (2008). Three-dimensional Simulation of Magnetized Cloud Fragmentation Induced by Nonlinear Flows and Ambipolar Diffusion. *ApJL*, 679:L97–L100.

Kunz, M. W. and Mouschovias, T. C. (2009a). The initial core mass function due to ambipolar diffusion in molecular clouds. *MNRAS*, 399:L94–L98.

Kunz, M. W. and Mouschovias, T. C. (2009b). The Nonisothermal Stage of Magnetic Star Formation. I. Formulation of the Problem and Method of Solution. *ApJ*, 693:1895–1911.

Kunz, M. W. and Mouschovias, T. C. (2010). The non-isothermal stage of magnetic star formation - II. Results. *MNRAS*, 408:322–341.

Larson, R. B. (1981). Turbulence and star formation in molecular clouds. *MNRAS*, 194:809–826.

Li, P. S., McKee, C. F., Klein, R. I., and Fisher, R. T. (2008). Sub-Alfvénic Nonideal MHD Turbulence Simulations with Ambipolar Diffusion. I. Turbulence Statistics. *ApJ*, 684:380–394.

Lombardi, M., Alves, J., and Lada, C. J. (2006). 2MASS wide field extinction maps. I. The Pipe nebula. *A&A*, 454:781–796.

Mac Low, M., Norman, M. L., Konigl, A., and Wardle, M. (1995). Incorporation of ambipolar diffusion into the ZEUS magetohydrodynamics code. *ApJ*, 442:726–735.

Mathewson, D. S., van der Kruit, P. C., and Brouw, W. N. (1972). A High Resolution Radio Continuum Survey of M51 and NGC 5195 at 1415 MHz. *A&A*, 17:468–+.

McDaniel, E. W. and Mason, E. A. (1973). *The Mobility and Diffusion of Ions and Gases*.

McKee, C. F., Li, P. S., and Klein, R. I. (2010). Sub-Alfvénic Non-ideal MHD Turbulence Simulations with Ambipolar Diffusion. II. Comparison with Observation, Clump Properties, and Scaling to Physical Units. *ApJ*, 720:1612–1634.

Mellon, R. R. and Li, Z. (2008). Magnetic Braking and Protostellar Disk Formation: The Ideal MHD Limit. *ApJ*, 681:1356–1376.

Mellon, R. R. and Li, Z. (2009). Magnetic Braking and Protostellar Disk Formation: Ambipolar Diffusion. *ApJ*, 698:922–927.

Men'shchikov, A., André, P., Didelon, P., Könyves, V., Schneider, N., Motte, F., Bontemps, S., Arzoumanian, D., Attard, M., Abergel, A., Baluteau, J., Bernard, J., Cambrésy, L., Cox, P., di Francesco, J., di Giorgio, A. M., Griffin, M., Hargrave, P., Huang, M., Kirk, J., Li, J. Z., Martin, P., Minier, V., Miville-Deschênes, M., Molinari, S., Olofsson, G., Pezzuto, S., Roussel, H., Russeil, D., Saraceno, P., Sauvage, M., Sibthorpe, B., Spinoglio, L., Testi, L., Ward-Thompson, D., White, G., Wilson, C. D., Woodcraft, A., and Zavagno, A. (2010). Filamentary structures and compact objects in the Aquila and Polaris clouds observed by Herschel. *A&A*, 518:L103+.

Mestel, L. (1965). Problems of Star Formation I, II. *QJRAS*, 6:161–+.

Mestel, L. and Spitzer, Jr., L. (1956). Star formation in magnetic dust clouds. *MNRAS*, 116:503–+.

Morton, S. A. (1991). *The role of ambipolar diffusion in the formation of interstellar cloud cores and protostars*. PhD thesis, AA(Illinois Univ. at Urbana-Champaign, Savoy.).

Morton, S. A., Mouschovias, T. C., and Ciolek, G. E. (1994). Ambipolar diffusion, interstellar dust, and the formation of cloud cores and protostars. 2: Numerical method of solution. *ApJ*, 421:561–569.

Mott, N. F. and Massey, H. S. W. (1987). *The theory of atomic collisions (3rd ed.)*.

Motte, F., Andre, P., and Neri, R. (1998). The initial conditions of star formation in the rho Ophiuchi main cloud: wide-field millimeter continuum mapping. *A&A*, 336:150–172.

Mouschovias, T. C. (1975). *Static equilibria of the interstellar gas in the presence of magnetic and gravitational fields*. PhD thesis, California Univ., Berkeley.

Mouschovias, T. C. (1979). Ambipolar diffusion in interstellar clouds - A new solution. *ApJ*, 228:475–481.

Mouschovias, T. C. (1987). Star formation in magnetic interstellar clouds. I - Interplay between theory and observations. II - Basic theory. In G. E. Morfill & M. Scholer, editor, *NATO ASIC Proc. 210: Physical Processes in Interstellar Clouds*, pages 453–489.

Mouschovias, T. C. (1996). Multifluid magnetohydrodynamics and star formation. In K. C. Tsinganos, editor, *Solar and Astrophysical Magnetohydrodynamic Flows*, pages 505–538.

Mouschovias, T. C. and Psaltis, D. (1995). Hydromagnetic waves and the linewidth-size relation in interstellar molecular clouds. *ApJL*, 444:L105–L108.

Mouschovias, T. C. and Spitzer, Jr., L. (1976). Note on the collapse of magnetic interstellar clouds. *ApJ*, 210:326–+.

Mouschovias, T. C., Tassis, K., and Kunz, M. W. (2006). Observational Constraints on the Ages of Molecular Clouds and the Star Formation Timescale: Ambipolar-Diffusion-controlled or Turbulence-induced Star Formation? *ApJ*, 646:1043–1049.

Myers, P. C. (1985). Molecular cloud cores. In Black, D. C. and Matthews, M. S., editors, *Protostars and Planets II*, pages 81–103.

Myers, P. C. and Fuller, G. A. (1992). Density structure and star formation in dense cores with thermal and nonthermal motions. *ApJ*, 396:631–642.

Myers, P. C., Fuller, G. A., Goodman, A. A., and Benson, P. J. (1991). Dense cores in dark clouds. VI - Shapes. *ApJ*, 376:561–572.

Nakamura, F. and Li, Z. (2008). Magnetically Regulated Star Formation in Three Dimensions: The Case of the Taurus Molecular Cloud Complex. *ApJ*, 687:354–375.

Nakano, T. and Tademaru, E. (1972). Decoupling of Magnetic Fields in Dense Clouds with Angular Momentum. *ApJ*, 173:87–+.

Nutter, D. and Ward-Thompson, D. (2007). A SCUBA survey of Orion - the low-mass end of the core mass function. *MNRAS*, 374:1413–1420.

Offner, S. S. R., Klein, R. I., and McKee, C. F. (2008a). Driven and Decaying Turbulence Simulations of Low-Mass Star Formation: From Clumps to Cores to Protostars. *ApJ*, 686:1174–1194.

Offner, S. S. R., Krumholz, M. R., Klein, R. I., and McKee, C. F. (2008b). The Kinematics of Molecular Cloud Cores in the Presence of Driven and Decaying Turbulence: Comparisons with Observations. *AJ*, 136:404–420.

Ossenkopf, V. and Mac Low, M. (2002). Turbulent velocity structure in molecular clouds. *A&A*, 390:307–326.

Padoan, P., Juvela, M., Goodman, A. A., and Nordlund, Å. (2001). The Turbulent Shock Origin of Proto-Stellar Cores. *ApJ*, 553:227–234.

Pineda, J. E., Rosolowsky, E. W., and Goodman, A. A. (2009). The Perils of Clumpfind: The Mass Spectrum of Substructures in Molecular Clouds. *ApJL*, 699:L134–L138.

Ryden, B. S. (1996). The Shapes of Dense Cores and BOK Globules. *ApJ*, 471:822–+.

Shu, F. H., Allen, A., Shang, H., Ostriker, E. C., and Li, Z. (1999). Low-Mass Star Formation: Theory. In C. J. Lada & N. D. Kylafis, editor, *NATO ASIC Proc. 540: The Origin of Stars and Planetary Systems*, pages 193–+.

Stone, J. M. and Norman, M. L. (1992). ZEUS-2D: A Radiation Magnetohydrodynamics Code for Astrophysical Flows in Two Space Dimensions. II. The Magnetohydrodynamic Algorithms and Tests. *ApJS*, 80:791–+.

Stone, J. M., Ostriker, E. C., and Gammie, C. F. (1998). Dissipation in Compressible Magnetohydrodynamic Turbulence. *ApJL*, 508:L99–L102.

Tassis, K. (2007). The shapes of molecular cloud cores in Orion. *MNRAS*, 379:L50–L54.

Tassis, K., Christie, D. A., Urban, A., Pineda, J. L., Mouschovias, T. C., Yorke, H. W., and Martel, H. (2010). Do lognormal column-density distributions in molecular clouds imply supersonic turbulence? *MNRAS*, 408:1089–1094.

Tassis, K., Dowell, C. D., Hildebrand, R. H., Kirby, L., and Vaillancourt, J. E. (2009). Statistical Assessment of Shapes and Magnetic Field Orientations in Molecular Clouds through Polarization Observations. *MNRAS*, 399:1681–1693.

Tassis, K. and Mouschovias, T. C. (2004). Ambipolar-Diffusion Timescale, Star Formation Timescale, and the Ages of Molecular Clouds: Is There a Discrepancy? *ApJ*, 616:283–287.

Tassis, K. and Mouschovias, T. C. (2007). Protostar Formation in Magnetic Molecular Clouds beyond Ion Detachment. II. Typical Axisymmetric Solution. *ApJ*, 660:388–401.

Testi, L. and Sargent, A. I. (1998). Star Formation in Clusters: A Survey of Compact Millimeter-Wave Sources in the Serpens Core. *ApJL*, 508:L91–L94.

Williams, J. P., de Geus, E. J., and Blitz, L. (1994). Determining structure in molecular clouds. *ApJ*, 428:693–712.

Wong, T., Ladd, E. F., Brisbin, D., Burton, M. G., Bains, I., Cunningham, M. R., Lo, N., Jones, P. A., Thomas, K. L., Longmore, S. N., Vigan, A., Mookerjea, B., Kramer, C., Fukui, Y., and Kawamura, A. (2008). Molecular line mapping of the giant molecular cloud associated with RCW 106 - II. Column density and dynamical state of the clumps. *MNRAS*, 386:1069–1084.

Zuckerman, B. and Evans, II, N. J. (1974). Models of massive molecular clouds. *ApJL*, 192:L149–L152.

Zuckerman, B. and Palmer, P. (1974). Radio radiation from interstellar molecules. *ARAA*, 12:279–313.